# Impacts of Future Storminess, Greater Wave Energy,and Increased Sediment Transport along Castle Neck and into Essex Bay: Essex, MA

*Municipal Vulnerability Preparedness Grant Program*


July 2021

Boston University: *Duncan FitzGerald, Zoe Hughes, Alice Staro*
University of New Orleans: *Md Mohiuddin Sakib*
Town of Essex: *Brendhan Zubricki*

## Executive Summary

Like many coastal communities, the Town of Essex is vulnerable to the effects of global warming and climate change, conditions that are leading to an increase in the rate of sea-level rise (SLR) and a greater frequency and magnitude of coastal storms. This project addressed three priority actions *identified by the Essex Community Resilience Building Workshop and Report*, with an overall goal quantifying vulnerability of natural and Town resources to changing climate, as well as determining how to work with the system to improve the resilience of the coastline around Essex via nature-based solutions. In Ipswich, the project was aimed at improving our understanding of the Castle Neck barrier system and particularly sand transport along Crane Beach and into Essex Bay. This research provided information for recommending future best management practices and soft solutions to maintain the integrity of the barrier, along with learning more about the conditions causing flooding in the Argilla Road area**.**

The Castle Neck barrier and Essex Tidal Inlet and Bay complex are part of a highly dynamic and interconnected sand transport regime that is dominated by a southerly longshore littoral transport system driven by northeast storms. Sand supply is controlled by behavior of the Sandy point spit and platform in Plum Island Sound. The alignment of the main ebb channel dictates how sand bypasses the inlet. Further down Castle Neck, sand is sequestered for periods of 15 to 20 years at the mid-island region starving the Southern Spit of sediment. Between the 2011-2016 period it lost 178,000 $m^3$ of sand.

Sand eroded from the Southern Spit system moves in a net pathway into Essex Bay where it fills channels, such as Castle Neck River, and builds and enlarges sand shoals, including the inner flood-tidal delta west of Conomo Point. This movement of sand into Essex Bay helps to sustain shellfish grounds and eelgrass beds as sea level rises. The landward of sediment up the Essex Estuary also aids the delivery of silt and fine sand to the marsh platform improving their resiliency. Castle Neck can be divided into four distinct regions based on sand transport trends, morphology, and patterns of shoreline change. Cedar Point and Steep Hill Beach are stable but can experience periods of storm erosion followed by beach reconstruction. North Crane Beach has undergone dramatic changes related to shifts in the position of the main Plum Island inlet channel, involving 50 to 400 m of shoreline advancement and recession. Presently, this section of shoreline is stable. The Beach Protuberance is an area that progrades and recedes depending on cycles of inlet sediment bypassing. The Southern Spit has been in a stage of erosion since 1995. From 1938 to 2018 the Castle Neck barrier decreased in area by 438,788 $m^2$ (Table 9, Figure 63) and by 2020 the loss in area increased to 611,958 $m^2$ (Figure 71). This loss of sand was likely multicausal and related to sea-level rise, decreased sand supply coming from Plum Island, and sand losses to the offshore and to the backbarrier. The reduced sand coming from Plum Island may be related to human activities, including jetty repair, dredging activity, and construction of revetments and seawalls along the northern portion of the island**.**

Storm flooding in the system is particularly sensitive to the angle of storm winds and storm approach, due to the position of the system with respect to Cape Anne. Future increases in storminess is associated with higher frequency of flooding in areas already recognized as at risk.

**Table of Tasks/Deliverables**

| **Task #** | **Deliverable** | **Section** |
|---|---|---|
| Task 1 | Maps of historical evolution of system | Section V.D.2 and VII.B |
| Task 2.1 | Elevation and post-storm change surveys | Section V.D.1.and VII.. |
| Task 2.2 | Time series of currents, tides, and waves | Section V.E. and VII.A |
| Task 2.3 | Sediment sampling and analyses | Section V.A. and |
| Task 3. | Storm statistics, selection and inputs | Section VI. A 5 and 6 |
| Task 4 | Specification of marsh elevation to future sea level for model | Section VI. A 1, 5 and 6 |
| Task 5 | Functioning, calibrated hydrodynamic and wave model, plus model output for different storm and SLR scenarios | Section VI.A 1-4 |
| Task 6. | Discussion of different sea level and storm scenarios examining flooding and erosion potential and website | Section VI A5 . Section VII.C, D. Section VIII.<br>Section IX |
| Management | Input from stakeholders and outreach/sharing results. Reporting. | Section IX |

## TABLE OF CONTENTS

## INDEX OF ILLUSTRATONS

## LIST OF TABLES

# I. INTRODUCTION

Like many coastal communities, the Town of Essex is vulnerable to the effects of global warming and climate change, conditions that are leading to an increase in the rate of sea-level rise (SLR) and a greater frequency and magnitude of coastal storms. During winter of 2018 the Massachusetts coastal zone experienced extensive flooding and wave erosion from intense Nor'easters. Numerous roadways in Essex and Ipswich became impassible, including much of the Essex downtown, and storm waves severely damaged the seawall protecting Conomo Point. Large magnitude storms are forecasted to become more prevalent in the future due to climate change. This project addressed three priority actions identified by the Essex Community Resilience Building Workshop and Report, with an overall goal quantifying vulnerability of natural and Town resources to changing climate, as well as determining how to *work with the system* to improve the resilience of the coastline around Essex via nature-based solutions. In Ipswich, the project was aimed at improving our understanding of the Castle Neck barrier system and particularly sand transport along Crane Beach and into Essex Bay. This research provided information for recommending future best management practices and soft solutions to maintain the integrity of the barrier, along with learning more about the conditions causing flooding in the Argilla Road area.

# II. BACKGROUND

During the winter of 2018, the coastal zone along the North Shore and throughout Massachusetts experienced extensive flooding and wave erosion generated by large astronomic tides coupled with the passage of intense extra-tropical storms. The impact was felt throughout the coastal communities surrounding the Great Marsh and Essex Bay. Massachusetts officials compared the impact of the 4 January 2018 Bomb Cyclone to a Category 1 hurricane (e.g., Kurt Schwartz, director of the Massachusetts Emergency Management Agency). Along the oceanside of the bay, a clear imprint of the events was observed in severe beach erosion, dune scarping, and overwash along Castle Neck, Plum Island, and Salisbury Beach. Several large areas within the Great Marsh experienced an unprecedented ice-raft sediment deposition. Inland areas also suffered from extensive flooding including waves crashing over the Plum Island Turnpike, standing water affecting sewer systems, and impacts to Plum Island Shellfish Purification Plant. Numerous roadways in Essex, Ipswich and elsewhere became impassible, including in downtown Essex along Route 133 (Figure 1, Table 1) and Argilla Road at the Entrance to Castle Neck. These conditions present an obvious impediment and danger to rescue and service vehicles during major storms. However, recent research shows that such events will occur with increasing frequency as climate changes (Colle et al, 2013; Zhang and Colle 2018).

Like many coastal communities along the North Shore, the towns of Essex and Ipswich are vulnerable to the effects of global warming and climate change, conditions that are leading to an increase in the rate of sea-level rise (SLR) and a greater frequency and magnitude of coastal

storms (Figure 2). The increasing frequency of flooding in downtown Boston and in other coastal cities is a direct consequence of rising sea level. Predicted SLR and increased storm surge have the potential to significantly and negatively impact Essex residents and the economy, facilities, and infrastructure upon which the community relies.

A Municipal Vulnerability Preparedness Workshop was held for the Town of Essex on 5th April 2018 at the Essex Town hall. The Town of Ipswich completed this process in March of 2019 and has developed a draft report. Our primary rationale is to address certain concerns that both Essex and Ipswich's ranked in their top MVP action items. In Essex, three major types of features and resources most vulnerable to tidal flooding, storm surge flooding, and sea-level rise, were listed: 1. Town infrastructure, 2. Elderly and defenseless people living in flood zones, and 3. Environmental natural resources. Critical infrastructure includes the MassDOT Bridge and the Causeway that runs through the middle of the Town's commercial area, comprising its restaurants, antique shops, marinas, and other businesses. The seawall fronting Conomo Point, which was partly damaged during the 2018 winter storms, is another important structure that protects residential and Town property. One of the major issues that the Town faces, is that Essex Bay and the Essex River estuary extend deeply into the Town's interior, translating to a large portion (> 40%) of it being within the 100-yr flood zone (Figure 2; MassDEP, 2018). As sea level rises, potential flooding impacts an increasingly greater area of the town. For example, as the southeast end of the Castle Neck barrier retreats (Figure 3), storm surge water can flow more easily into Essex Bay raising water levels and exacerbating inland flooding. At the same time, high energy storm waves are more able to propagate into the bay, accelerating marsh edge erosion (Figure 4) and impacting Conomo Point. Another consequence of SLR and greater storminess is

Table 1. **Sites within Essex that will be impacted by major storms (from Schottland et al 2017).**

| **Identified Area of Flooding** | **Cause of Flooding** |
|---|---|
| 1. Main Street (Rt 133)- Woodman's Landing | Tidal inundation, Storm-surge flooding |
| 2. Island Road | Tidal inundation, Storm-surge flooding |
| 3. Conomo Point Road/Robbins Island Road | Tidal inundation, Storm-surge flooding |
| 4. J.T. Farnham's Restaurant Culvert/Eastern Ave. @ Ebben Creek | Tidal inundation, projected storm-related flooding, scouring/erosion |
| 5. Apple Street Bridge | Storm-related flooding |
| 6. Lake Chebacco | Storm-related flooding |
| 7. Gregory Island Road | Storm-related flooding |
| 8. Walnut Park | Storm-related flooding |
| 9. Quinn Brothers | Storm-related flooding |
| 10. Landing Road Culvert | Storm-related flooding |
| 11. Apple Street near Andrews Street | Storm-related flooding |
| 12. Route 22 Culvert near Country Road | Storm-related flooding |


**Figure 1.** View of Main Street: A. during a spring high tide and B. during the Bomb Cyclone
View of Main Street: A. during a spring high tide and B. during the Bomb Cyclone of 4 January 2018 (photo curtesy of Peter Phippen). This type of flooding will increase in frequency in the forecasted regime of sea level rise and increase storminess.

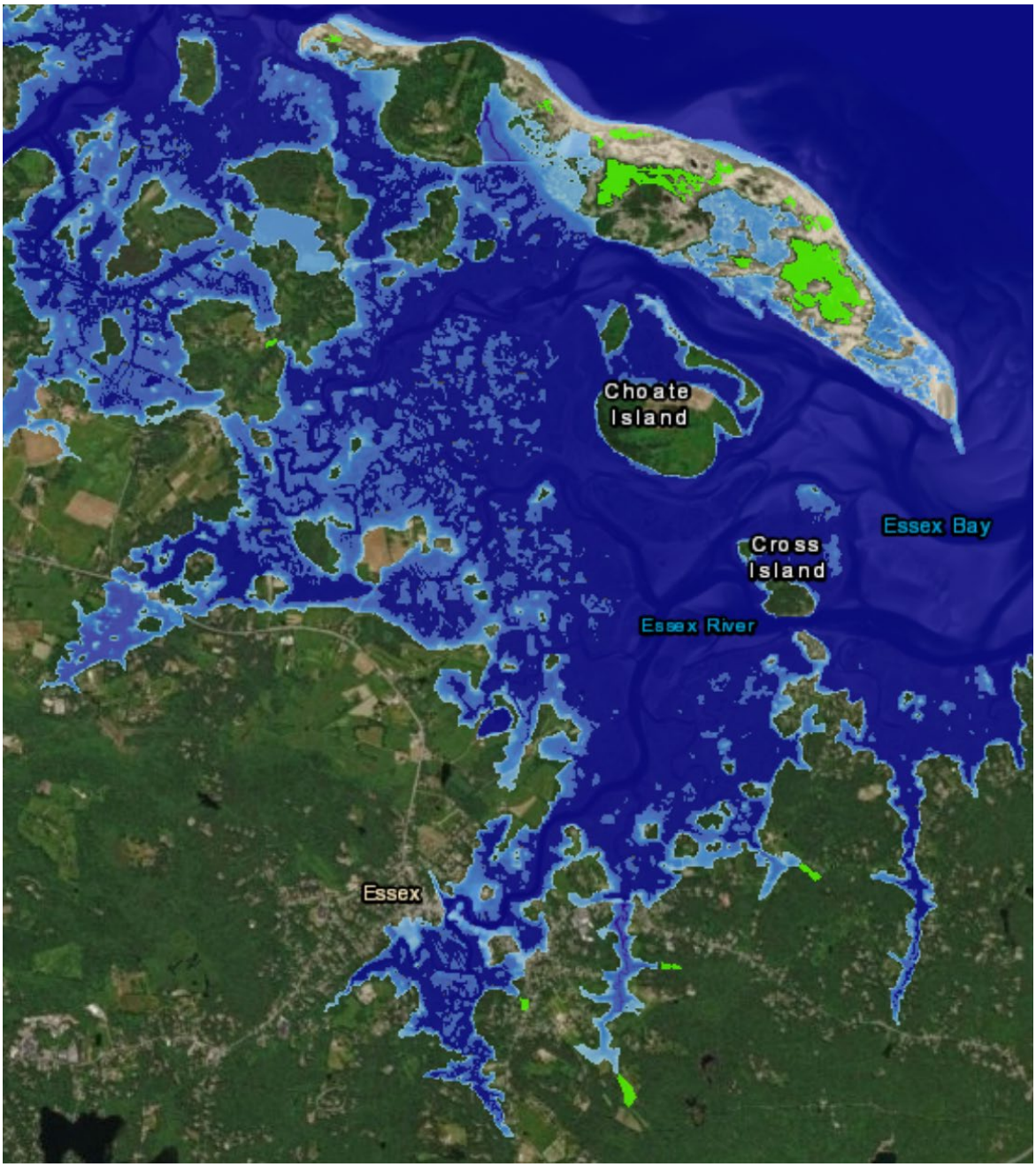


**Figure 2**. Map showing areas within the 100-yr flood for the Essex region (NOAA, 2019) using the projected relative sea levels in 2050 for three climate scenarios for Boston, MA based on RCPs 2.6, 4.5, and 8.5, which are within 2 inches of one another (from Kopp et al., 2014). Note extensive flooding of Castle Neck and reaching far interiors of Essex.

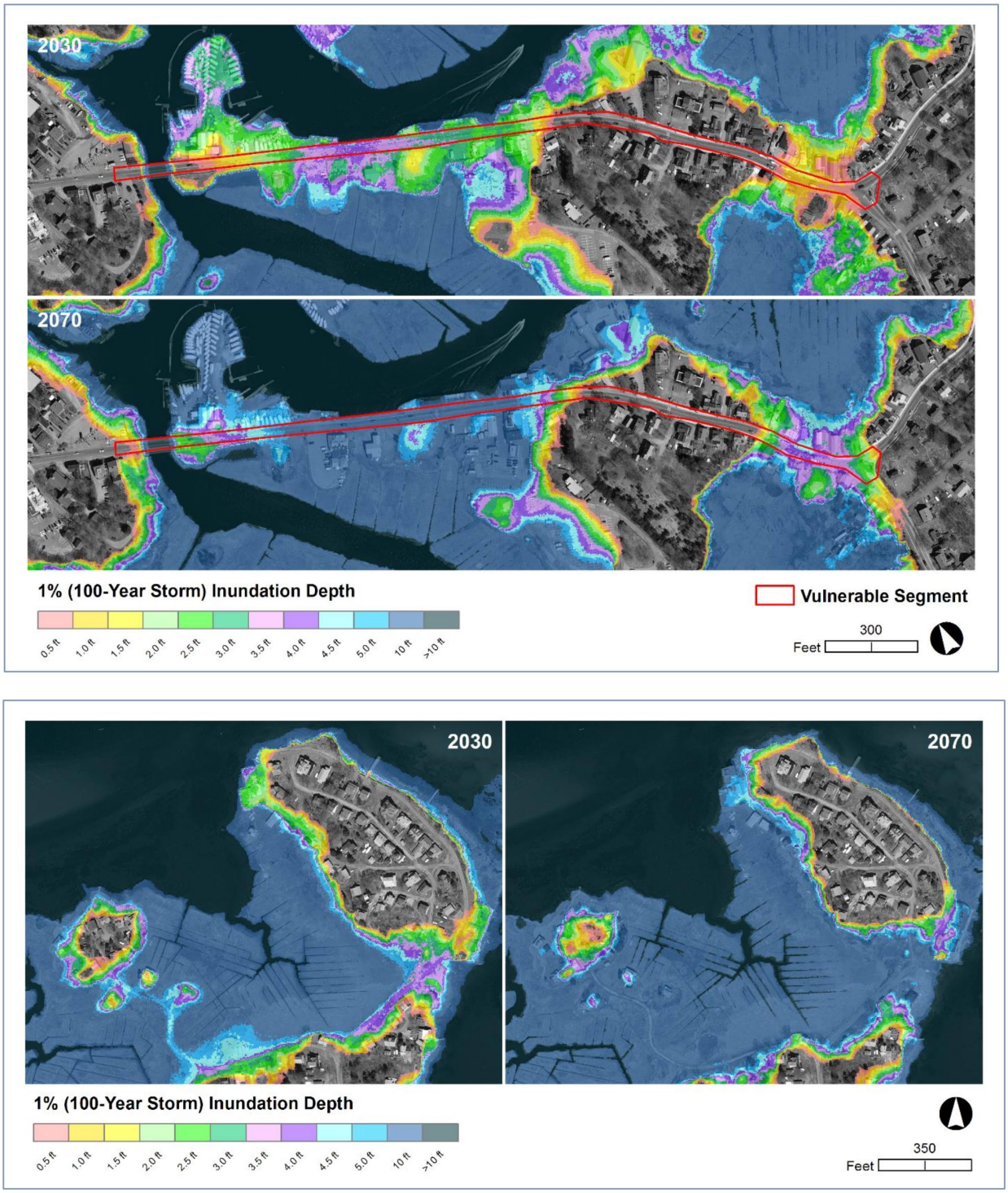


**Figure 3. Top panel:** One-hundred year storm inundation depthfor Essex Causeway and Woodman's Landing, projected for 2030 and 2070. **Bottom panel**: One-hundred year storm inundation depth for Conomo Point region.

the increased rate of sand transport along barriers, including Crane Beach. That process will cause a redistribution of sediment within sand reservoirs (barriers, nearshore deposits, tidal deltas, and sand bodies inside the bays) leading to possible erosion ocean side, and increased rates of sand entering Essex Bay. For example, during the past 25 years as the southern end of Castle Neck been retreating (~ 0.5 km). Much of the eroded sand has moved into Essex Bay. It is important to know the rate at which sand is entering Essex Bay and where it is being deposited (both with respect to Ipswich's loss of sand from the barrier island and the effects of changing sedimentation patterns within Essex) This sand impacts shellfish beds, sedimentation in channels, and possible marsh formation. The continued health of Castle Neck, which is major MVP priority for the Town of Ipswich is also affected.

## III. PHYSICAL SETTING

The Merrimack Embayment in northern Massachusetts is a formerly glaciated terrain now fronted by a 34-km long, mixed-energy barrier island system (sensu, Hayes 1979). One of the central barriers along this coast is Castle Neck bordered to the north by Plum Island Sound Inlet and Essex River Inlet to south. North of Plum Island is Merrimack River Inlet, the second largest freshwater discharge into the Gulf of Maine. Tidal inlets along the chain are associated with diminutive estuaries having small drainage basins (FitzGerald 1993). Inlets are anchored next to bedrock outcrops or occur between resistant drumlin landforms (FitzGerald and van Heteren 1999). Stabilization of the landward migrating proto-Plum Island-Castle Neck barrier system occurred circa 3.6 ka (Hein et al 2012) leading to the development of Plum Island Sound, Essex Bay, and the contiguous Great Marsh. The Great Marsh is an internationally-recognized Important Bird Area, and a region that supports dozens of federal trust species, as well as state and federally designated Critical Natural Landscapes.

The backbarrier of Castle Neck is dominated by a shallow lagoonal estuary floored by ubiquitous intertidal and subtidal sand bodies (Figure 4). Mean depth along the thalweg gradually deepens from < 2 m proximal to the upper Essex River near the bridge to > 10 m at the inlet throat (Figure 4). The backbarrier of Essex comprises approximately 24 $km^2$ and is bounded by bedrock and glacial uplands. Generally, the high tide open water area increases substantively toward Essex Inlet. This region experiences semi-diurnal tides with a mean range of 2.8 m, increasing to more than 3.7 m during perigean spring tidal conditions (NOAA 2021). The backbarrier spring tidal prism ($30 \times 10^6$ $m^3$; Smith and FitzGerald 1994) is exchanged through Essex River Inlet. inlet at the southern Castle Neck barrier.

Essex contains broad platform marshes dissected by numerous creeks and several major channels including the Essex River and Castle Neck Rivers and several smaller creeks such as Alewife Brook, Ebben Creek, Soginese Creek, and Walker Creek. (Figure 5). The high marsh is dominated by *Spartina patens* and *Distichlis spicata*, and the less extensive low marsh is vegetated by short-form *Spartina alterniflora*. Long- and short- form *Spartina alterniflora* are

typically found along creek banks and in poorly drained areas, respectively (Wilson et al 2014). Low marsh areas have an average elevation of 0.98 m above mean sea level; high marshes are ~40 cm higher and flood only during spring tides (Valentine and Hopkinson 2005; Millette et al 2010). Tidal channels and anthropogenic ditches dissect the entire marsh and numerous large and small salt pannes and ponds spot the high marsh surface.

The Great Marsh and Essex Bay are fed by several small streams and brooks draining coastal lowlands dominated glacial and paraglacial deposits (Stone et al., 2006). Both Essex River and Castle Neck River are almost entirely tidal and have negligible freshwater inputs except during periods of intense precipitation. The largest contribution of freshwater and suspended sediment to the coastal ocean is the Merrimack River, which has a watershed area of 12,885 km$^2$, an.

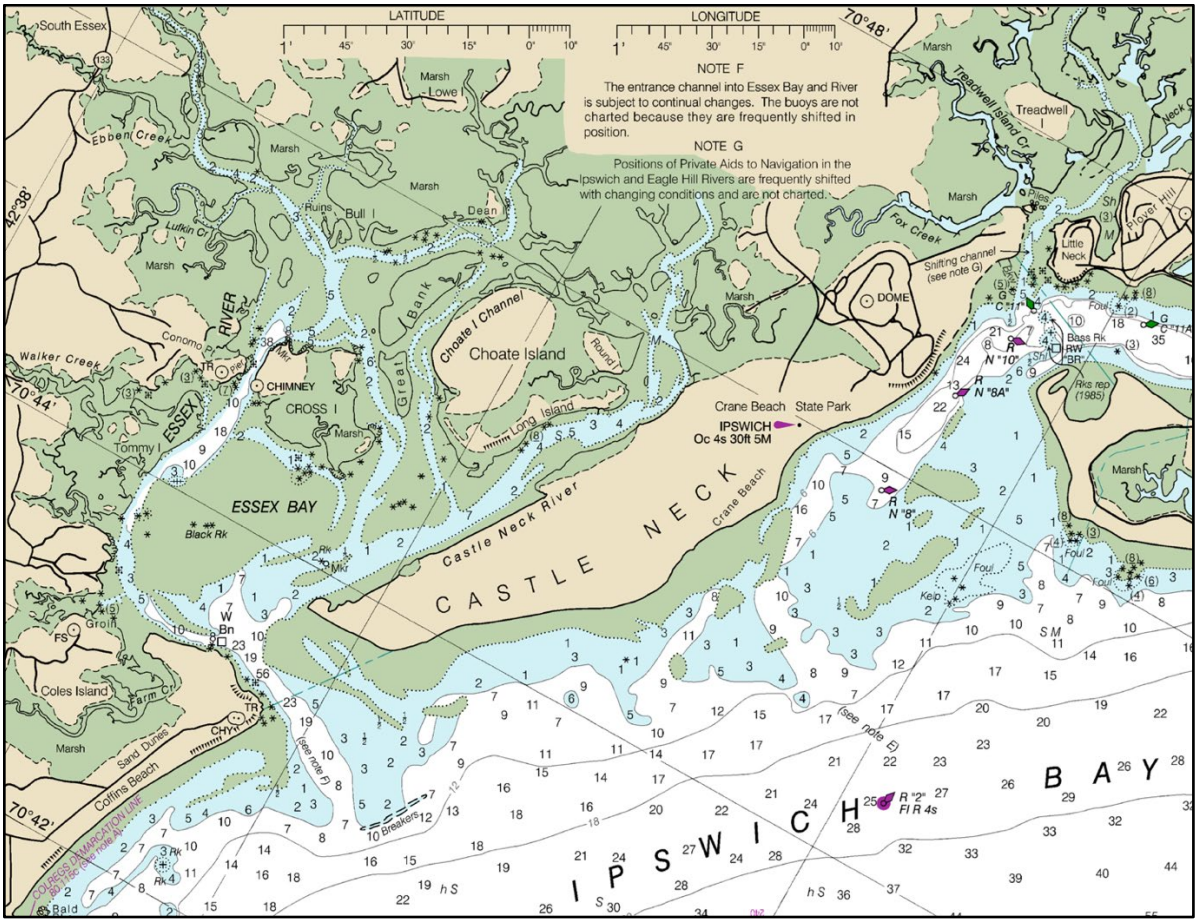


**Figure 4.** NOAA coastal chart (13274)of the northern of Essex Bay and Great Marsh region. Many of the islands within the marsh are composed of one or several amalgamated drumlins.

average discharge of 6.5 km$^3$/yr, and total suspended sediment load of 74,880 MT/yr (Shawler et al 2019). Circulation models demonstrate that a limited amount of suspended sediment from the

Merrimack River can travel south and enter Plum Island Sound and further south to Essex Bay (Zhao et al 2010). The discharge of freshwater into the Essex River is minimal except during intense precipitation events, and thus, the large tidal range and relatively shallow nature of the channel produces a well-mixed estuary

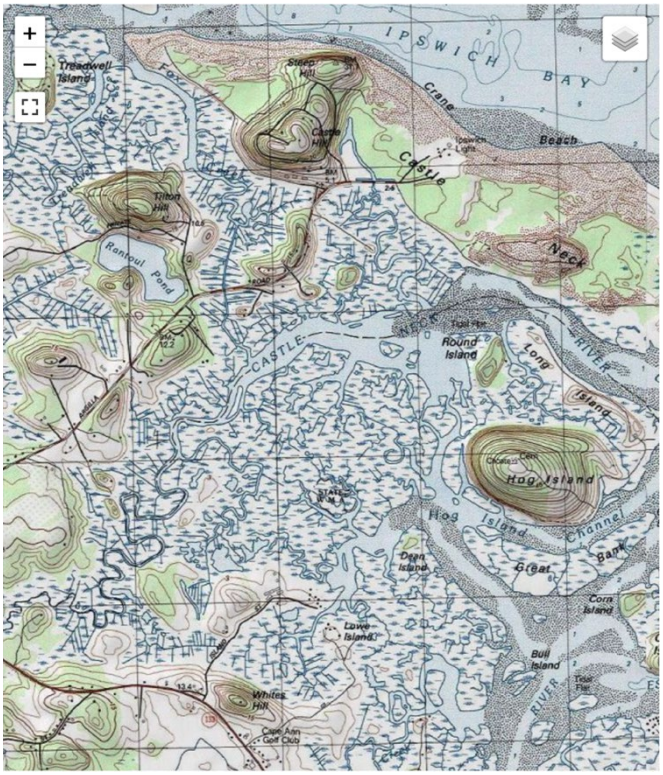


**Figure 5a.** USGS Topographic mapof Castle Neck and backbarrier region. Note the drumlins that appear as oval-shaped hills (e.g., Castle Hill, Tilton Hill, and Hog Island). These topographic highs were the anchoring sites for sediment accumulation when the barrier was first developing and the backbarrier was filling in.


**Figure 5b.** Southeast portion of Castle Neck and Essex Inlet. Note the number of drumlins that form the upland landscape and islands within the marsh system. The backbarrier has two prominent tidal river including Castle Neck running behind the barrier and Essex River that runs into downtown.


**Figure 5c.** Argilla Road forms the boundary between the Essex and Ipswich backbarrier systems. The road crosses low-lying marsh and is subject to storm flooding. A small culvert at this site connects the Essex and Ipswich tidal systems.

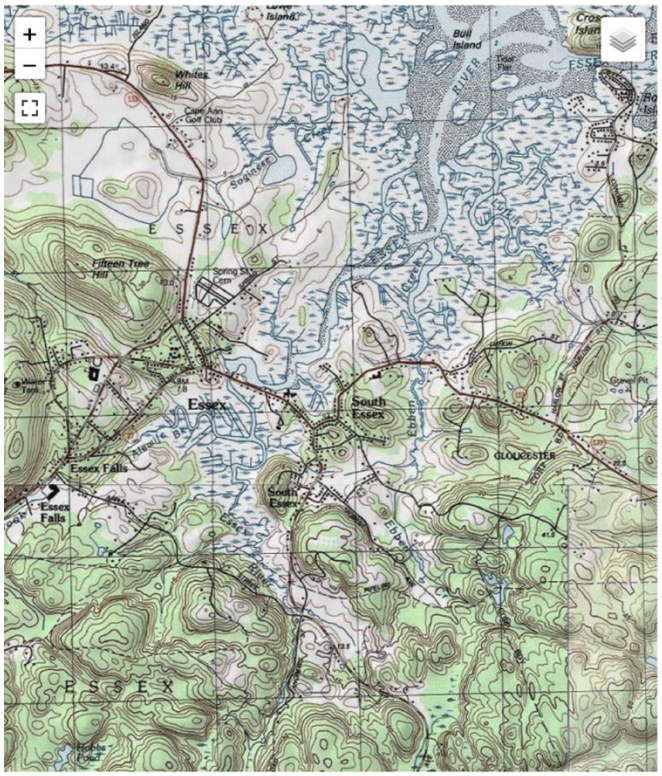


**Figure 5d.** The interior portion of the Essex River drainage system shows the uplands confined the development of marsh. The discharge of freshwater into the Essex River is minimal except during intense precipitation events. Thus, the large tidal range and relatively shallow nature of the channel produces a well-mixed estuary.

Essex River Inlet is a well study inlet that was the basis for the Hayes (1975, 1979) mixed energy tidal inlet model that contains a well-developed arcuate ebb-tidal delta fronting the inlet and a

classic horseshoe-shaped flood within Essex Bay (Figure 6). Tidal current measures, bedform distributions, and historical morphological changes of Essex Inlet and ebb-tidal delta system can be found in Smith and FitzGerald (1994). This section of coast has built from sand reworked onshore during the Holocene transgression (FitzGerald and Heteren 1999; Hein et al 2012) and sand discharged directly from the Merrimack River (FitzGerald et al 2005). The dominant longshore transport direction is south as evidenced by: 1) a decrease in grain size, 2) seaward excursion of the 5-m isobath, 3) increase of Holocene sediment toward Cape Ann as well as 4) offshore wave data (FitzGerald et al 2006; Hein et al 2013). An example of wave times series in 2011 from a NOAA wave buoy offshore of Merrimack Inlet is given in Figure 7. Note that the largest waves that have the greatest influence on the rate and direction of longshore sand transport come from the northeast and are related to the passage of extratropical Northeast storms, such as the Bomb Cyclone of 4 January 2018 and Blizzard of 13 March 2018.

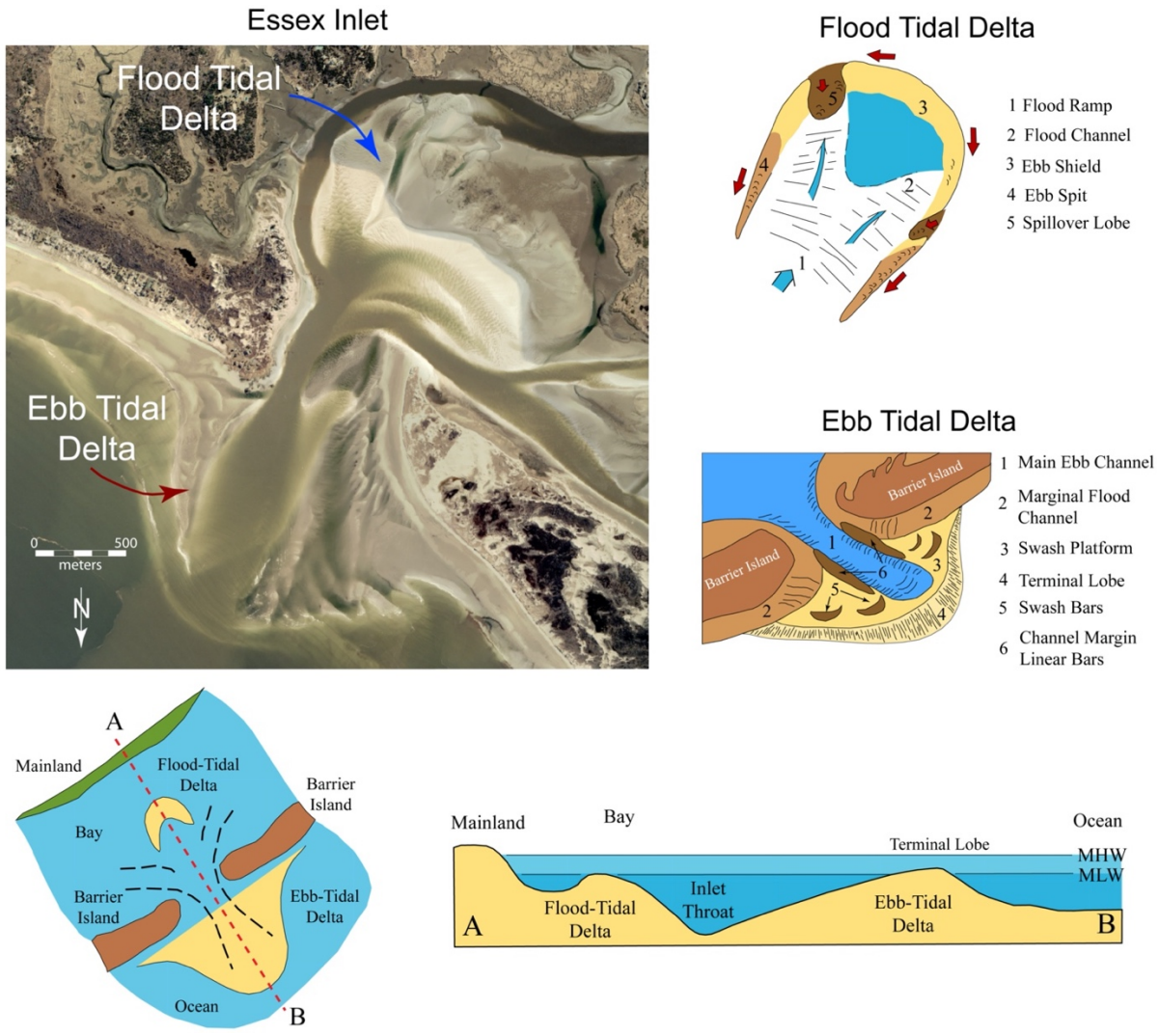


**Figure 6**. Ebb- and flood-tidal models (from Hayes, 1979). Aerial photograph of Essex Inlet, MA. Inlet cross section model from FitzGerald (1996).

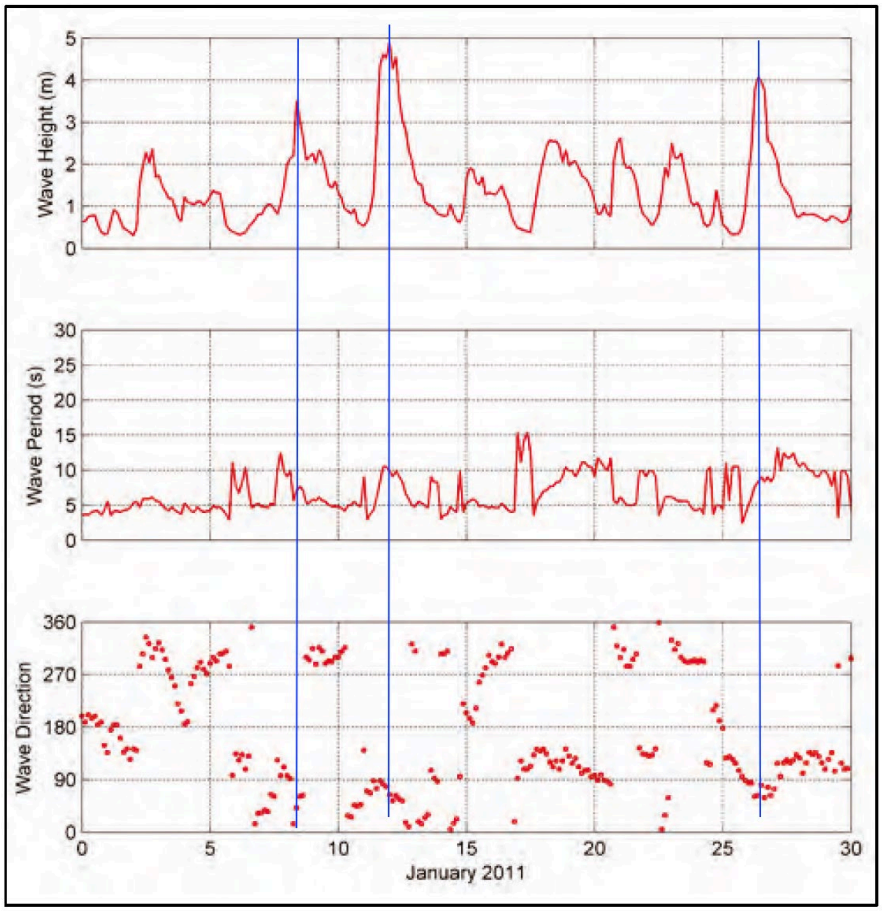


**Figure 7.** Wave data collected at NDBC buoy 44098located 50 km east of Merrimack River Inlet (from Li et al 2018). Note that largest waves were recorded from the northeasterly quadrant.

## IV. OUTLINE OF MAJOR STUDIES

This was a multifaceted project with several seemingly disparate goals, but ultimately interrelated because of their focus on the effects of climate change and associated sea level rise and increased storminess.

### A. Castle Neck Barrier

The Castle Neck barrier is one of the major barriers along the Merrimack Embayment island chain. It is mostly an unfettered barrier consisting of an extensive beach, frontal dune and secondary dune system, fringing marsh, and a spit complex at the southeast end. In order to understand the overall extent of the island's sand reservoirs and how their distribution has changed with time, an historical analysis was made in terms long-term areal changes and volumetric changes using the 2007 and 2017 Lidar data sets. This information is used to project the future evolution of the barrier translate those findings into management guidelines.

## B. Crane Beach

Crane Beach is the most dynamic section of Castle Neck and with a visitor population of more than 350,000 each year, it is the most utilized part of the barriers and under the greatest human pressure. In order to understand the processes affecting the beach, we undertook field campaigns, laboratory analyses, and GIS studies to document historical shoreline changes and the erosional-depositional processes that produce these trends. Field campaigns consisted of collection of sediment samples and surveying the topography of the beach using RTK transects. Sediment transport trends were established from laboratory grain size and mineralogical determinations. Analysis of historical aerial photographs and GIS routines allowed a documentation of how sand is transferred through the system from southern Plum Island to Essex Bay. Various controlling processes include, 1) spit cycling at Sandy Point at the southern end of Plum Island, 2) meandering of the channel adjacent to the beach, 3) ebb channel deflection and breaching, 4) growth and decay of a mid-island beach protuberance, 5) erosion of the southeast spit, and 6) sand washed into Essex Bay.

## C. Spit, Essex Inlet, and Essex Bay

These three morphological units are connected by sediment transport regimes. Sand eroded from the spit is fed into the inlet and from there transport seaward by ebb current to the ebb-tidal delta or moved landward by flood currents into the bay. In order to track this sand distribution system, we have conducted a detailed grain size analysis, historical image analysis, and hydrodynamic modeling. Together these studies reveal the sand circulation patterns and the morphological changes they produce. For example, we show that sand from the ebb-delta is transported back onshore rebuilding the spit, while other sand is transported into the bay causing channel shifting and the enlargement of sand shoals, which has important consequences to shell-fishing and eel grass beds.

## D. Wave Energy inside Essex Bay

One of the recurring issues for the Town of Essex has been wave damage to Conomo Point region, particularly the seawall protecting the northern end of the coastal village. Storm dismantlement of the wall and erosion have been a hardship to the town both in terms of rebuilding costs as well as the expenditure of time and effort of town officials in seeking outside funding. Our coupled hydrodynamic and wave modeling scheme (Delft3D-Swan) has allowed us to identify shoreline hotspots where storm wave energy is concentrated and how this condition will be exacerbated in the future due to increased sea-level rise and greater storminess.

## E. Storm Surge Flooding

A major impact of Northeast storms to the Town of Essex, Town of Ipswich, and other coastal communities is lowland flooding caused by storm surges usually coinciding with astronomic

high tides. For example, downtown Essex was flooded by two major storms in 2018 as was Argilla Road near the Crane Estate. Tidal waters washed unabatedly across Main Street in Essex during the Bomb Cyclone of 4 January 2018 (Figure 1b) and similar state occurred later that winter in mid-March. The vulnerability of this region is demonstrated by the photo taken of Essex during a perigean spring tide in Figure 1a. Note that during a sunny non-storm day that the marsh was completely submerged and many parking lots were partially inundated by a high tide. Our modeling studies show that this condition will occur with increasing occurrence due to rising sea level and greater storm frequency and magnitude. Our modeling yields flooding maps showing the results of different sea level rise and storm magnitude scenarios.

### F. Discussion of Finding in terms of Essex Preparedness

This part of the study focused on using the collective results to apprise the Town of Essex about future areas of concern due to flooding, storm wave impacts, Essex Bay morphological changes affecting shellfish beds and navigation. Likewise, for the Castle Neck region, we use our historical morphological analyses and sand transport trend to identify future areas of potential concern.

## V. METHODOLOGY

### A. Grainsize Data Collection and Analysis

#### *1. Sampling Scheme and Locations*

Sample collection at study area began in 2017 and during the following three years more than 400 samples were collected during field campaigns to: 1. Crane Beach, 2. Spit platform, 3. Essex Inlet, 4. Essex Bay, and 5. Essex River Estuary. These samples were taken by various Boston University professors, graduate students, and several interns at FitzGerald lab and many of the students were involved in the analysis of the samples. Figures 8 and 9 provide the sampling environments and locations of the samples taken throughout the study area and are sorted according to the date when there were collected. These maps are created in Google Earth Pro, and each sample location has been accurately marked with a hand GPS.

#### *2. Sample Processing*

Dry sand samples from the supratidal beach and dunes were analyzed directly at the FitzGerald Sedimentology Lab at Boston University. Samples obtained from underwater environments that were stored in refrigerator were washed with fresh water to remove salt and to break up clusters of sediments that could affect the subsequent granulometric analyses. All samples (after washing for submerged ones, same day of collection for subaerial) were placed in a drying oven, a procedure lasting one to several days at a temperature of 60 C (140 F).


**Figure 8**. Sampling environments at the study area.


**Figure 9.** Location of sand samples taken in the study area. Different colors indicate different dates when the samples were collected.

**Figure 10.** View of Ponar Grab sampler being armed

**Figure 11.** View of Ponar Grab sampler after being liftedto the surface. Note that the apparatus is now closed.

**Figure 12**. Grab is being to retrieve sand sampled.

**Figure 13**. View of sampleplaced labeled plastic bag.

A granulometric analysis of the sediment was performed using a mechanical sieving method (RO-TAP sieve shaker) that consists of a nested sieved that collected increasingly smaller gain sizes toward the bottom of the stack. The Ro-tap was run for approximately 10 minutes using a mesh size ranging from $\varphi$[1]= 0.0 to $\varphi$ = 4.0 (corresponding from coarse sand to coarse silt). The sediment fraction captured in each sieve and the catcher pan at the bottom of the stack was transferred to individual beakers and weight with on a digital scale. Lastly, the samples were placed into their original bag and stored as permanent record (see Figures 14 and 15).

Granulometric analysis allows statistical characterization of the sand samples, which can be used to determine the origin and sediment transport trends. We have applied the Folk and Ward (1957) classification method to determine the following sedimentological and statistical characterization of the sample population[2]:

- **Mean**: the average grain-size. It is calculated as follows:

$$Mean\ \varphi = (\varphi 16 + \varphi 17 + \varphi 84)/3$$

- where 16, 50, and 84 represent the size at 16, 50, and 84 percent of the sample by weight. Mean is measured in phi units and is the most widely compared parameter.
- **Median** (D50): corresponds to the 50 percentile on a cumulative curve. It shows that half of the sample population is larger and half is smaller than the d50.
- **Sorting**: is a method of measuring the grain-size variation of a sample by encompassing the largest parts of the size distribution as measured from a cumulative curve. Folk (1968) presented a verbal classification scale for sorting: very well sorted, moderately well sorted, moderately sorted, poorly sorted, very poorly sorted
- **Skewness:** it measures the degree to which a cumulative curve approaches symmetry. Two samples may have the same average grain size and sorting, but may be quite different in their degree of symmetry. Symmetrical curves have a skewness equal to 0.00; those with a large proportion of fine material are positively skewed and those with a relatively large proportion of coarse material are negatively skewed.
- **Kurtosis**: is a measure of "peakedness" of a curve. Kurtosis of 1.00 is a curve with the sorting in the tails equal to the sorting in the central portion (mesokurtic). If a sample curve is better sorted in the central part than in the tails, the curve is said to be excessively peaked, or leptokurtic. If the sample curve is better sorted in the tails than in the central portion, the curve is flat peaked or platykurtic

The statistical analyses have been calculated using a combination of MATLAB and Excel.

---

[1] Where $\varphi$ is $-\log_2(d)$, d=grain diameter in mm.

[2] Modified from Professor C. Rigsby, East Carolina University


**Figure 14.** Photo of the oven used to dry the samplesin the red cups.


**Figure 15.** View of Ro-tap with nested brass sieves.

STATISTIC PLACEHOLDER

## B. Mineralogical Analysis

Of the more than 400 sand samples taken from the study area, a subset of 135 samples were selected for a microscope description, which produced a mineralogic characterization of the sand Figure 16). This procedure consisted of putting a small amount of sample on a glass slide and placing the slide under a zoom binocular optical microscope with transmitted light. We the made a grain count of the most common mineral/grains found on clastic beaches, including quartz, feldspar, heavy minerals, mica (as minerals) and other grains such as shells and rock

fragments. In addition, we described the roundness[3] (i.e. a visual characterization of the presence/absence of edges on each grain) and checked the sand for magnetic grains (ilmenite and magnetite).

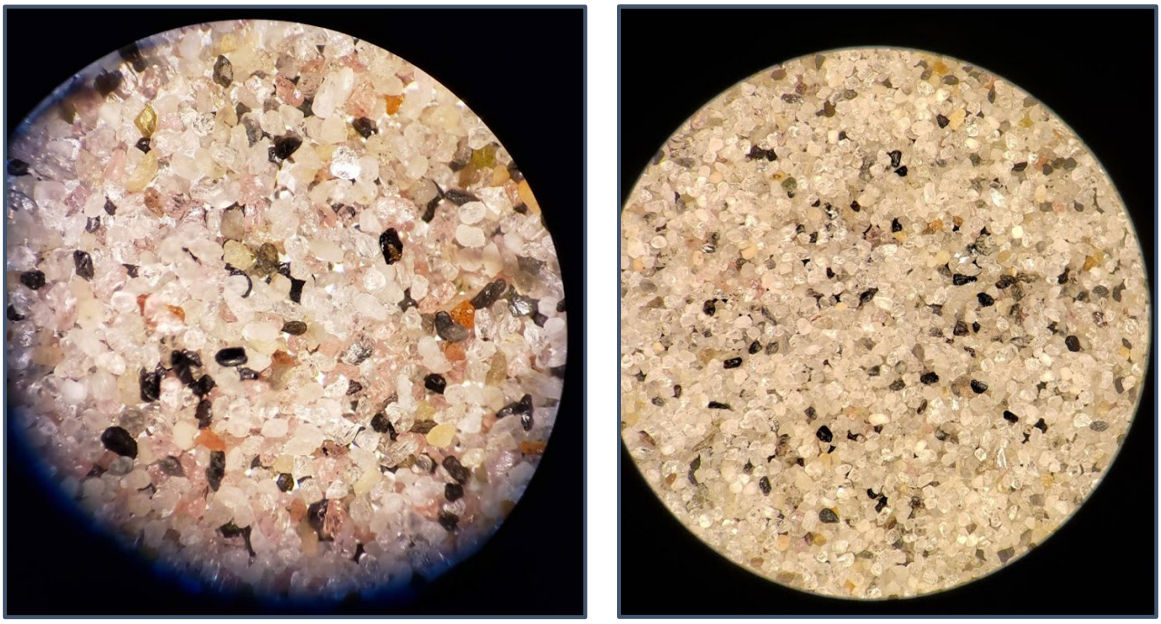

**Figure 16**. Examples of sand grains under the microscope. Quartz are the translucent grains, the pink grains are garnets, and reddish-brown grains are feldspars. The black grains are ilmenite and magnetite and some pyroxenes.

## C. Remote Sensing Methodology (Satellite Imagery)

### *1. Background*

In 2018 several strong northeast storms affected the northeast Atlantic East Coast. These storms were noteworthy in their strength and damage they caused in erosion to beaches and barriers and shoreline buildings, homes, and infrastructure. Their impact was partly a consequence of their occurrence during perigean spring tides (January 4$^{th}$ 2018 Bomb Cyclone also occurred 14 days after perihelion conditions as well). Remote sensing[4] techniques were used to quantify the r of reorganization of sand reservoirs comprising Crane Beach and within the Essex River Inlet and Essex Bay system due to the sequence of storms of extending from November 2017 through late

---

[3] Roundness gives relative information on how much a single grain has been transported. An angular grain likely had had transported less than a grain with round shape, which surface has been smooth.

[4] "Remote sensing is the process of detecting and monitoring the physical characteristics of an area by measuring its reflected and emitted radiation at a distance (typically from satellite or aircraft). Special cameras collect remotely sensed images, which help researchers "sense" things about the Earth" [From USGS https://www.usgs.gov/faqs/what-remote-sensing-and-what-it-used?qt-news_science_products=0#qt-news_science_products]

spring 2018. We have performed a change detection analysis based on a decision tree algorithm for high resolution image classification (Figure 17).

### *2. Imagery*

We collected two images from PlanetScope satellites through the provider Planet (see Figures 18 and 19 and Table 2 for specifications). These images have high resolution (3.5 m) and a high frequency revisiting time (i.e., how many times a satellite flies over the same object in a specific time window), which from the PlanetScope Constellation is about twice daily.

Both of the images were selected because they were taken during cloud coverage of less than 1%, which minimizes signal disturbance[5]. Clouds represent a particular problem in remote sensing, because they obscure and can physically cover the ground, making it invisible to the satellite. Additionally, clouds cast shadows that can alter the spectral signature of the surface (e.g., a darker pixel on a water bodies would normally indicate deeper water, unless it is made darker due to a shadow insisting over it).

### *3. Date of acquisition*

The study site is affected by seasonal weather and ground cover (snow), hence the images have been selected avoiding the winter season due to possible presence of thick and highly reflective surfaces (ice/snow), which can interfere with the sand spectral signature[6].

We wanted to determine if Essex River Inlet recovered after erosional-depositional processes resulting from 2018 extratropical storms events by identifying stable/unstable/changed areas. To reconstruct the response of the system, we have used images have been collected approximately in the same period in 2017 and 2019 (early and mid-fall).

**Table 2.** Imagery features

| | **2017** | **2019** |
|---|---|---|
| Satellite | PlanetScope | PlanetScope |
| # of spectral bands | 4 (RGB + NIR) | 4 (RGB + NIR) |
| Date of acquisition | 13 October 2017 | 5 September 2019 |
| Cloud % | 0% | 0.5% |

[5] Satellites normally see clouds, buildings and sand as almost identical objects. That is caused by the high reflectance of these kind of surfaces. An accurate classification based on distinct spectral signatures between these objects is therefore complicated and frequently inaccurate.

[6] Same as clouds, ice and snow also are highly reflective surfaces.

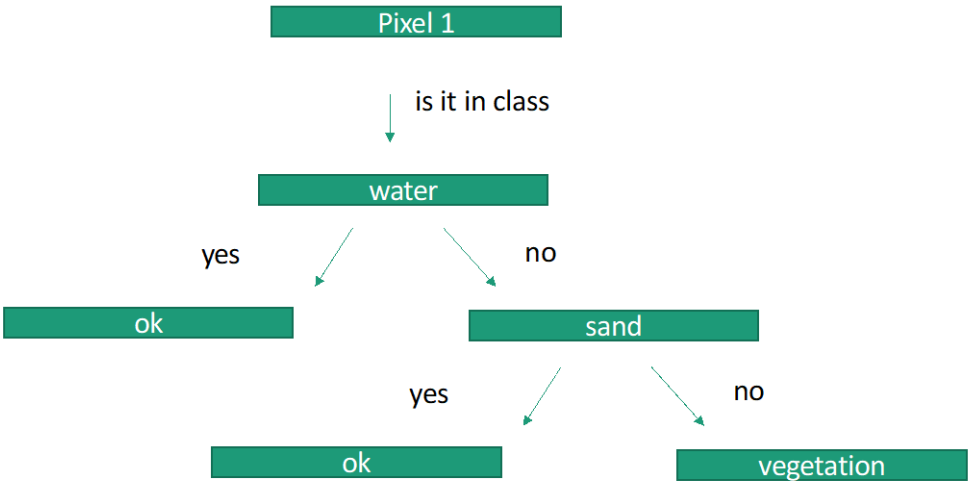


**Figure 17.** Decisional workflow of a basic Decision Tree algorithmrun with 3 stable and 4 unstable classes.

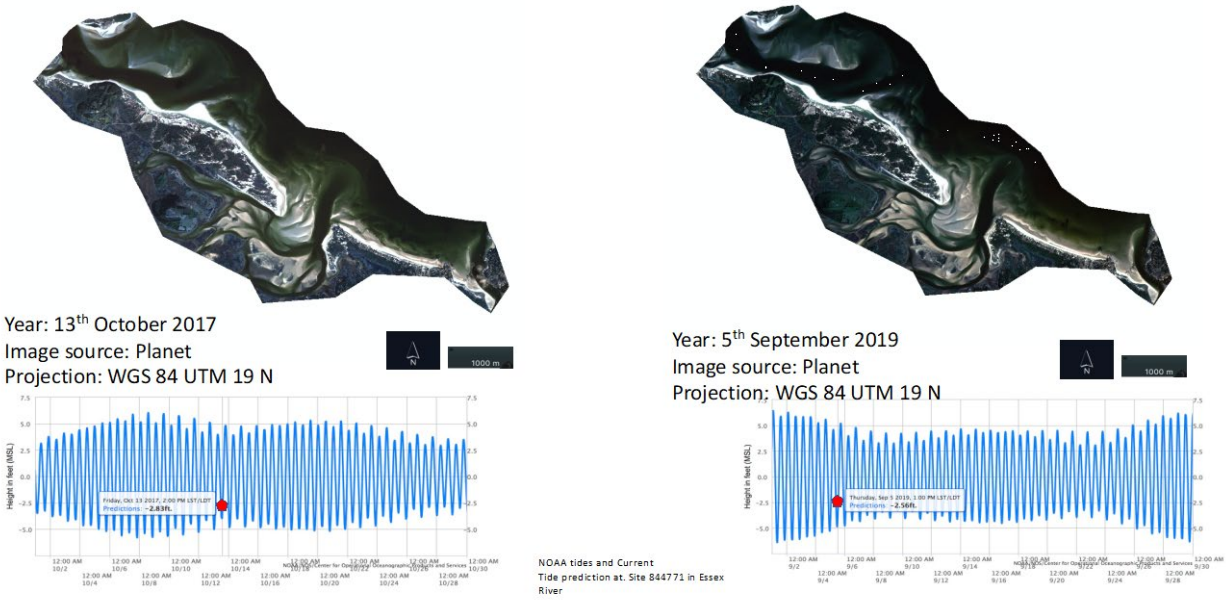


**Figure 18.** PlanetScope stack RGB and NIR bands displayed in RGB colors. Tidal prediction for October 2017 and September 2019; the red pentagon indicates the tidal elevation at the time of data acquisition.

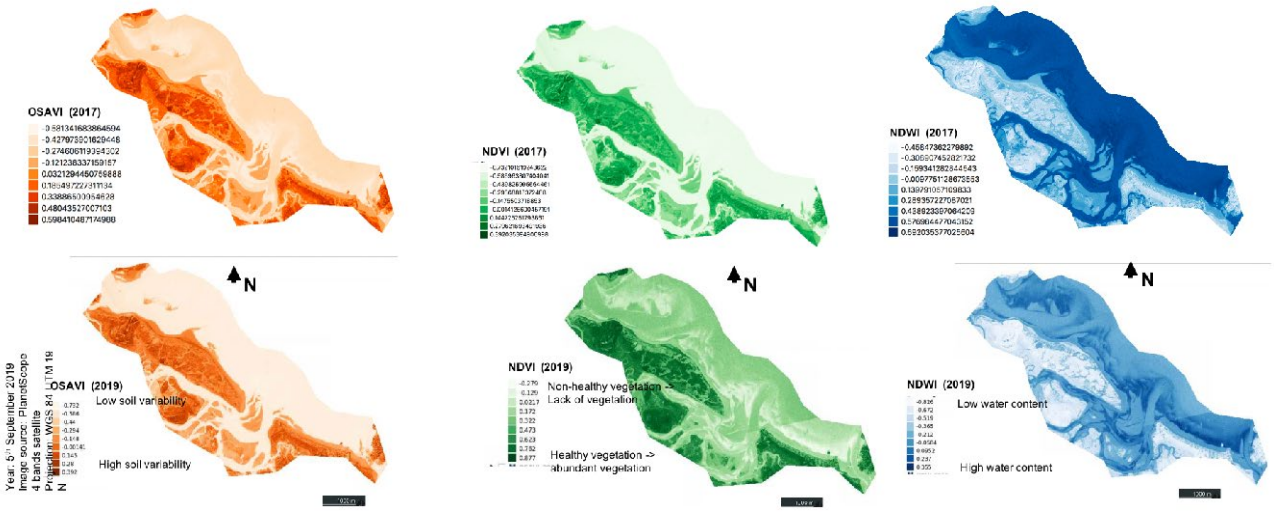


**Figure 19.** Spectral indexes obtained from PlanetScope imagery.. Upper panel is 2017, lower panel is 2019. OSAVI highlights bare soil, NDVI highlights healthy vegetation, NDWI water bodies

### *4. Tidal Conditions*

The mesotidal range (3.0 m) of the region produces strong tidal currents at Essex River Inlet and within Essex Bay and at high tide cover the shoals (both in the river's mouth and in front of Castle Neck beach), as well as the sand in the low tide terrace with more than a meter of water. Thus, an additional criterion for image selection was acquisition during or near low tide. The date and time of acquisition have been crosschecked with tidal elevation using NOAA tides and currents website (Figure 18).

### *5. Spectral Features*

We have analyzed the spectral responses of an "image" consisting of a stack, which is the sum of the different spectral signals.

The image analyzed is composed of the four available spectral bands, three Spectral Indexes (SI)and two spectral textures. The stacking has been done with GDAL package in Python code language. The spectral indexes have been computed with a raster calculation in QGIS, and the textures have been created in the R environment. To summarize, the final image contained a total of 16 spectral signals (8 for 2017 and 8 for 2019).

### *6. Spectral Indexes*

The spectral indexes used in the stack represent the common ones used when analyzing vegetated area: vegetation and water indexes (NDVI and NDWI) and a soil detection index (OSAVI) (Figure 18). They have been calculated as follow:

The Normalized Difference Vegetation Index (NDVI) is a normalized SI that highlights healthy vegetation, and is computed as (Jensen, 1986)

$$NDVI=\frac{NIR-RED}{NIR+RED}$$

here, with PlanetScope spectral bands:

$$NDVI=\frac{band4-band3}{band4+band3}$$

Where -1≤NDVI≤0 represents water bodies, -0.1≤NDVI≤0.1 soil and sand bodies water, and NDVI≥0.1 represents different type of vegetation covers.

The second SI computed is Normalized Difference Water Index, considering Green and NIR bands which is able to detect standing water bodies (McFeeters, 1996).

$$NDWI=\frac{GREEN-NIR}{GREEN+NIR}$$

here, with PlanetScope spectral bands:

$$NDWI=\frac{band2-band4}{band2+band4}$$

Lastly, we calculated a soil index, Optimized Soil Adjusted Vegetation Index (OSAVI), that is able to highlight different types of vegetation where the canopy is sparse, and the soil is partly visible. I applied this index specifically for the wetlands area in order to help the classifier in distinguishing them from build-ups and the other general land use class. OSAVI uses a factor (0.16) to normalized the canopy background (therefore it does not range between -1 and +1), and has been calculated as follow:

$$OSAVI=\frac{NIR-RED}{NIR+RED+0.16}$$

here, with PlanetScope spectral bands:

$$OSAVI=\frac{band\ 1-Band\ 4}{band\ 1+Band\ 4+0.16}$$

### *7. Texture*

We calculated the textures for each year using a Grey level matrix (GLCM) statistics. The computation has been done in RStudio. I have calculated the eight GLCM available in the R package GLCM: mean, variance, homogeneity, contrast, dissimilarity, entropy, second moment and correlation. Eventually only Mean and Variance textures have been added to the stack.

### *8. The Classifier: Decision Tree algorithms*

The decision tree classifier operates selecting a set of samples from the training data and creating a decision tree, an algorithm that learns decision rules each time a new input variable. Ultimately the sample, here the pixel, is assigned to a specific class based on the aggregation of votes coming from different decision trees (Figure 17).

It works analyzing an attribute, called *node*, where the *branch* represents a decision or a rule followed to make the decision, and the *leaf* being the outcome of this decision. Moreover, the Decision Tree's capabilities grow in identifying complex settings. The algorithm is based on training a model in order to have it predict the class or value of the target variable by learning simple decision rules inferred from prior data (training data).

### *9. Training data selection*

Training data are sets of pixels individually selected in GIS in forms of selection of single pixel or polygons containing pixels belonging to the same group, that are then manually allocated into a specific class. As the name implies, these data are used to train the algorithm in properly identify pixels. A good set of training data is fundamental for a proper classification with machine learning algorithm, and good practice is to use a minimum of 200 training data. Here we have chosen to adopt 245 training data (i.e., 245 pixels) variously allocated in different classes based two main criteria: the significance of the class itself (i.e., more pixels for change classes) and the possible difficulties for the algorithm to identify it (e.g., ocean water has the least importance and the easiest spectral signature, hence we allocated the least number of training data for this class).

### *10. Accuracy Evaluation*

The accuracy assessment was done in agreement with the instructions provided by the BEEODA protocol (Olofsson, 2009), consisting of a series of subsequent steps including: sample design, response design, and analysis of the accuracy (see below).

**a. Sampling Design.-** There are many different types of sampling designs, including stratified, simple, and random, which are the most common. In simple random sampling, each element in the class has the same equal probability of being selected to be classified, whereas in stratified random sampling strata are defined from different class, and then random sampling is performed into each stratum (i.e., into sub-set of population belonging to each specific class). To determine

the size of the sample, some intermediate steps must be followed. Knowing the size of each class in pixels (-hist flag in Gdal python package), it is possible to calculate the weight f 1):

$$w_i = \frac{n_i}{\sum_{j=1}^{5} n_j} \quad (1)$$

After that, the sample size is calculated using equation 2:

$$n \approx \left( \frac{\sum w_i S_i}{S(\hat{p})} \right)^2 \quad (2)$$

where $S_i$ is the standard error for the stratum $i$, defined as $S_i = {}^{p}pi(\overline{1 - p_1})$, and $p_i$ proportion of the $j$ class in stratum $i$. To clarify, we have assigned the higher $p_1$ to the two most important classes related to the wetlands and the sand classes. Using this methodology, it is possible to calculate the number of total samples for the all the strata, following Cochran (1977).

The ideal number of pixels to be sampled is approximately 289. To reduce computation time, this number was reduced to 200.

After determining the sample size and its allocation, we used a stratified random sample script that has produced a shapefile with the samples (Figure 20).

| | | STABLE LANDCOVER | | | CHANGED LANDCOVER | | |
|---|---|---|---|---|---|---|---|
| Class | stable water | stable sand | stable vegetation | sand to vegeta | sand to water | vegetation to sand | water to sand |
| area | 1399142 | 99921 | 332336 | 32220 | 230552 | 11443 | 444846 |
| Wi in % | 54.8584177 | 3.917763854 | 13.03043373 | 1.26330152 | 9.03962422 | 0.448664163 | 17.4417948 |
| Wi | 0.54858418 | 0.039177639 | 0.130304337 | 0.01263302 | 0.09039624 | 0.004486642 | 0.17441795 |
| pi | 0 | 0.0001 | 0 | 0.2 | 0.3 | 0.2 | 0.3 |
| Si | 0 | 0.0099995 | 0 | 0.4 | 0.45825757 | 0.4 | 0.4 |
| S(P) | | | 0.005 | | | | |
| n (theoretical) | 561.041386 | | | | | | |
| n (actual) | 245 | | | | | | |
| allocation | 25 | 45 | 25 | 35 | 40 | 35 | 40 |

**Figure 20.** Reference data table with sampling size, allocations and weights.

**b. Sample Response.-** The following step involves checking agreement between the classified map and the reference data. This procedure is done by manually checking each of the reference pixel. This step is crucial because the final classification and area estimates will rely on the correct identification of the units in the sample. This passage has very often some challenges, in particular for the attribution to the proper class for those pixels falling in the channels or in the shallow water on the shore. A major rule of classification of samples have been applied as follow: pixels that were falling on the edge of a group of pixels of the same class were assigned to a change class if they were in a stable class in 2017. An example is a pixel that in 2017 was in stable forest and in 2019 is on the edge/boundary with sand. In this case it was decided to assign the pixel to a change class because the landcover has shifted.

Similarly, pixels that where on almost exposed shoals in 2017 and in 2019 are visible but clearly more submerged have been assigned to unstable classes.

**c. Analysis.-** With the correct assignation done, the following step consists of computing the error or *confusion* matrix based on the mapped area for each class. Since the classes have different size and importance, it is necessary to estimate the correct area proportions for each class. This is done computing area proportion with Eq. 3

$$p_{ij} = \frac{w_i n_{ij}}{n_{ij}} \tag{3}$$

Where $w_i$ is the weight associated to the sample belonging to stratum $i$, and $n_ij$ is the sample count in the cell $i$ ,$j$ is the total counts for sample $i$ in the map.

The total area proportion for each class is then re-converted into pixels counts dividing the total of each class' area estimate (from the area proportion error matrix) by the map pixel counts for that class (from the sample counts error matrix). It is also possible to convert the area proportions from pixel to metric area (in $m^2$) associated with each class, and that can be achieved by multiplying the reference labels area times the extent of a pixel in the Landsat framework (30x30$m^2$).

Following this, it is necessary to calculate the standard error for the computed area estimates, as follow (Eq. 4)

$$S(\hat{p}_j.) = \sqrt{\sum_i \frac{w_i \hat{p}_{ij} - \hat{p}_{ij}^2}{n-1}} \tag{4}$$

Lastly, it is possible to compute 95% confidence intervals based on the standard errors calculated with Eq. 4, simply multiplying them times 1.96. The final area estimate will then be (Eq. 5):

$$A_{bj} \pm 1.96 S(A_{bj}) \tag{5}$$

where $\widehat{A}_j$ is the area proportion, $\widehat{A}_j$ the std error, and 1.96 the conversion factor.

The total area will be derived from the area estimates, with the corresponding confidence intervals, as a sum of the change classes.

**d. Accuracy Assessment -**Once assigned the map label and the reference label to each of the sample units, the following step is to compute a confusion matrix, or error matrix. This is a table that allows a visualization of the performance of the supervised classification algorithm. From that we perform the actual accuracy assessment.

The error matrix can be expressed in terms of counts from the map or calculated with the estimator defined in Eq. 3. The table in Figure 20 represents the assignation of pixels to different classes, where the rows $i$ correspond to the map's classes, and the columns $j$ to the classes belonging to the reference data.

Elements that will fall on the diagonal will be the correctly classified ones, showing agreement between the map classification and the reference data, while elements outside it (above or below), represent commission and omission errors. Commission error happen when a pixel (or estimated area) is assigned to the wrong class, and represent false positive, omission error when a pixel (or estimated area) is not assigned to the proper class therefore represents false negative. The fraction, or percentage, of commission error is given by the sum of all the pixels that have been assigned to the *i* class (row on the confusion matrix) divided by the total of the elements in that class. Omission errors fractions (or percentage) are calculated by the sum of the element that should have been assigned to class *i* (column on the confusion matrix) but have actually been assigned to another one, divided by the total of this class.

The steps above are fundamental to calculate the accuracy of the classification, that can be distinguished between overall, producer's and user's accuracy.

**e. Overall accuracy**: It is the actual proportion of the map that has been correctly classified. it is calculated summing the correctly classified area proportions (the element on the diagonal) and dividing the sum by the total numbers of values (Eq. 6) (Olofsson et al., 2013).

$$Ob = \sum_{j=1} \hat{p}_{jj} \quad (6)$$

**f. Producer's Accuracy**: This accuracy shows the probability that the value classified to a specific category in the map belongs to that class on the ground, meaning that it has been classified correctly. Producer's accuracy takes into account the fraction of properly predicted values with respect the total of the values belonging to that class, following Eq. 7

$$\hat{P}_i = \frac{\hat{p}_{jj}}{\hat{p}_{.j}} \quad (7)$$

**g. User's Accuracy**: this is the "probability that a value predicted to be in a certain class is really in that class"[7]. User's and Producer's probability are complementary. User's probability is calculated as follow (Eq. 8):

$$\hat{U}_i = \frac{\hat{p}_{ii}}{\hat{p}_{i.}} \quad (8)$$

[7] https://www.l3harrisgeospatial.com/docs/CalculatingConfusionMatrices.html

## D. Beach Morphological Changes

### *1. Beach Profiling using Real Time Kinematics*

To determine seasonal morphological changes and effects of storms to Crane Beach, we established six Beach Profiles stations in the dunal area along the length of the barrier from the drumlin outcrop in the north to the spit end in the south next to Essex River Inlet (Figure 21). A general view of the beach and other environmental settings at Castle Neck are shown in Figure 22. The beach profiles stations consisted of two metal fence posts aligned perpendicular to the strandline. The RTK Surveys were completed with the help of the Trustees at Crane Beach.

Each profile has been chosen taking into account:

- Its position with respect the hand grabbed sediment samples collected during several surveys in 2019
- The proximity to significant beach and tidal features, such as a rapidly accreting sand bar (Profile 1), proximity to a dune that will be likely impacted by storm winds (Profile 4), proximity to ongoing dune and beach erosion marked by garnet bearing sand (Profile 0)
- Conservation and preservation of Piping plovers nesting sites.

The profiling survey consists of steps:

- Positioning the base station, a stable sensor that acts as reference point to calculate elevation. The base station transits its position using Bluetooth to the receivers. We normally chose to place it on the northern protuberance because of its exposure, Bluetooth signal is not often lost due to topography.
- Walk along the chosen transect with a receiver positioned at the top of a 2m long pole. The profile is measured following a as straight as possible line stretching between the dunes and the low-tide terrace. The receiver pings a signal to the base station, containing x,y,z values. Coordinates are collected at a high frequency in order to maximize the number of points defining each profile.
- Take hand-held GPS readings for both front and back stick and seaward end of the profile (this is a precautional measure in case the pole has shift in between surveys).

Photographs illustrating the Real Time Kinematic survey, stakes and other beach features are shown in Figures 21-27.

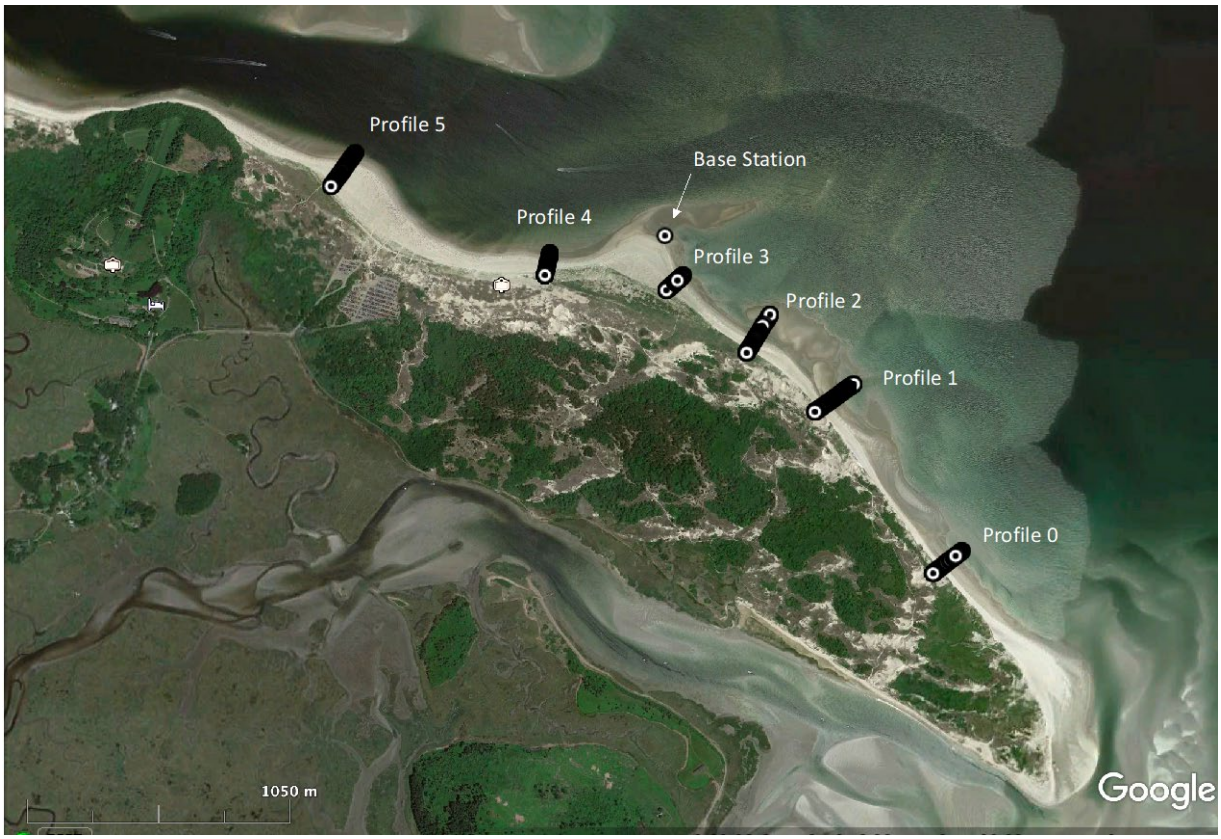


**Figure 21**. Beach Profile stations.


**Figure 22.** Castle Neck environments.A concentration of garnet sand along upper berm at mid-barrier. B. Large dunes at southern end of barrier have experienced recent dune scarp erosion. C. Boardwalk crossover at parking lot. D. Backbarrier marsh system. E. Tidal creek devoid of water at low tide.

**Figure 23**. RTK Base station located at the mid-island beach protuberance. This site provided an unobstructed signal line to all the profiles.

**Figure 24**. Scientists recording RTK beach profile survey.


**Figure 25**. Survey team in the dunes at the metal fence location

**Figure 26.** Close-up view of the metal fence post arrangement. This alignment aide the survey team run the same transit profile.

**Figure 27**. Example of a profile along the width of the beach to the low-tide terrace.

The beach surveys have been run on three occasions during 2020 (see Table 3 for survey information). The data were plotted in Excel and then for each site the profiles were overlaid to show morphological changes. These overlays also allowed us to calculate volume changes resulting erosional and depositional processes. A discussion of the beach profile changes are given in Appendix 1.

**Table 3.** Beach Profile Information

| Date | Geoid | Coordinate system | Unit | Accuracy | Starting time and tide |
|---|---|---|---|---|---|
| 6/16/2020 | 2018 | WGS84 | Meters | cm | 12.54 pm, low tide |
| 9/8/2020 | 18 | NADV88 | Meters | cm | Low tide |
| 10/11/2020 | 2018 | WGS84 | Meters | cm | 11.35 low tide |

### *2. Shoreline Mapping using GIS Methods*

We have analyzed shorelines changes of Castle Neck over the past 80 years, from 1938 to 2018 using a combination of aerial photographs and satellite imagery (Landsat 7 and 8 OLI, 30 m resolution) to trace the shoreline profiles of Crane Beach (from the northern protuberance to the southern spit at Essex River Inlet extending to the northernmost portion of Coffins Beach. Each aerial historical shoreline has been compared by overlaying the contours of different years over a 2018 Landsat image; then it has been identified the section with maximum modification between the historical shoreline and the 2018 one by tracing a perpendicular line connecting the two shorelines at the site where the more significant variation was identifiable. Additionally, when multiple shorelines were available for the same decade, transects of maximum erosion and maximum accretion within the decade have been identified.

We have used QGIS and ArcMap to produce to trace shorelines and creates the maps of shoreline variation for each decade.

Decadal information for the historical shoreline analyses are shown in Table 4.

**Table 4.** Historical Data Base

| Decade | Year(s) | Maximum variation within decade | Maximum accretion | Maximum erosion |
|---|---|---|---|---|
| 30's | 1930 | no | Yes | yes |
| 60's | 1960,1965 | Yes | Yes | yes |
| 70's | 1972(spring, summer, fall), 1973 | Yes | Yes | yes |
| 90's | 1991,1992,1995 | Yes | Yes | yes |
| 2000 | 2000 | No | Yes | yes |

## E. Bathymetry and Hydrographic Data Collection

### *1. Bathymetry*

The two major input parameters for hydrodynamic modeling are 1. detailed bathymetry, including all the major and moderate-sized channels in the system, and 2. tide-level measurements over at least a fortnightly cycle at several locations throughout the estuary. The shallow nature of much of Essex Bay and Essex River estuary means that Lidar data provided most of the bathymetry required for the modeling (Figure 28). However, for the deeper channel areas, Lidar does not reach to the bottom and those depths were unknown. As seen in Figure 28, there are numerous channel sections within the study area that exceed 2 m. In these deeper regions, we ran a boat-mounted Acoustic Doppler Current Profiler (ADCP), which continuously records depth, as well as velocity through the water column (Figure 29). Note that

at the tidal inlet throat, there were numerous transects across the channel that extended over a period of several hours (see location in Figure 29). The data collected during this time allowed us to determine an accurate cross-sectional area of the inlet throat, as well as record detailed velocities for calibrating the hydrodynamic model.

### *2. Hydrodynamic Deployments*

A major second field task involved measuring tidal elevations, suspended sediment, and wave heights within the modeling area (the domain). These deployments assisted in assessing the depth and frequency of tidal and storm flooding and movement of suspended sediment. Timing of the deployments was designed to capture elevated tides (perigean spring tidal ranges) and possible storm surge conditions. We used a system of Onset Hobo water level loggers (n = 5), RBRsolos (n = 2) and Notek Aquadopp current profilers with Campbell Scientific Optical Backscatter Sensors (OBS) (Figure 30). The hobos measure water level every few minutes while the RBRsolos have a sampling frequency up to 16 Hz (16 measurements per second) and are ideal for measuring short period waves propagating in shallow water. The Aquadopps provided water level and current velocities, and suspended sediment data were obtained from the OBS. The instruments were deployed during late summer to late fall in order to collect data during a northeaster. These data were used to calibrate and validate the hydrodynamic (Delft3D and Swan) models. In addition to static current measurements, we used a boat mounted synoptic Acoustic Doppler Current Profiler to measure the flux through the inlet. A sample of the current velocity and tidal elevation data are given in Figure 31.

Despite our best efforts to secure the instruments to the bottom and place them at locations out of boat traffic lanes and lobster pot sites, the Hobo behind Castle Neck and the Aquadopps east of Conomo Point were lost. The current meter was anchored to the bottom with weights and a tag line and mushroom anchor were rigged with a buoy and line to the surface. This arrangement reduces buoy dragged and possible movement during strong current velocities. Despite these efforts the meters could not be located even though they were located using our RTK system that is accurate to within less than 30 cm (1 foot). Additionally, we dragged for the instruments on two occasions at extreme low-tide and sent a team of SCUBA divers over the side who searched for the equipment for more than hour. Our best guess is that the equipment was stolen; the loss totaled more than $35 k. Fortunately the loss of data did not compromise our modeling calibration.

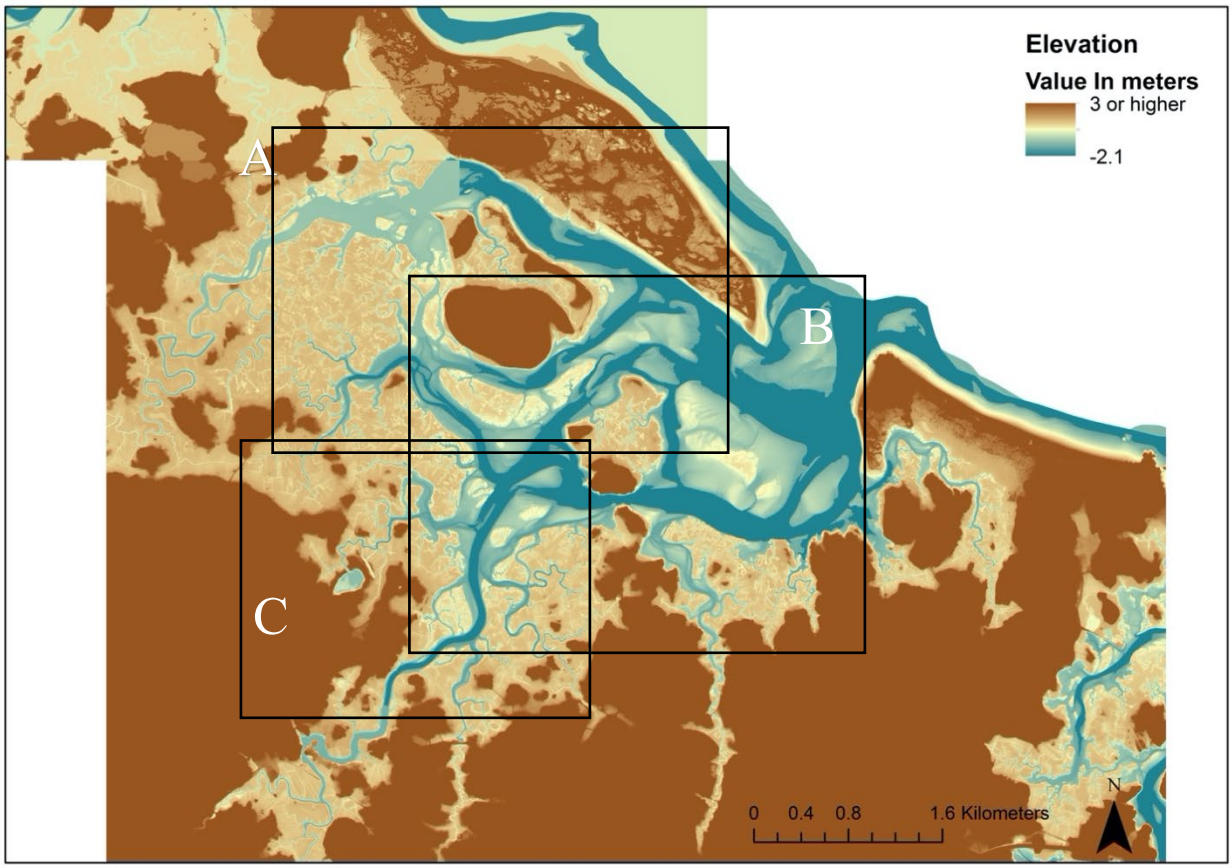
Elevation
Value In meters
3 or higher
-2.1
A
B
C
0 0.4 0.8 1.6 Kilometers
N

A

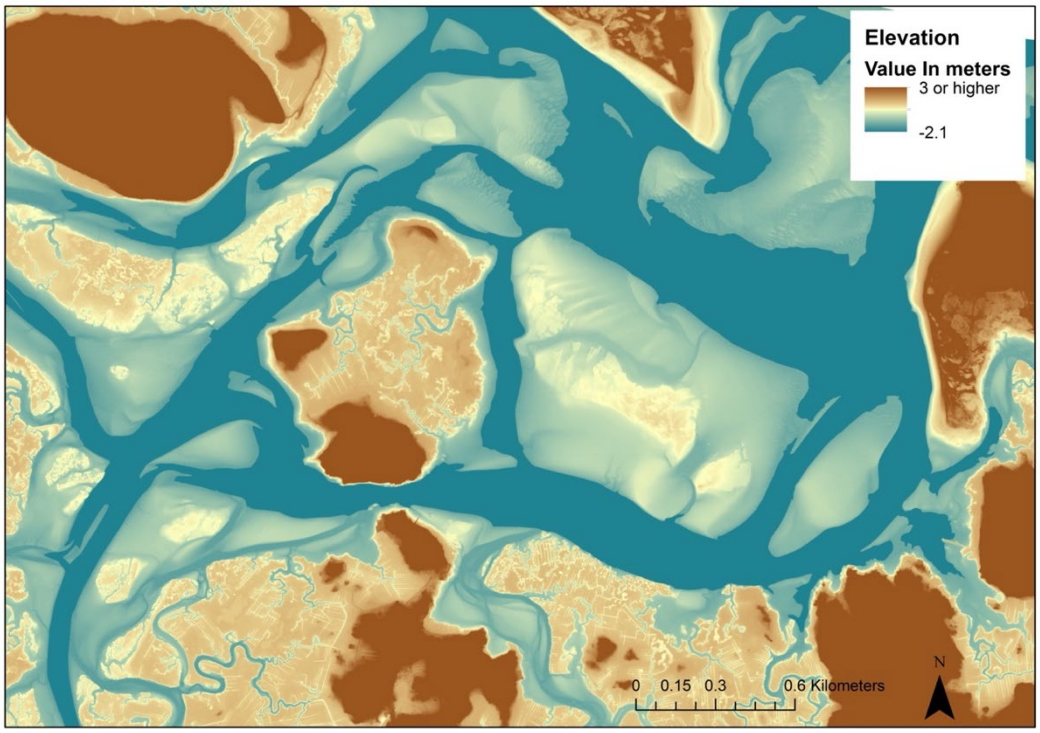
Elevation
Value In meters
3 or higher
-2.1
0 0.15 0.3 0.6 Kilometers
N

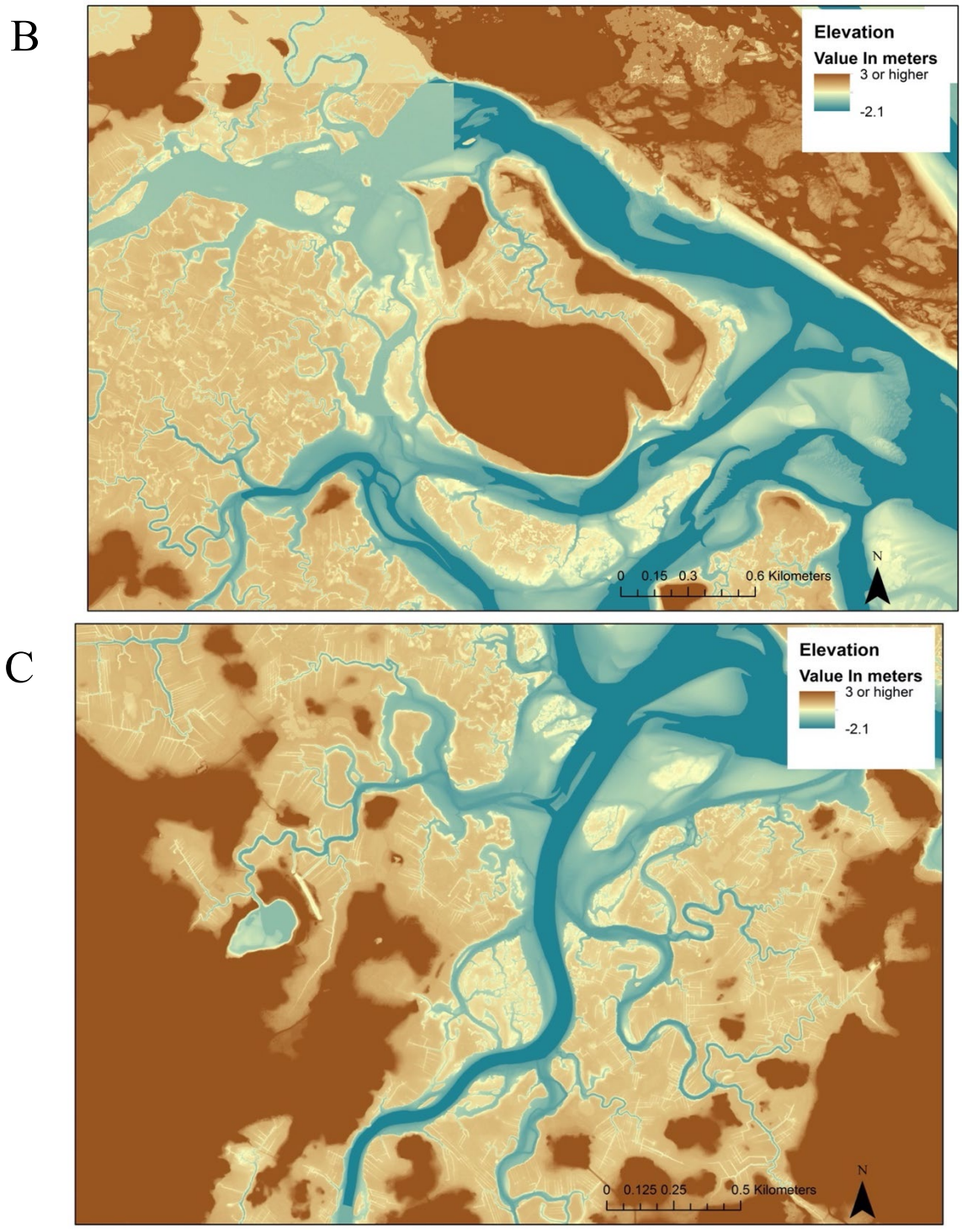


**Figure 28.** Lidar data for the study area. The areal coverage in the enlargements of panels A, B, C are show in the first panel.

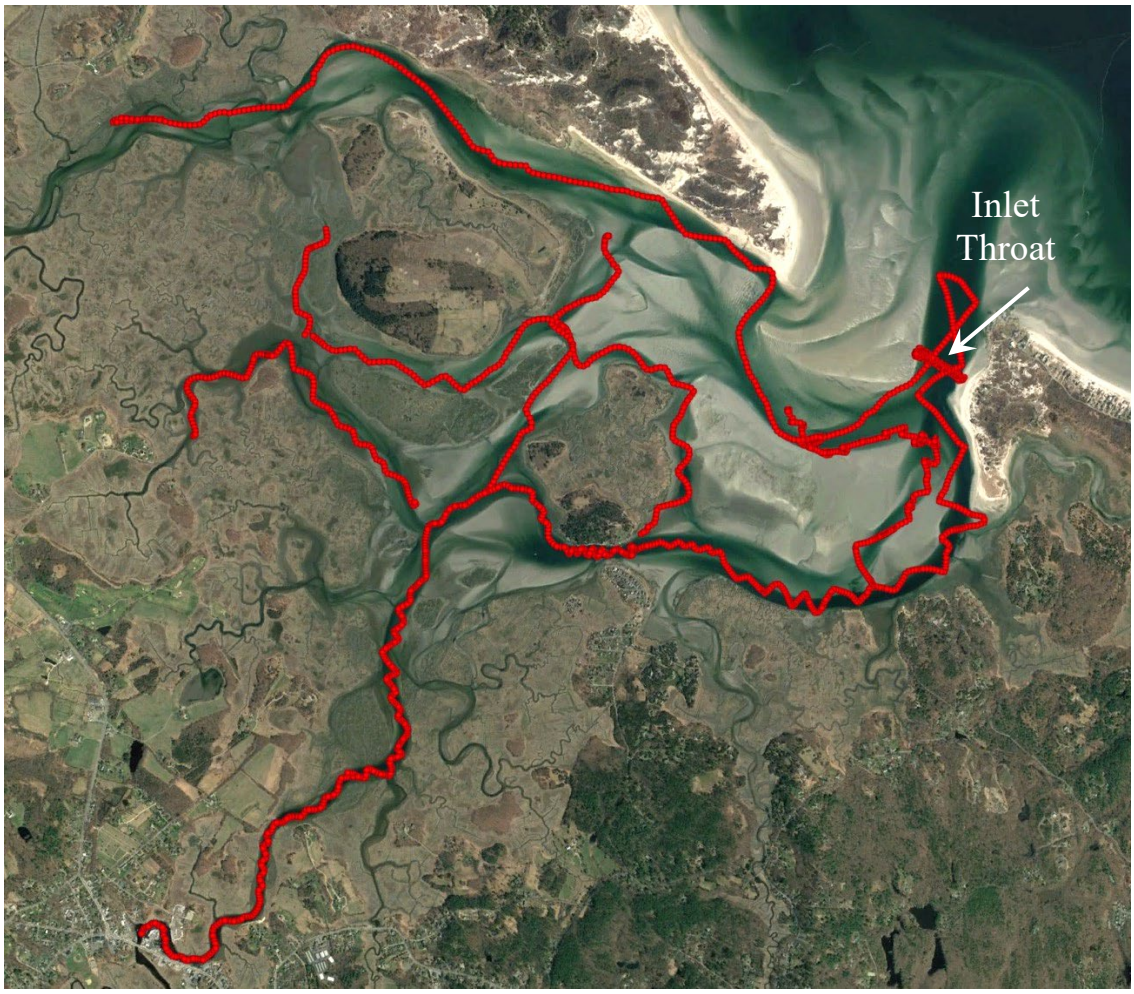


**Figure 29**. Tracklines where additional bathymetric data were collected. Typically, Lidar does record channels of deeper depths. These data are essential for running the hydrodynamic model.


Figure 30. Location of instrument deployments. Hobos measure water level and the BUP and WOP instruments recorded water level, current velocity and current direction over a vertical profile.

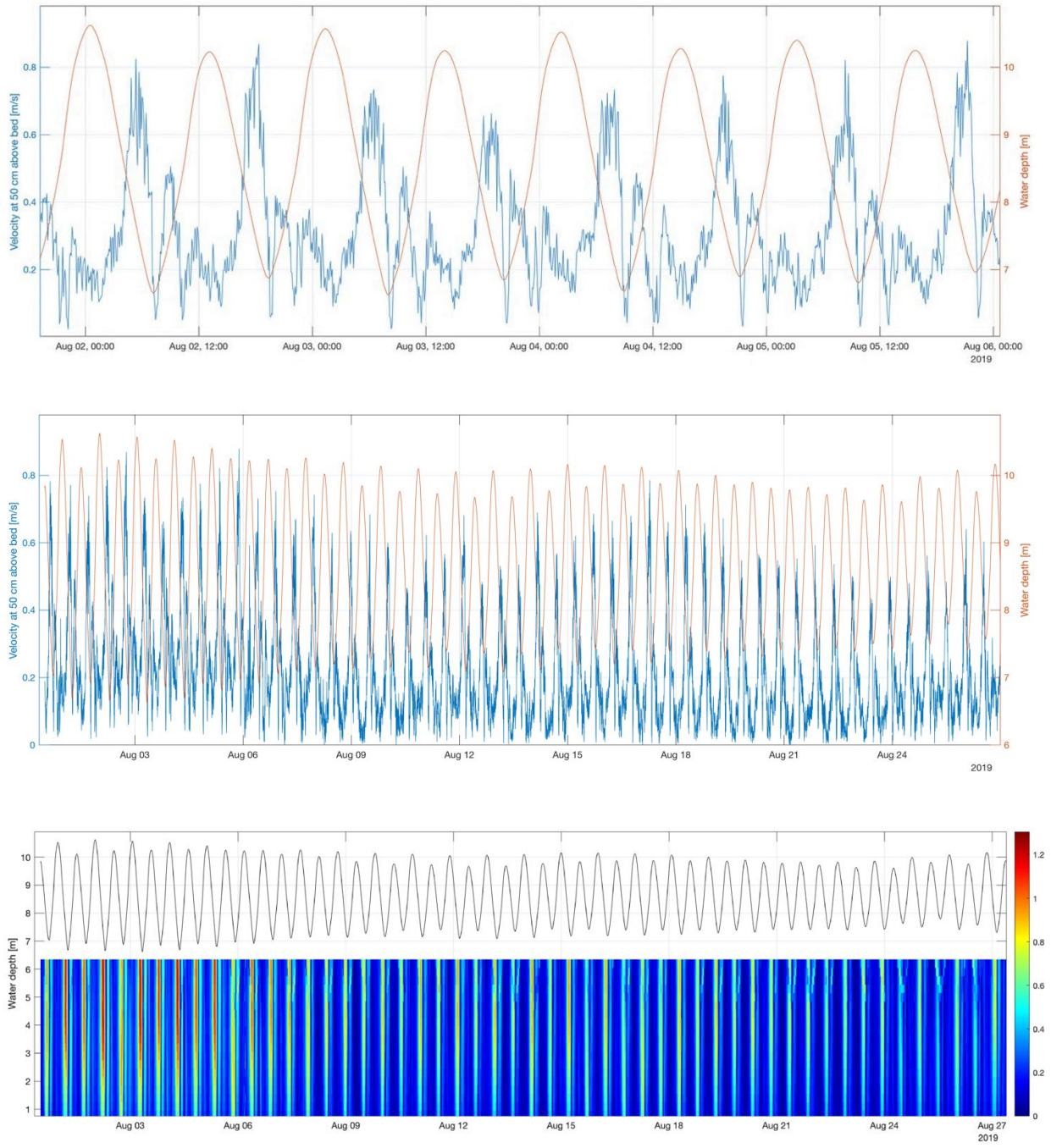


**Figure 31.** Tidal observations.Top panel- Velocity time series for the 2-6 August 2019 period. The station located inside Essex Bay in the channel west of Cross Island. The red line is the tide curve and the blue is the velocity curve. Note the strongly ebb-dominated current. Middle panel- 1-25 August 2019 velocity and tide time series. Bottom panel- Tide curve for 1-27 August 2019 period.

# VI. HYDRODYNAMIC MODELING

## A. Delft3D implementation

Present-day hydrodynamic and sediment transport patterns are assessed using the Delft3D modeling suite (Delft3D; Lesser et al., 2004), which has been used successfully to study storm surge (Sakib et al., 2015) and wave dynamics throughout the world. The Delft3D hydrodynamics and wave modeling suite is a numerical process-based model that is capable of resolving hydrodynamics, sediment transport, and resulting morphology under the combined effects of currents and waves (Lesser et al 2004). The Delft3D suite can be used to simulate flow and wave propagation in coastal and marsh environments, including fine-scale circulation and over-marsh flow in saltmarsh or mangrove (e.g., Liu et al 2018; Sakib et al 2016; Caldwell et al 2014; Hanegan and Georgiou 2015; Sullivan et al 2015). The effects of surface waves and wave-current interactions were included by coupling the flow model with the third-generation spectral wave model SWAN (Booij et al., 1999) within Delft3D modeling suite.

### *1. Construction of Grid and Model Bathymetry*

The modeling effort was carried out on two computational grids of different spatial extent but identical resolution where the model domains overlap. The regional Northeast Atlantic mesh extended from New Hampshire north Atlantic Ocean side to Cape Cod to the southeast Atlantic Ocean. The nearshore grid covers the plum island inlet to the north to the Cape Ann to the south including Essex Inlet system which is area of interest for this study. The Northeast Atlantic mesh has a 400 m constant resolution whereas the resolution of the nearshore computational mesh varies from 40-120 m in the offshore, reducing to a resolution of 10-20 m in the vicinity of the barrier islands, tidal inlets and within the backbarrier.

The model bathymetry shown in Figure 32 uses the most recent bathymetry-topography data available for the area: (a) regional bathymetry for the coastal ocean based on the Coastal Relief Model from NOAA, (b) 2011 LIDAR, 2014 & 2015 Sandy LIDAR obtained from the US Army Corps of Engineers, and (c) 2015 & 2019 BU bathymetry survey. In addition, the RTK data further resolved topography. All elevation data was converted into a common horizontal and vertical datum (UTM zone 19 meters, NAVD 88 meters) and interpolated into the computational domain using spatial triangular interpolation methods using Delft3D QUICKIN tool. Finally, marsh elevation surfaces for future SLR scenarios were inputted from results in defining the sea level positions.

### *2. Boundary Conditions and Bottom Roughness*

During the model calibration and validation process, tidal constituents (see Table 5) were forced for each open boundary node using the tidal database of TPXO 7.2 Global Inverse Tide Model (Egbert et al., 2002) at the open boundary of the regional grid. Tidal amplitude and phase were extracted for each of the boundary nodes, allowing for water level variation across the open boundary. Essex nearshore model boundary data were extracted from the regional model to force

the hydrodynamic of the nearshore model during model validation period. Neumann zero gradient boundaries were used on both cross-shore boundaries (north and south). The NACCS analysis storm database was used to select representative storms for this study. Surge, wave parameters and wind field of selected storms for this study were directly applied at the calibrated and validated essex nearshore grid boundary nodes to force the hydrodynamic of the storms. The wind-generation module within SWAN was activated, including water-level setup (increase storm surge elevation) due to waves.

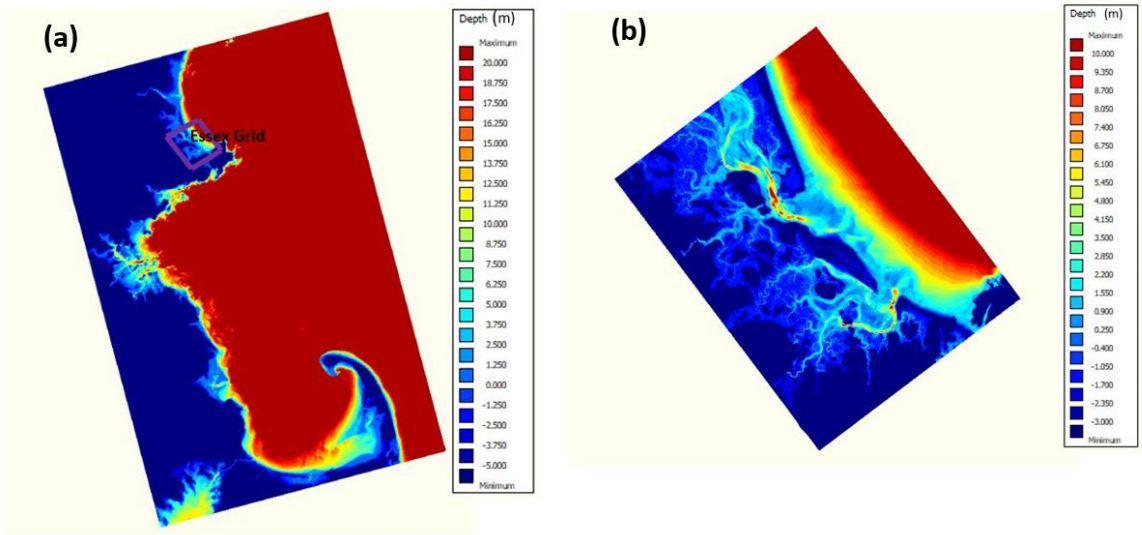


**Figure 32** Computational Domain and Bathymetry. (a) The regional Northeast Atlantic bathymetry (b) The nearshore Essex bathymetry.

**Table 5.** Description of tidal constituents used in this study

| **Tidal Type** | **Tidal Constituent** | **Description** |
|---|---|---|
| Semidiurnal | M2 | Principal Lunar |
| | S2 | Principal Solar |
| | N2 | Larger lunar elliptic (monthly variations in lunar distance) |
| | K2 | Luni-solar declination |
| Diurnal | K1 | Principle Lunar |
| | P1 | Principle Solar |
| | O1 | Principle Lunar |
| | Q1 | Larger lunar elliptic (monthly variations in lunar distance) |

Manning's roughness value is used to apply the friction generated by bed. The stress generated as water flows over the bottom is formulated using a quadratic friction law with a drag

coefficient that is defined as a function of bed or bottom roughness. The roughness is parameterized by setting a roughness value that can either be constant over the full domain or vary to represent the natural variation in bed roughness of different environments. For this model, an approach was used which assumes the roughness value is dependent on the water depth and the vegetation type. In the implemented formulation**,** higher n values correspond to rougher beds. Figure 33 presents the spatial variable range of n values for various floodplains, barrier islands, channel types and marsh platform to show the applicability of calibrated model values.

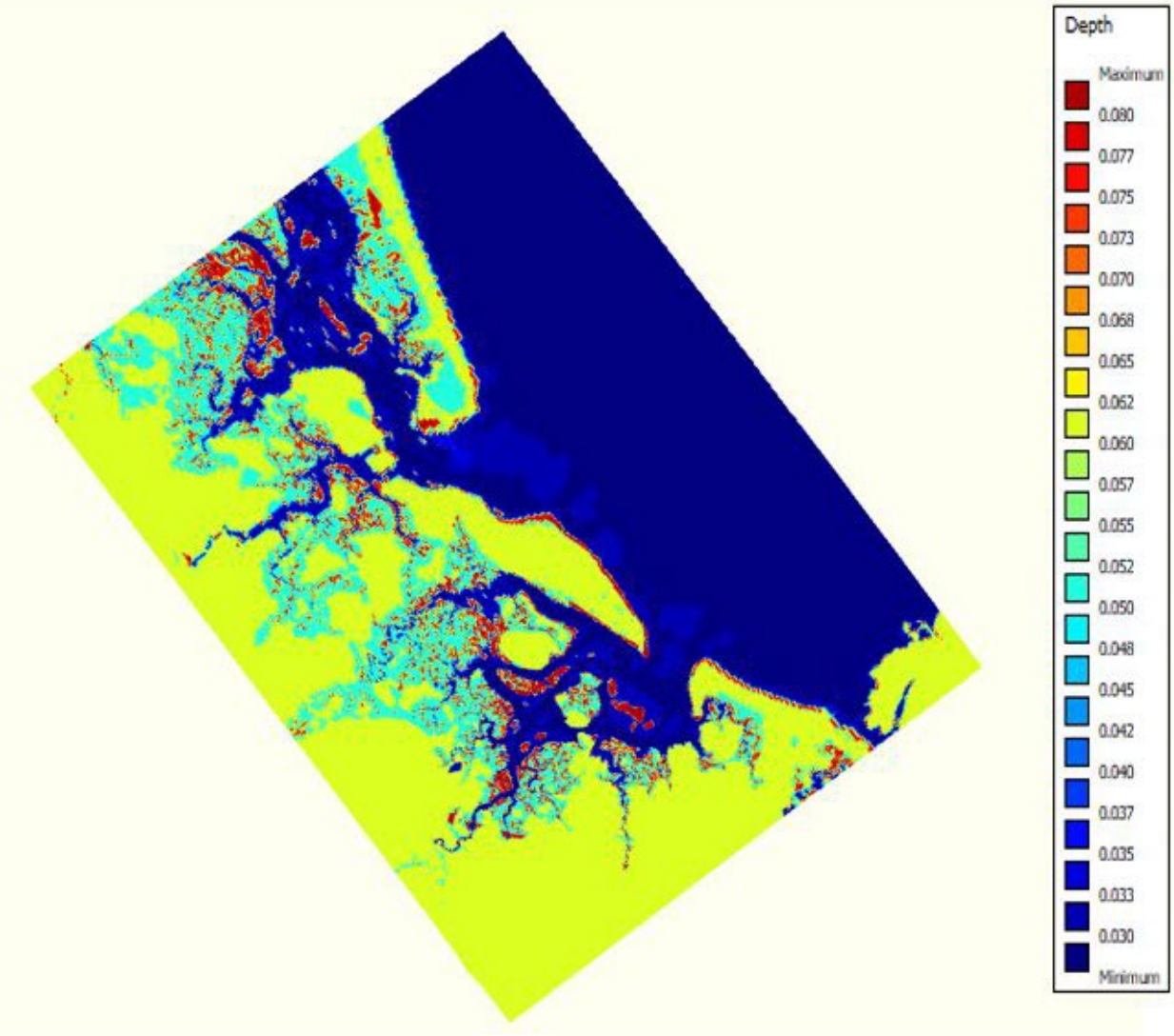


**Figure 33.** Space-varying Bottom Roughness Mapfor Essex nearshore model domain (color indicates Manning's n value which is shown here as equivalent depth value)

### *3. Calibration and Validation*

The model calibration process involves adjusting relevant model parameters until a representative dataset describing the fundamental processes of interest is produced by the model. This is done so until model results meet certain metrics established for the project (Rodrique and Meselhe, 2013). Bottom Roughness (manning's n value) is used as the model calibration parameter. Performances of the model during the calibration exercises are evaluated by computing model performance metrices (Rodrique and Meselhe, 2013). Typically, in hydrodynamic models, variables such as water level or stage in the river, flow distribution, velocity, sediment concentration and salinity or temperature are considered. The variables used during the calibration processes can vary according to the model objectives. For this effort, in support of the study objectives, the model was calibrated for water level during non-stormy conditions.


**Figure 34** Location of the deployments.

The model was also validated using data collected under non-storm conditions by leveraging existing observations collected by the BU team in 2019 which includes a nearshore (~10 m) deployment along the Essex Tidal Inlet. During 2019 campaign, instrument tripods were deployed, and hydrodynamic data were collected continuously for almost entire August period.

The hydrodynamic model was calibrated using measured water levels at six locations shown in Figure 34. The calibration simulation was performed for a 27-days period from July 31 to August 27, 2019. Figure 35 presents plots comparing measured and simulated water levels at the six calibration locations where data were available. The results show that the model reproduces both the tidal range and phase very well at all locations, with only a slight overprediction of tidal range at Hobo 1 compared to measurements. This deployment location is in a part of a narrow creek in the domain where the model grid is not sufficiently refined.

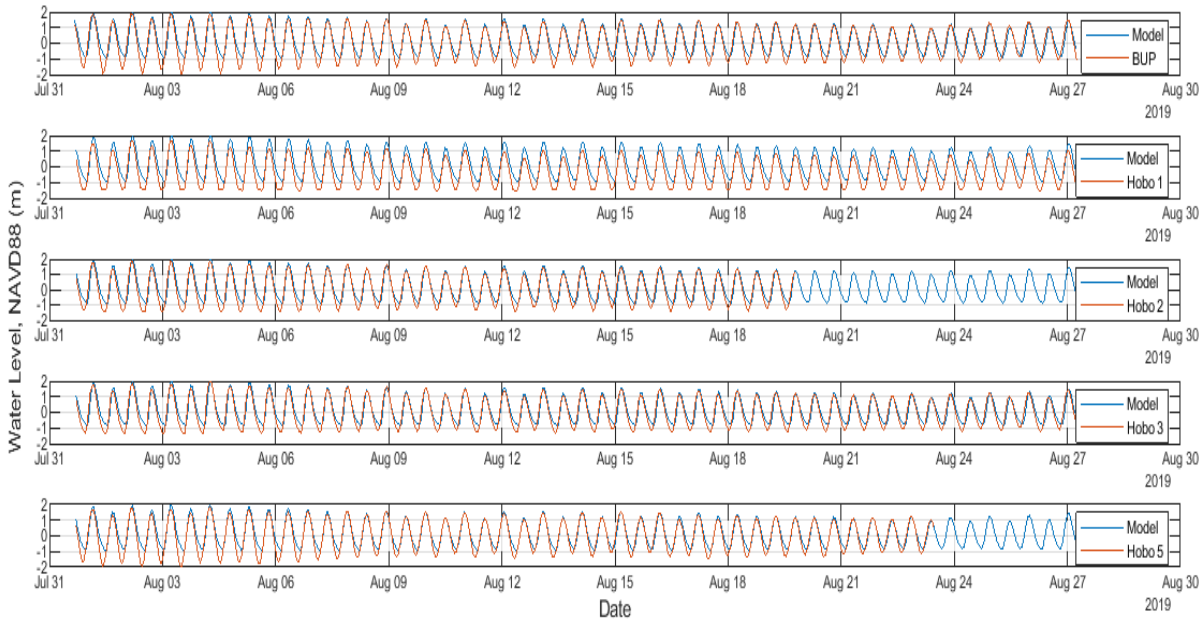


**Figure 35**. Model validation. Showing a comparison of modeled (blue) and observed data.

### *4. Model Performance Metrics:*

Model calibration is an endless process. There is always another set of parameters that will produce a better fit to the measured data. To quantify the agreement between the modeled and measured data it is important to establish a set of metrics to help identify acceptable model performance. Model Performance metrics were created for three goodness-of-fit statistics: (1) the root mean square error (RMSE), (2) the Pearson product-moment correlation coefficient, and (3) normalized bias (Meselhe and Rodrigue, 2013). Hourly Water level data was used for model validation. The RMSE is calculated as follows:

$$RMSE = \sqrt{\frac{\sum_{i=1}^{N}(M_i - O_i)^2}{N}} * \frac{N}{\sum_{i=1}^{N}(O_i)^2}$$

Where:

M=Modeled Value

O=Observed Value

N=number of observations

A small value of RMSE indicates to a better fit between the modeled and measured data whereas a large value means opposite. The Pearson product-moment correlation coefficient, r measures the phasing between the modeled and observed data (Legates and McCabe,1999). It determines how well the peaks and troughs of the curves line up. The Pearson product-moment correlation coefficient is calculated as follows:

$$r = \frac{\sum_{i=1}^{N}(M_i - \bar{M})(O_i - \bar{O})}{\sqrt{\sum_{i=1}^{N}(M_i - \bar{M})^2}\sqrt{\sum_{i=1}^{N}(O_i - \bar{O})^2}}$$

Where:

M=Modeled Value

$\bar{M}$ = Mean of modeled values

O=Observed Value

$\bar{O}$ = Mean of observed values

N=number of observations

The value of r ranges from -1.0 to +1.0, where a value equal or close to +1.0 is preferred. The value equal +1 or close to +1 means the peaks and troughs of modeled and observed data curves are well matched. Bias ensures that the model is not consistently over- or underestimating critical quantities. Bias value could be positive (overestimation) or negative (underestimation). Bias can be calculated as follows:

$$Bias = \frac{1/N \sum_{i=1}^{N} Ei}{1/N \sum_{i=1}^{N} |Oi|}$$

where N is the number of observation points in the time series, $Ei = Mi - Oi$ is the difference between the model result $Mi$ and the observation $Oi$. Bias refers to the normalized mean error.

A summary of the metrics produced from the calibration process are shown in Table 2. Locations where water level were assessed exhibited good RMSE, r, and Bias values based on acceptable metrics (Meselhe and Rodrigue, 2013), with most stations showing RMSE less than 20%. Phase differences between the model and observations - timing of the high and low water level - were in a good agreement (see Figure 36 and Table 6), with the model slightly over-predicting tidal range at Hobo 1 location, this deployment location however, is in a part of narrow creek in the domain

where the model grid is not sufficiently refined. This overprediction is well within the performance metrics evaluated and was thus not considered significant.

Table 6. List of Metrics Used in the Assessment of Model Performancefor Different Locations

| Station/Location | Variable | Bias | RMSE | Pearson product-moment correlation coefficient, r |
|---|---|---|---|---|
| BUP | Water Level | 0.10 | 0.02 | 0.94 |
| Hobo 1 | Water Level | 0.21 | 0.02 | 0.95 |
| Hobo 2 | Water Level | 0.02 | 0.002 | 0.94 |
| Hobo 3 | Water Level | 0.08 | 0.02 | 0.94 |
| Hobo 5 | Water Level | 0.05 | 0.002 | 0.95 |

### *5. Storm characterization and selection*

An assessment was made of the full suite of NACCS storms to determine a subset to use for detailed modeling of present and future conditions in Essex Bay. The present day Annual Exceedence Probability for water level was determined for a position just offshore of Essex bay, based on the regional scale modeling from NACCS. Maximum storm surge elevation for each storm was determined and compared to the AEP water levels to determine a suite of storms that would describe the annual curve. In total 1150 storms were assessed for their impact on Essex Bay and from these 30 tropical storms and 25 Extra tropical storms were selected to represent a range of annual flood conditions (Table 7, Figure 36). Further description of these storms can be found in Appendix 5.

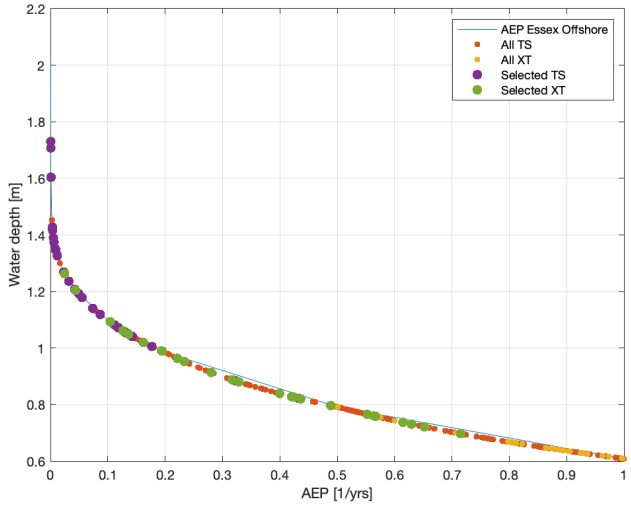
AEP Essex Offshore
All TS
All XT
Selected TS
Selected XT
Water depth [m]
AEP [1/yrs]
2.2
2
1.8
1.6
1.4
1.2
1
0.8
0.6
0
0.1
0.2
0.3
0.4
0.5
0.6
0.7
0.8
0.9
1

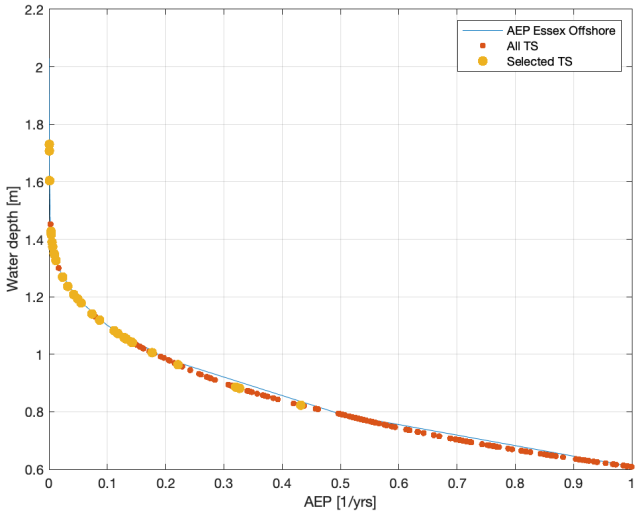
AEP Essex Offshore
All TS
Selected TS
Water depth [m]
AEP [1/yrs]
2.2
2
1.8
1.6
1.4
1.2
1
0.8
0.6
0
0.1
0.2
0.3
0.4
0.5
0.6
0.7
0.8
0.9
1

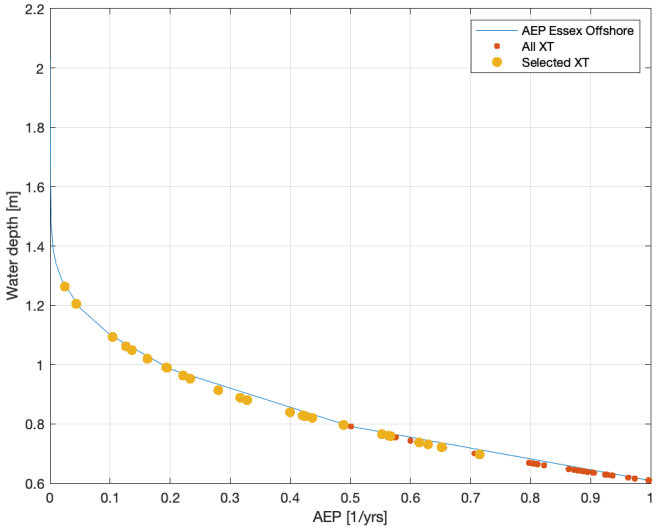
AEP Essex Offshore
All XT
Selected XT
Water depth [m]
AEP [1/yrs]
2.2
2
1.8
1.6
1.4
1.2
1
0.8
0.6
0
0.1
0.2
0.3
0.4
0.5
0.6
0.7
0.8
0.9
1

**Figure 36**. Annual Exceedance Water level curve for offshore of Essex Bay and the selected storm chosen to represent the highest return periods and the curve.

These storms were then modeling at high resolution with in Essex bay to assess the AEP flooding. Data were extracted from the model for specific sites (Table 1) and examined to determine water depths and flooding for set return periods. In addition system wide flood maps were created. Further, these storms were run in conjunction with sea level rise scenarios to determine the impact of SLR on the flood return periods. Lastly

### *6. Scenarios*

To assess the vulnerability of Essex town area from storm surge and waves, we simulated several selected storms (see storm characterization and analysis section) using our coupled flow and wave model based on Delft3D modeling suite. The primary storms influencing Essex town area are normally northeasters, but there are less frequent southwesterly extra-tropical cyclones as well as the infrequent hurricanes. The storms were selected, with corresponding wave height, wave period, wave direction, wind speed, and wind direction, which represent typical events with high, medium and low return intervals. The selected storms were then used in the final simulations for present conditions, and for future conditions under scenarios of sea level rise identified in the proposal (e.g., Kopp et al., 2017). Three simulations were performed to represent present conditions,

## VII. RESULTS

### A. Grain Size Data

The grain size and mineralogic analyses from more than 400 samples provide a means of evaluating net transport directions, wind processes, and depositional sites. The results of these analyses are given in Figures 36 to 44. Figures 36-38 encompass the entire beach system, tidal inlet, and Essex Bay area, whereas Figures 39-44 are concerned strictly with Crane Beach south of the mid-barrier protuberance. It should be noted that data were collected along the active portion of the beach affected by waves, including storm waves, but not in the dune system, which is dominated by wind processes.

### *1. Overall Grain Size Trends*

Sediment transport along Crane Beach is complex because unlike an open-coast beach where wave approach, particularly during storms, dictates the net direction movement of sand in the longshore transport system, this beach is affected by many processes:

1. Partial sheltering by the spit platform extending south from Plum Island, which reduces wave energy.
2. Strong tidal currents moving into and exiting Plum Island Sound along the northwestern half of the beach.

3. Plum Island Sound ebb-tidal delta, which affects the shoaling and breaking of waves along much of the landward shoreline.
4. Inlet sediment bypassing regime (discussed in later section).

Grain size data for the spit platform, ebb-tidal delta, inlet channel, and Essex Bay are provided in Figures 36-38 and Appendix 2. The grain size data along the length of Crane Beach indicate a general divergence in the longshore transport direction with a nodal point centered at the mid-island beach protuberance The data show a general trend of the coarsest sand (medium sand) at the beach protuberance and a fining in grain size toward Ipswich Inlet and to the southeast toward the spit. This is consistent with the fact that sand moves onshore from the ebb-tidal delta in the form of landward migrating bars. This sediment is sourced from sand transported seaward in the main ebb channel and then moved onshore by flood-tidal currents and by landward flow produced by shoaling and breaking waves. Ultimately, the sand comprising the landward migrating bars comes from Plum Island and enters the inlet by the dominant southerly longshore transport system in concert with flood-tidal currents.

Grain size trends characterized by a medium sand at the beach protuberance fining to a medium-fine sand along beach to the northwest, suggests northwestward transport toward Ipswich Inlet. Sand movement along the beach toward the Ipswich Inlet occurs during higher water elevations coincident with rising tides. Waves propagating onshore during higher tidal frames undergo less refraction and break at steeper angles to the beach. During these periods, waves approaching from the easterly quadrant produce a westerly nearshore longshore current that aids transport sand toward the inlet, especially during flooding currents entering the Sound.

The shore southeast of the beach protuberance experiences sand transport toward Essex River Inlet. Normally diverging sand transport regimes are areas of intense beach erosion because sand is not being replenished. However, at Crane Beach the protuberance is a region where bars migrate onshore from the ebb tidal delta that build up the beach, hence the cuspate shoreline shape.

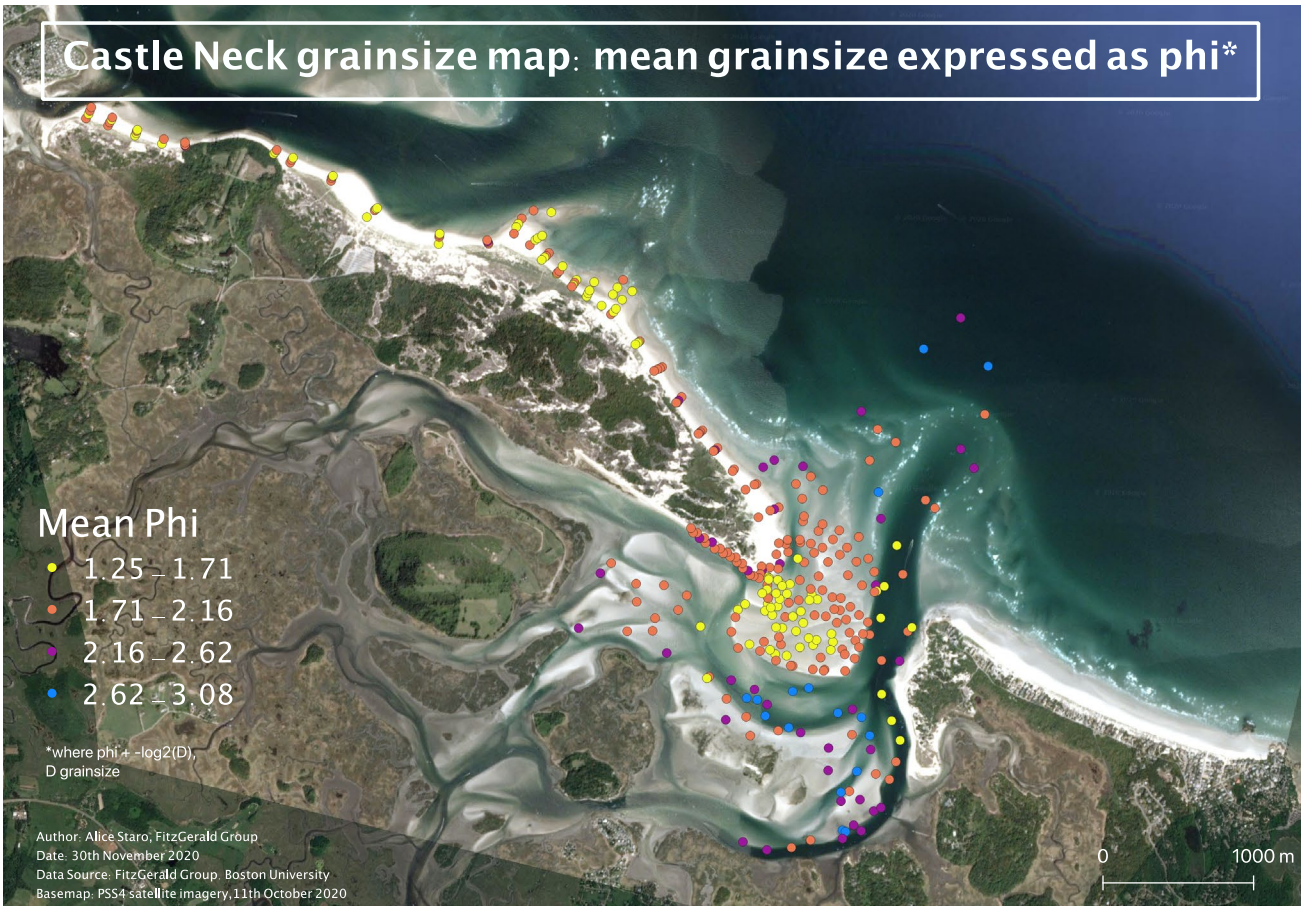


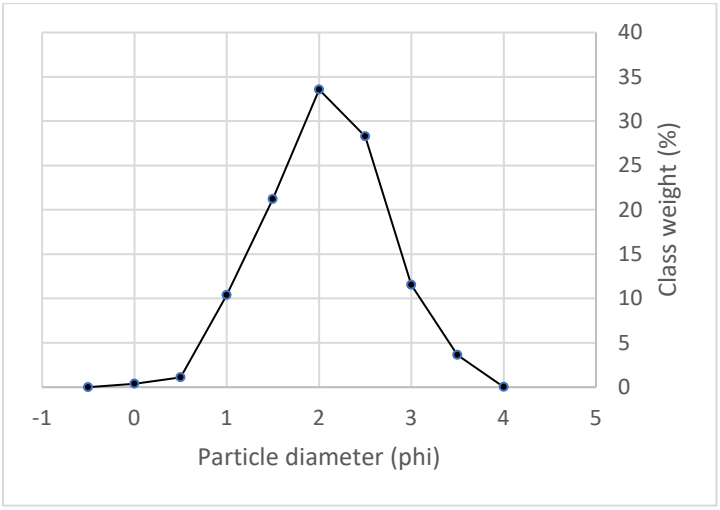


**Figure 37.** Mean grain size distribution in the project area. Note that majority of the sediment consists of medium to medium-fine sand. Interestingly, fine sand dominates the backbarrier channels and tidal flats. One major exception is the sand comprising western flood-tidal delta system immediately east of Choate Island, which is dominated by fine sand.

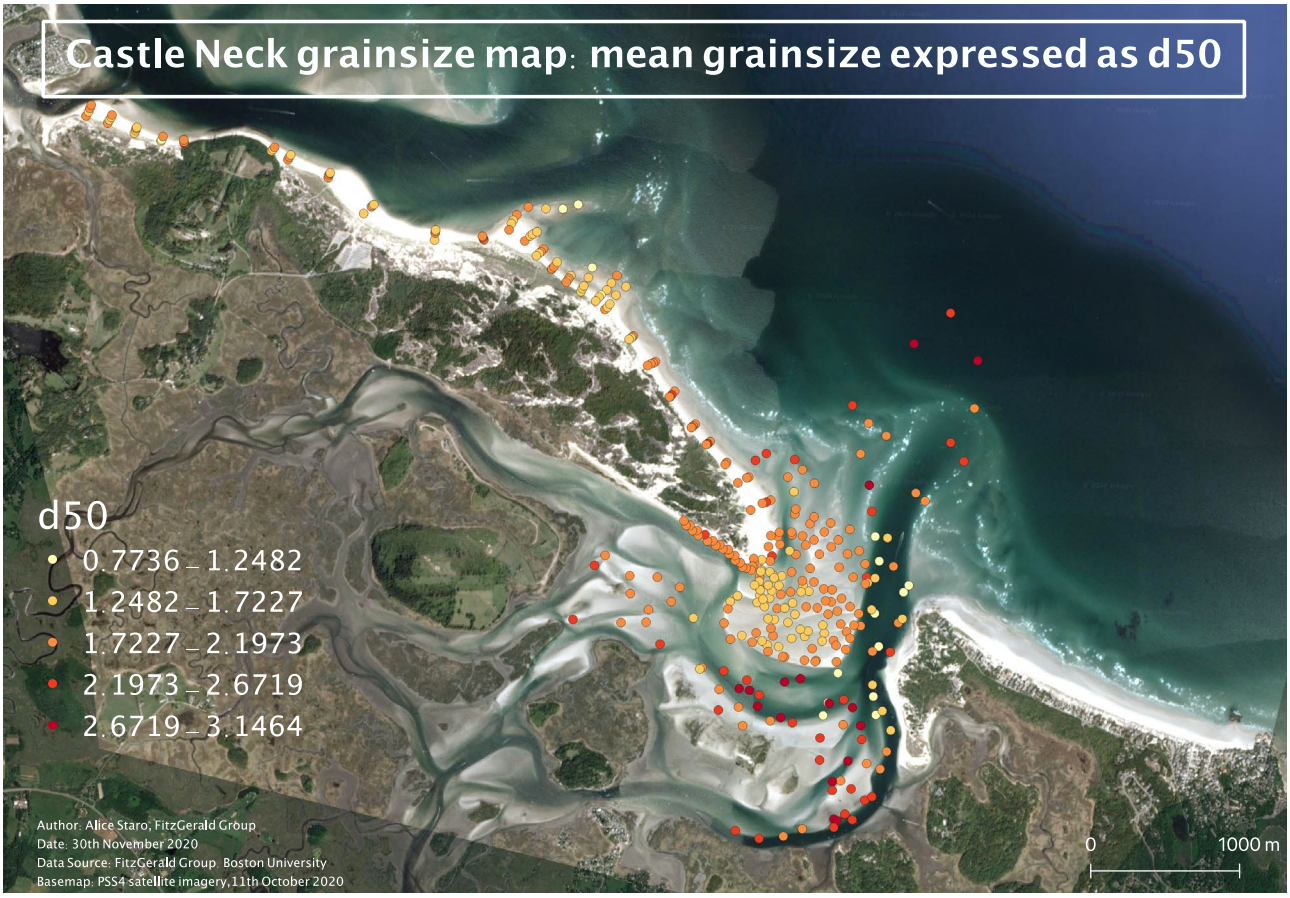


**Figure 38.** Median grain size expressed as D-50 in which half the population is larger and half the grain size is smaller. Note that downdrift (southeast direction) of the beach protuberance, generally the sand fines into the tidal channels. There is also a slight fining trend along the beach toward Ipswich River Inlet.

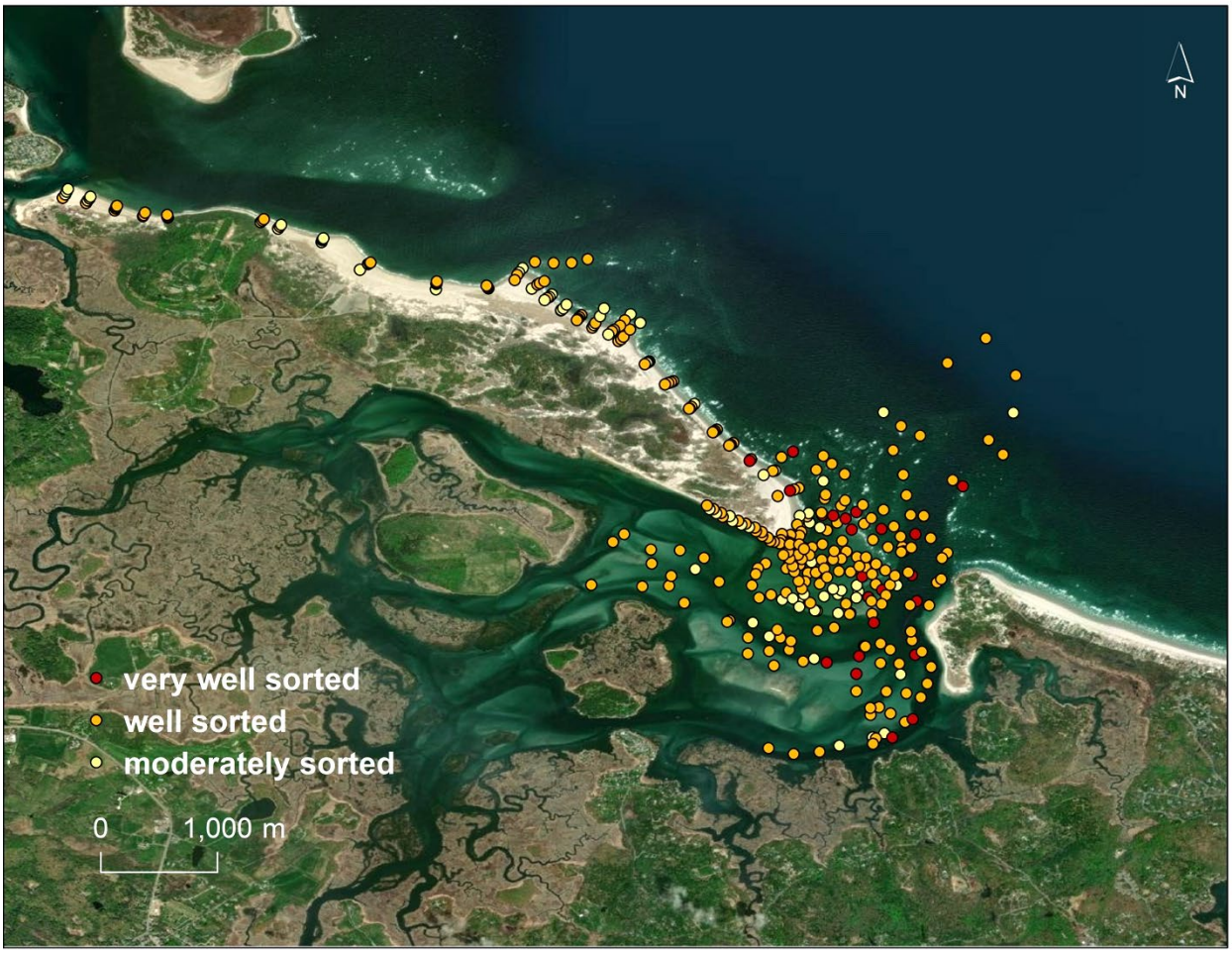


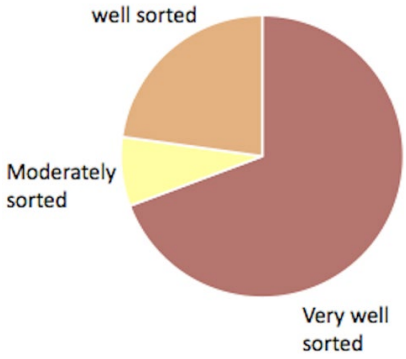


**Figure 39.** Mean grain sorting (Standard Deviation) of the sand population. Most of the sand is very well sorted, indicating that it is mature having been reworked onshore or alongshore over a considerable long distance.

Figures 36, 37, and 38 show a general trend of decreasing grain size and increased sorting toward Essex Inlet indicating a southerly longshore transport direction, which is consistent with periodic spit extension at the southern end of Castle Neck. Geophysical evidence also supports

a net southerly movement of sand along Crane Beach. Ground-penetrating radar was used to image the subsurface. This instrument produces and X-ray view of the layers of sand comprising the barrier with the ability to see about 8 m below the sand surface. A transect at the end of the island exhibits a distinct set of southeasterly dipping reflectors extending to a depth of about 5-6 m. These reflectors represent accretionary surfaces that were formed by the sloping beachface and nearshore environment. The parallel dipping reflectors indicate that the spit builds in pulses between periods of quiescence. This scenario describes well what occurs during a storm when wave energy substantially increases the longshore transport rate and sand contribution to the end of the island.

### *2. South (Spit) end of the Island*

A more detailed characterization of the sediment provenance at the spit end is provided in Figures 39-44, which includes both grain size and mineralogical analyses. Results of the 32 samples collected along southern Crane Beach are presented as individual mean grain sizes for the upper berm, berm crest, beachface, and lowtide terrace (Figure 39) as well as averages for each of these environments and averages of the samples collected along each of the eight transects (Figure 40). As Figures 39 and 40 demonstrates, there is considerable heterogeneity along beach, with an overall trend of decreasing grain size to the south. Looking at the individual sectors along the beach, the finest sand is found on the beachface and the coarsest sand occurs along the berm crest. Wave swash and backwash transport the coarser grains onshore and offshore, whereas onshore winds winnow the fine sand, slightly coarsening the berm crest, while at the same time adding fine sand to the upper berm.

Grain size sorting of southern Crane Beach is shown in Figures 41. It is seen that the beach spanning the northern four transects consists mostly of well-sorted to moderately well-sorted compared to the southern four transects that contain mostly well-sorted to very well-sorted sand. This is to be expected as sand typically becomes better sorted with distance of travel. Individual frequency curves for the different environmental settings show similar overall average grain size, but the upper berm shows the least degree of variability. This is because the upper berm consists of sand that has undergone the greatest degree of reworking and finest grain sizes (Figure 42) compared to the other environments.

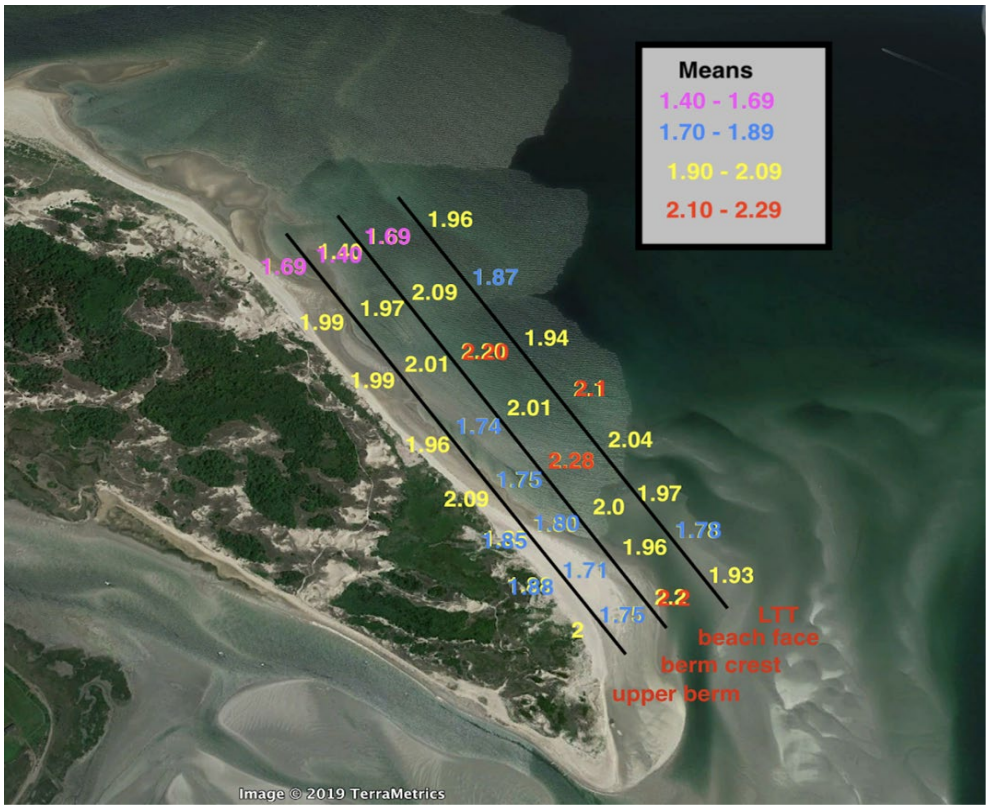


**Figure 40**. Grain sizes at different elevations across the beach and along the beach. Although there is considerable variability, generally grain size decreases toward the southern end of the spit


**Figure 41.** Averages for mean grain size along the beach and average grains sizes along a transect vertical to the beach. Note that grain size generally decreases to the south, whereas the averages vertical grain sizes trends is mixed.

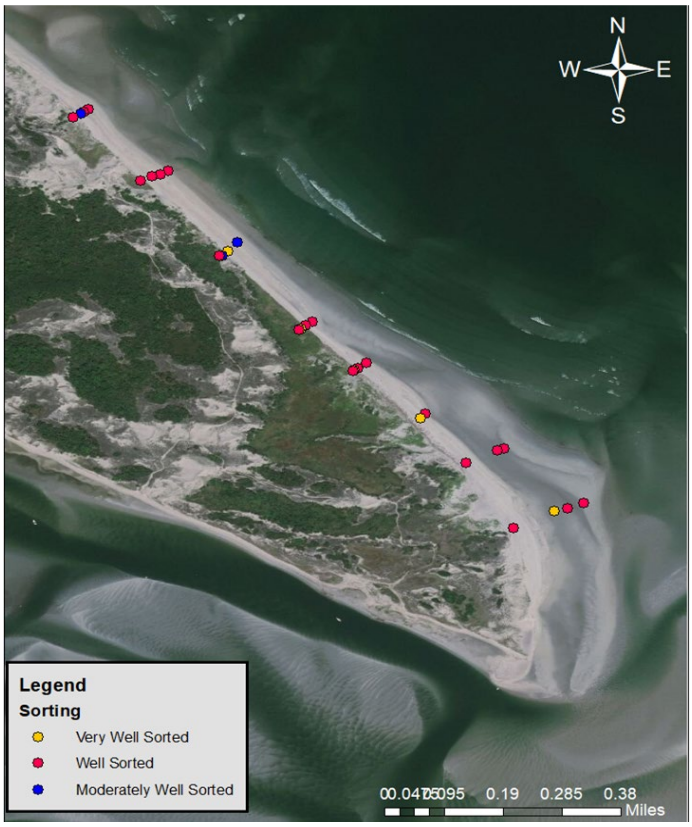


**Figure 42.** Grain sorting along the beach. Generally, the sorting improves toward the southern spit end of the beach

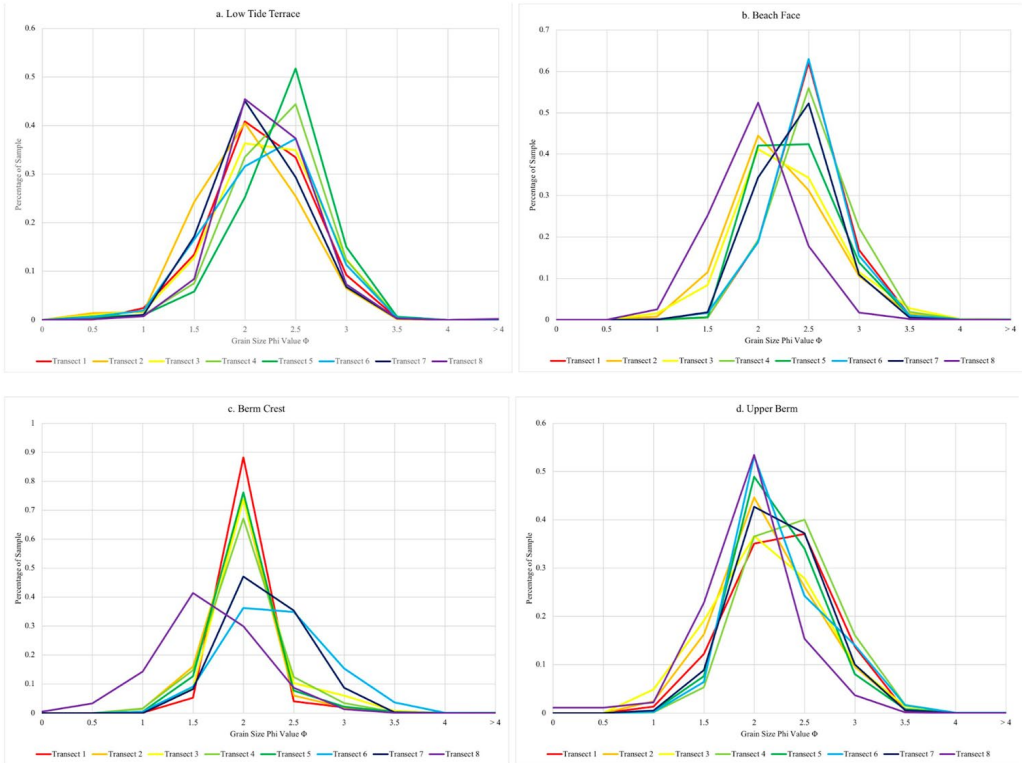


**Figure 43**. Grain size frequency curves for different positions along the beach. Berm crest tends to be coarsest.

Results of the mineralogical analyses of the same sites discussed above are shown in Figure 43. The major mineral grains consist of quartz, feldspar, and rock fragments. All other grains were grouped together as others. Rock fragments are grains that consist of more than one mineral or essentially a grain that has not been broken down to individual minerals. The greater the number of rock fragments in the sample, the more immature is the sand and conversely, the higher the percentage of quartz the more mature is the sand. All of Crane Beach contains highly mature quartzose sand. However, as seen in Figure 43, the feldspar content decreases to the south while at the same time, the quarts percentage increases, indicating dominant transport to the south. Exceptions to these general trends occurs where the wind has winnowed the finer less dense quart and feldspar grains concentrating the garnet and iron-oxide minerals (Figure 44).

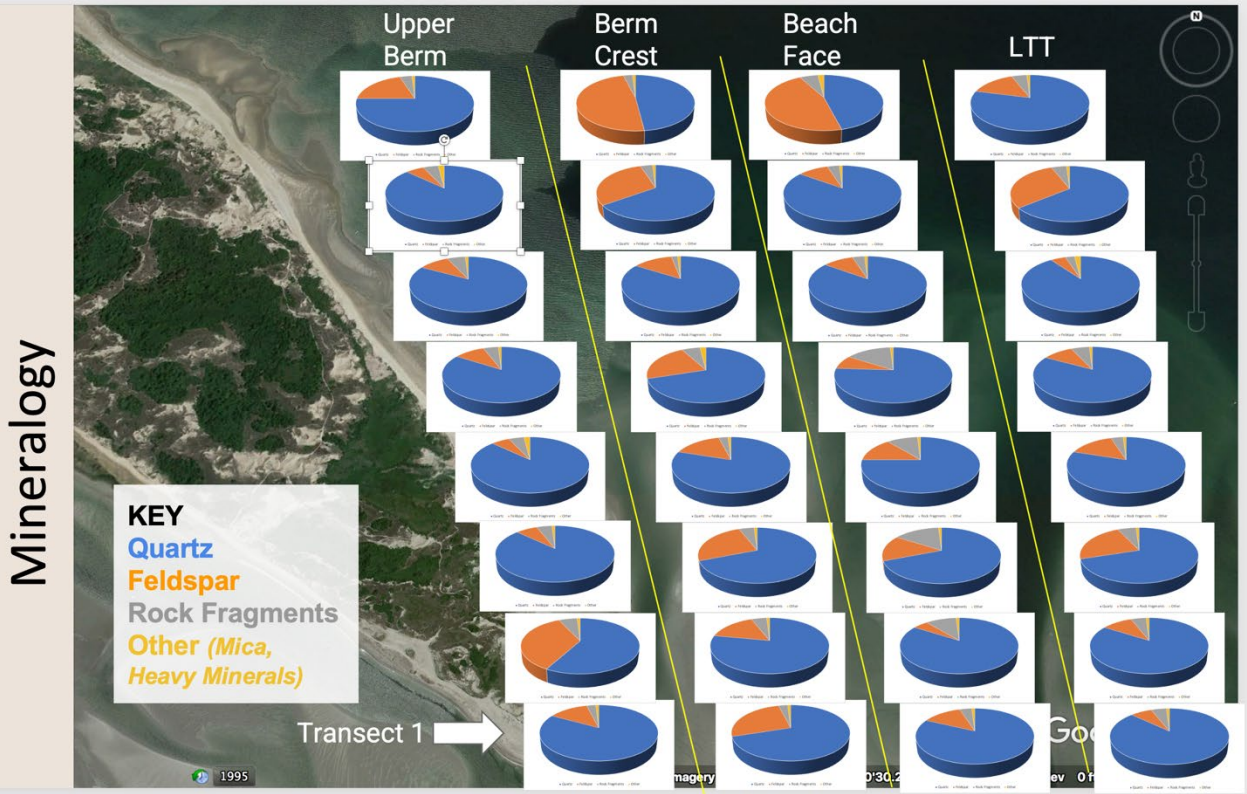


**Figure 44.** Mineralogical analyses of beach sand along southern Crane Beach. Note the general slight trend of increasing quartz content both toward the nearshore and south along the beach.

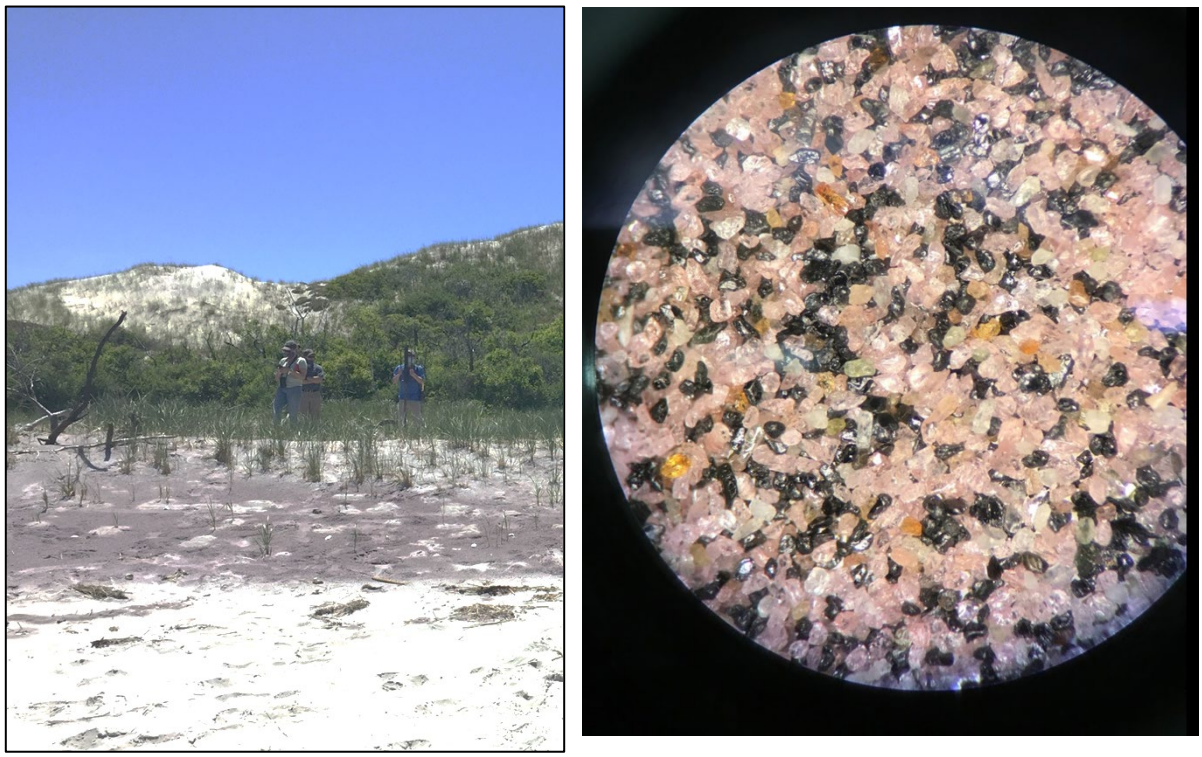

Figure 45. Garnet sandis clearly visible in the upper berm along southern Crane Beach **(left panel)**. This concentration is a product the wind winnowing away the lighter quartz grains leaving behind the heavier garnet and iron oxides. **(right panel)** Photo-micrograph of beach sample taken from upper berm in left panel. The black grains are magnetite and ilmenite and the pink grains are garnet.

## B. Historical Morphological Changes

### *1. General Trends*

During the period of record (1938-2020) the Castle Neck barrier has had a complex morphological history, involving primarily its shoreline. The barrier is 0.4 to 1.0 km wide and 5.5 km long and is anchored to the amalgamated drumlin complex of Castle Hill and Steep Hill, which comprises the Crane Estate (Figure 45). These drumlins separate the Steep Hill Beach to the west and Crane Beach to the southeast (for this report the entire beach is referred to as Crane Beach). As seen in Figures 45 and 46, the barrier exhibits a range of elevations spanning areas that are only a couple of meters above mean high water to Wigwam Hill that is almost 25 m high. Although sand blankets this portion of Castle Neck (see dark red area of Figure 46), it is actually a dune-covered drumlin. Other major dunes occur along its length, but they are much lower. Note that the overall elevation of the barrier decreases to the southeast, which coincides with the age of the barrier, younging to the southeast. The general trends in width and elevation of the barrier provide clues to the evolution of Castle Neck. The relatively wide and high topography in mid-Castle Neck suggests that sand moving onshore as landward migrating sheets and transgressive

segmented barriers stabilized at Wigwam Hill drumlin and barrier prograded seaward and southward as sand was added from both along and offshore sources.

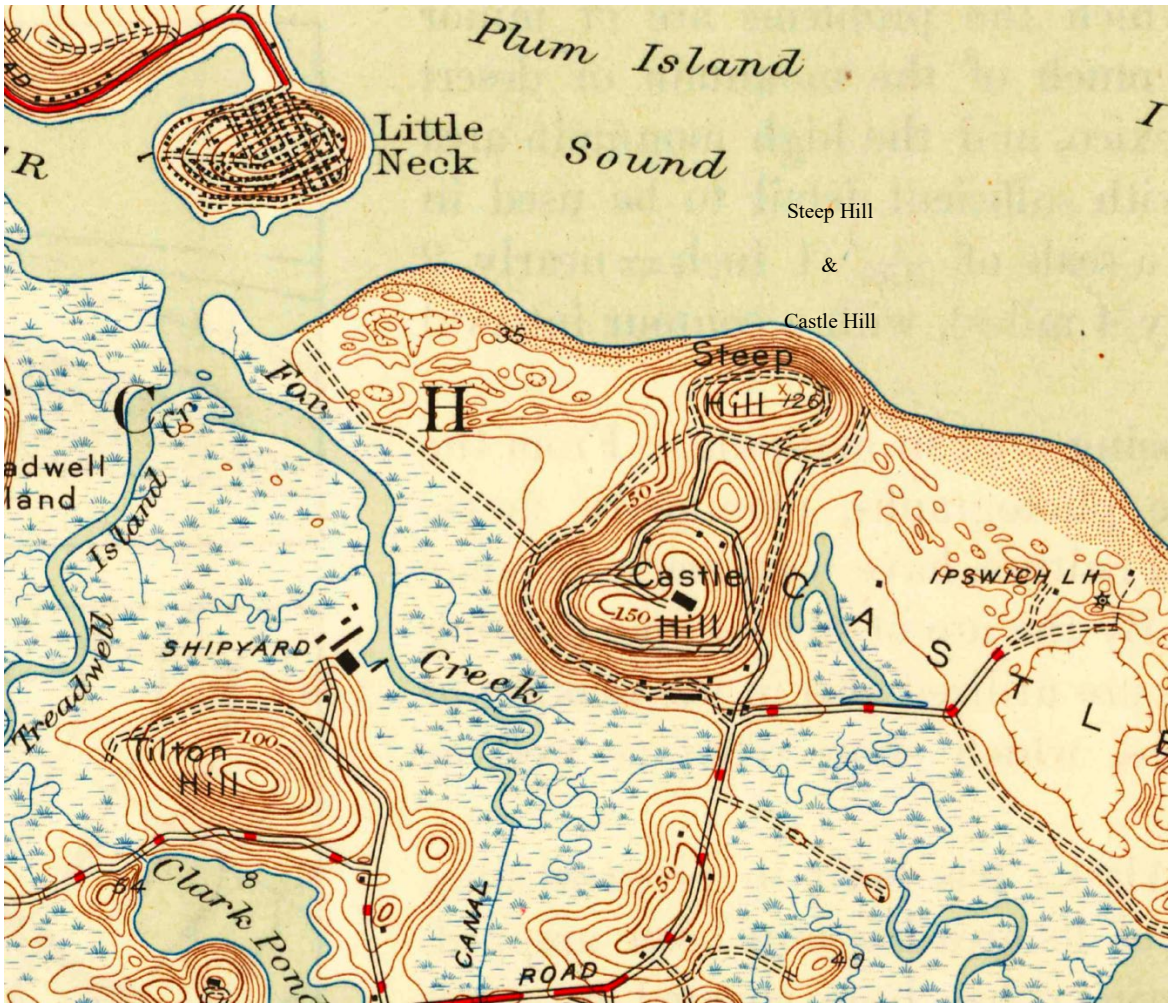


Figure 46. Topographic map of the Ipswich coast. The rounded high elevation features are drumlins.

The constant changing nature of the Castle Neck barrier and Essex Inlet and Bay system is illustrated in Figures 47 and 48. The images in Figure 46 were taken at low tide within 8 cm of the same elevation so that the difference map in Figure 47 is 97% accurate. A dominant trait observed from this analysis is that except for the island interior that is largely protected and vegetated and therefore stable, most the periphery of the island undergoes change. There is an outline of yellow along the seaward side of the barrier representing the beach, but most of the other barrier environments experience change. And even the beach undergoes topographic changes due to storms and wind processes. The most dramatic changes are the conversion from water to sand and sand to water shown by the brown and dark blue colors, respectively (Figure 48).

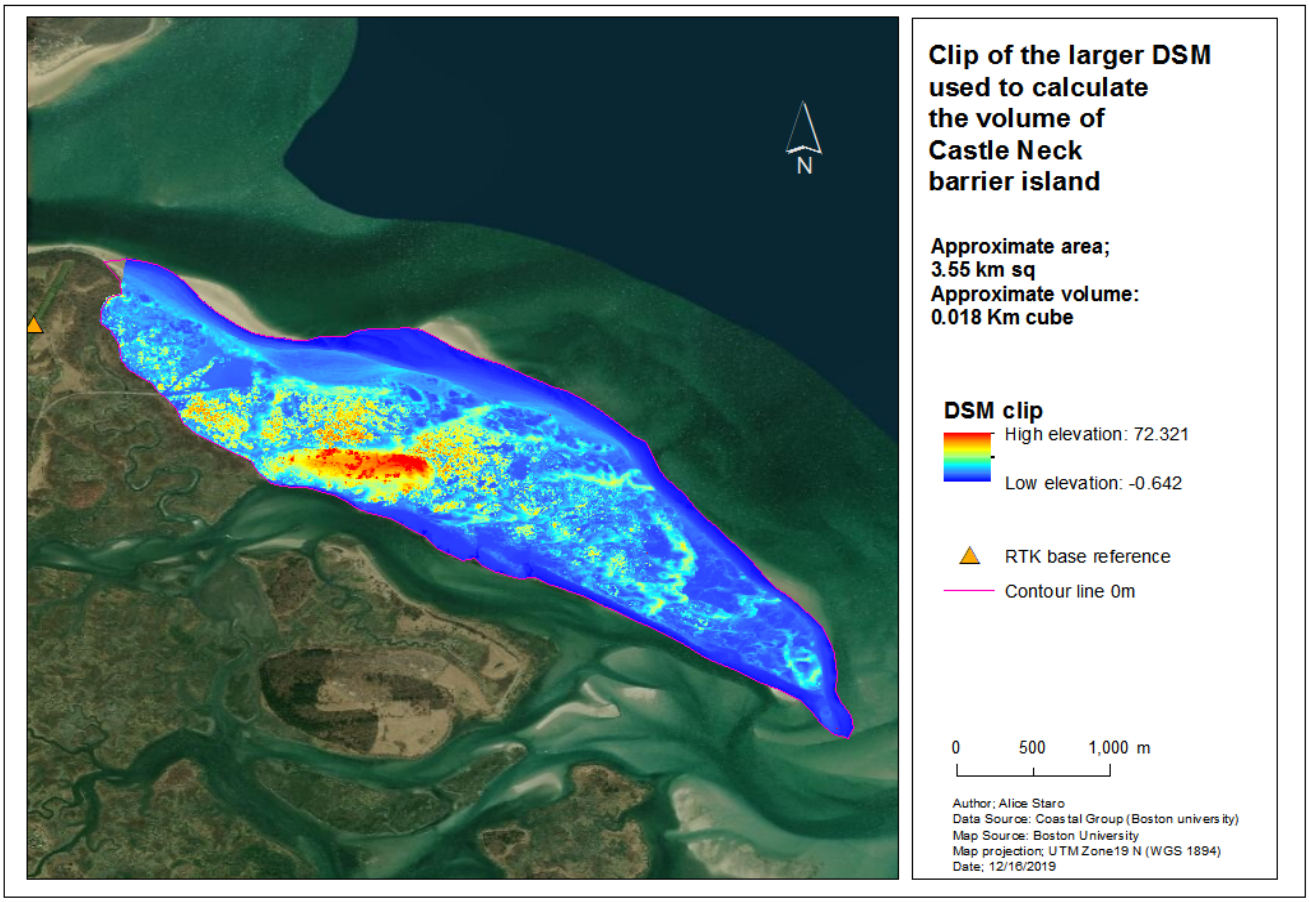


**Figure 47.** Digital Surface Model of Castle Neck east of the drumlins.. Note the height of Wigwam Hill shown by the dark red color which is almost 25 m high.

### 2. *Detailed Beach Morphology and Processes*

To discuss the major processes and morphological changes, the barrier is separated into four major regions including: **a.** ***Cedar Point and Steep Hill Beach*** comprising the beach west of the Castle Hill-Steep Hill drumlin complex, **b.** ***North Crane Beach*** encompassing the beach east of drumlin to **c.** ***Beach Protuberance*** at mid-island, and **d.** ***Southern Spit*** extending to Essex River Inlet (Figure 49).

***a. Cedar Point-Steep Hill Beach.-*** This region is semi-protected by Plum Island and its southern spit platform that extends into Plum Island Sound. However, strong storm waves that shoal and reform after crossing the spit platform and those that refract through the inlet channel can buffet the beach. Due their approach angle from the easterly quadrant, sand along the shore is transported to the west, especially augmented during flooding tides. This process contributes sand to Cedar Point impinging Fox Creek and to Steep Hill Beach. As seen in the oblique aerial photograph in Figure 50, a system of older, partly deflate dunes is fronted by a 100-m wide prograding beach ridge system.

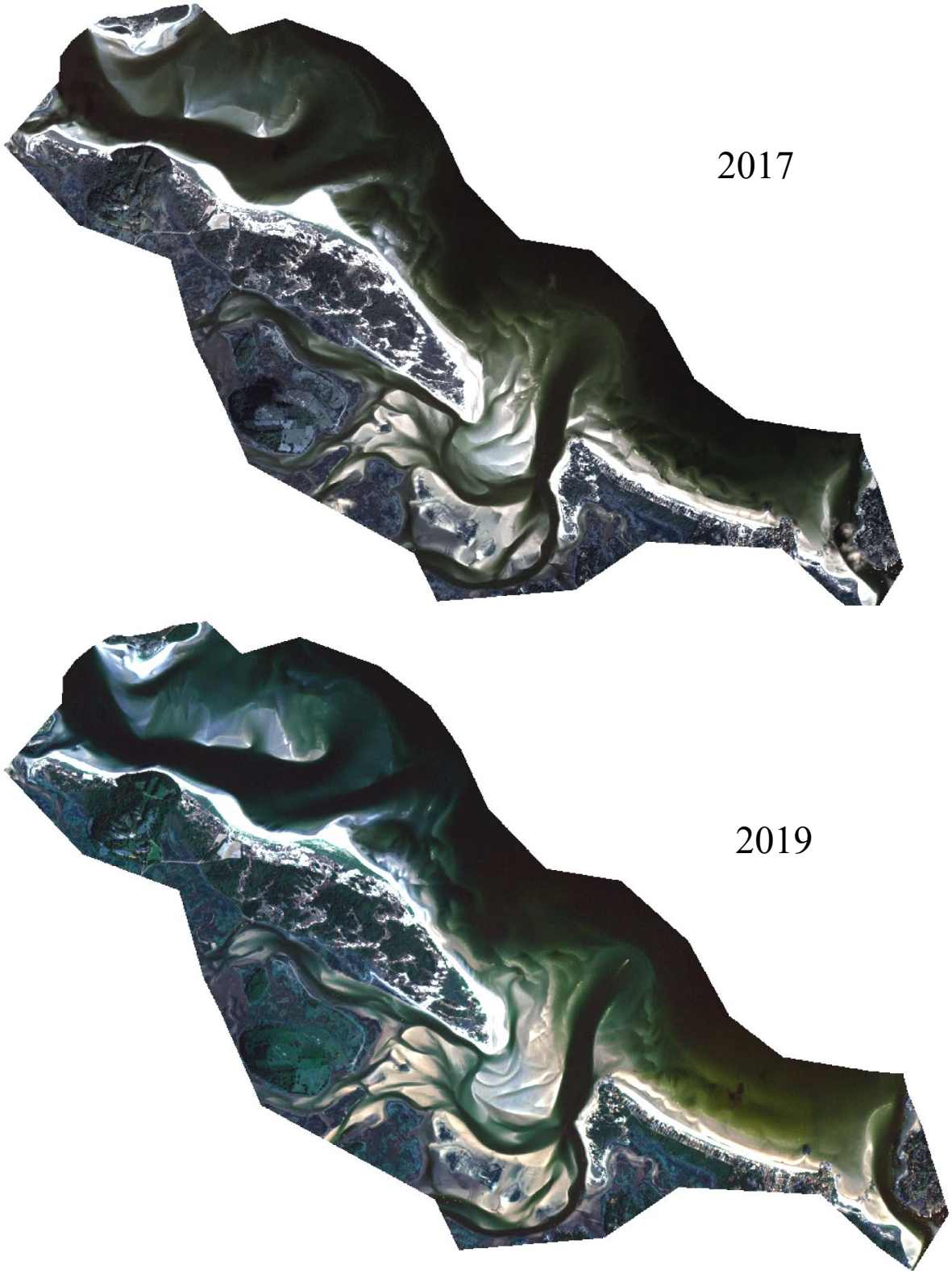


**Figure 48.** 2017 and 2019 images of Castle Neck barrier and Essex River Inlet complex. These images were taken at similar tidal elevations (8 cm difference).

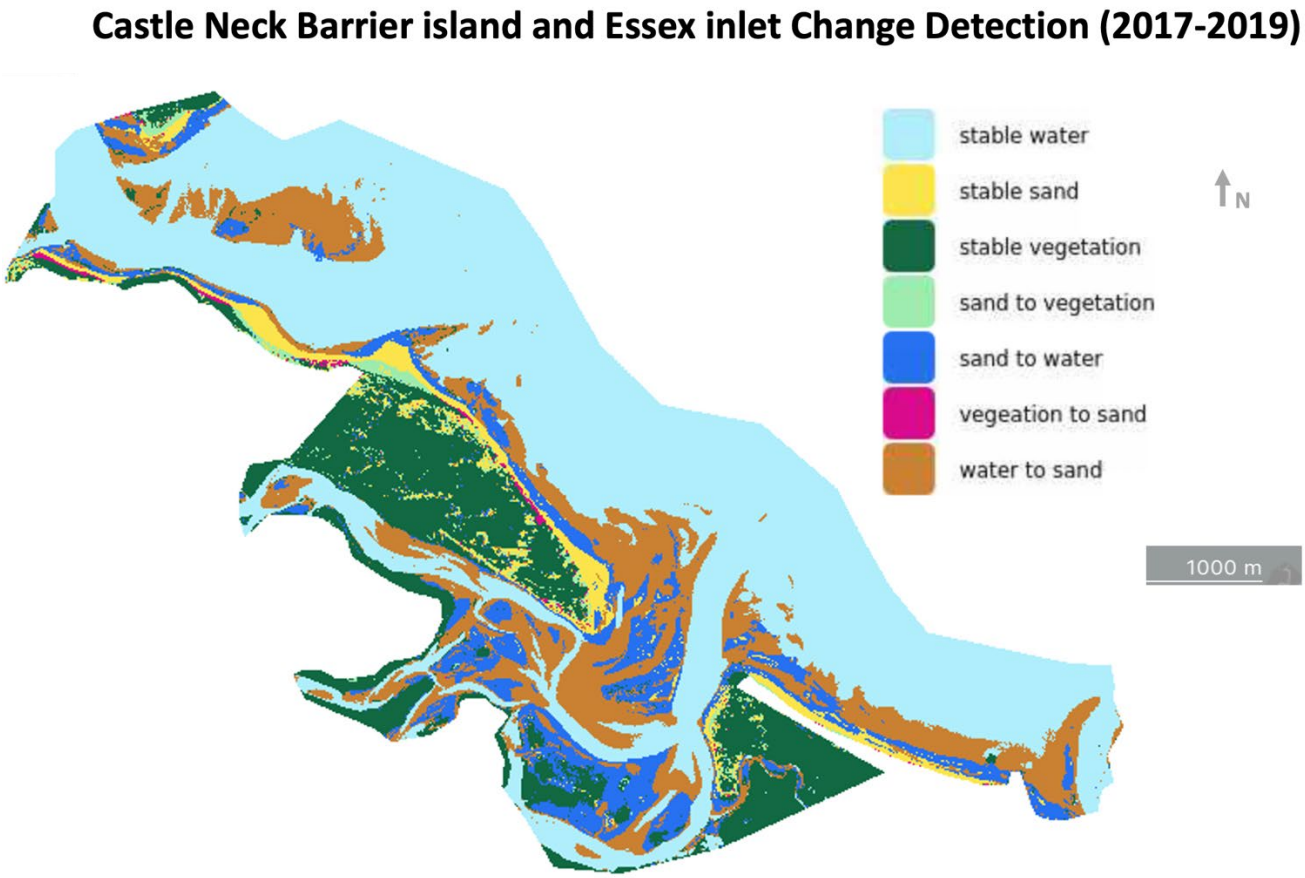


**Figure 49** Geomorphic map of Castle Neck and Essex Inlet systemshowing how surface area changed in elevation in terms of coastal environments from 2017 to 2019 (based on images shown in Figure 46.)


**Figure 50**. Morphological units discussed in the text.


**Figure 51.** Oblique aerial photograph looking north across Steep Hill Beach and Ipswich Beach.

However, this beach can experience periods of erosion and retreat, especially during intense storms, such as those that occurred during the winter of 2018. The Bomb Cyclone (2 January 2018) and Blizzard of 2 March 2018 coinciding with perigean spring high tides produced large storm surges and allowed high energy waves to break along the upper beach, resulting in 20 m of retreat. During the following two years, the beach completely rebuilt. Because of the continual sand supply, this region is considered fairly stable.

***b. North Crane Beach.-*** Although it would seem that this mid-section of the barrier would be fairly stable, particularly located between two slight promontories: Steep Hill to the northwest and the beach protuberance to the southeast, this section of the barrier is actually everchanging (Figure 51). The beach here undergoes shoreline shifts of 50 to more than 400 m during decadal to centennial timeframes, which cannot be explained by simple long-term trends or a single storm. Rather, in addition to storm erosion, there is also the meandering of the main ebb channel (Figures 52 and 53) that periodically migrates close to the shore along this section of barrier causing shoreline retreat. Likewise, when the channel migrates away.

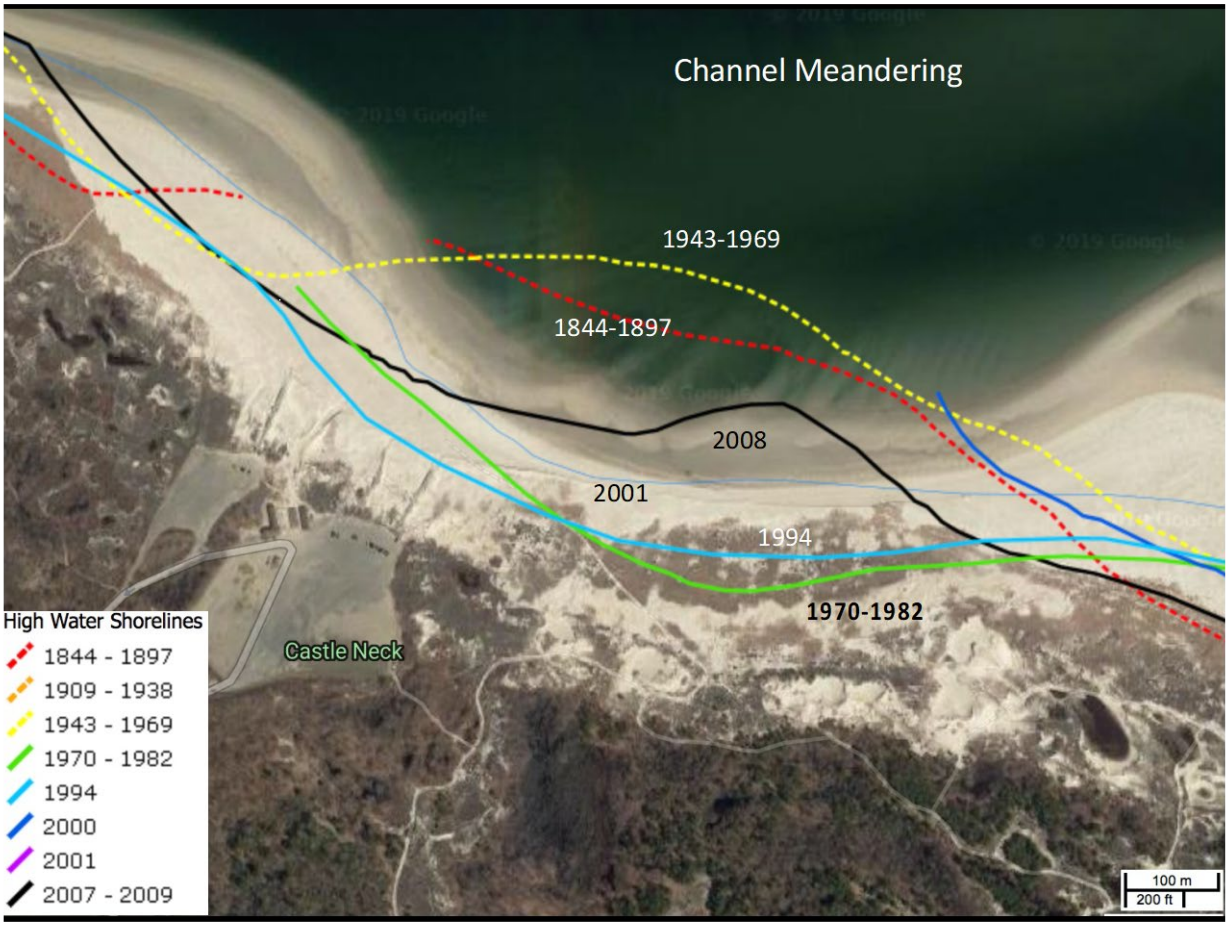


**Figure 52.** Shoreline changes for the 1844 to 2009 period (from CZM Shoreline Mapper). Note that region of the barrier has undergone dramatic changes amounting in some regions to more than 400 m of shoreline retreat and advancement.

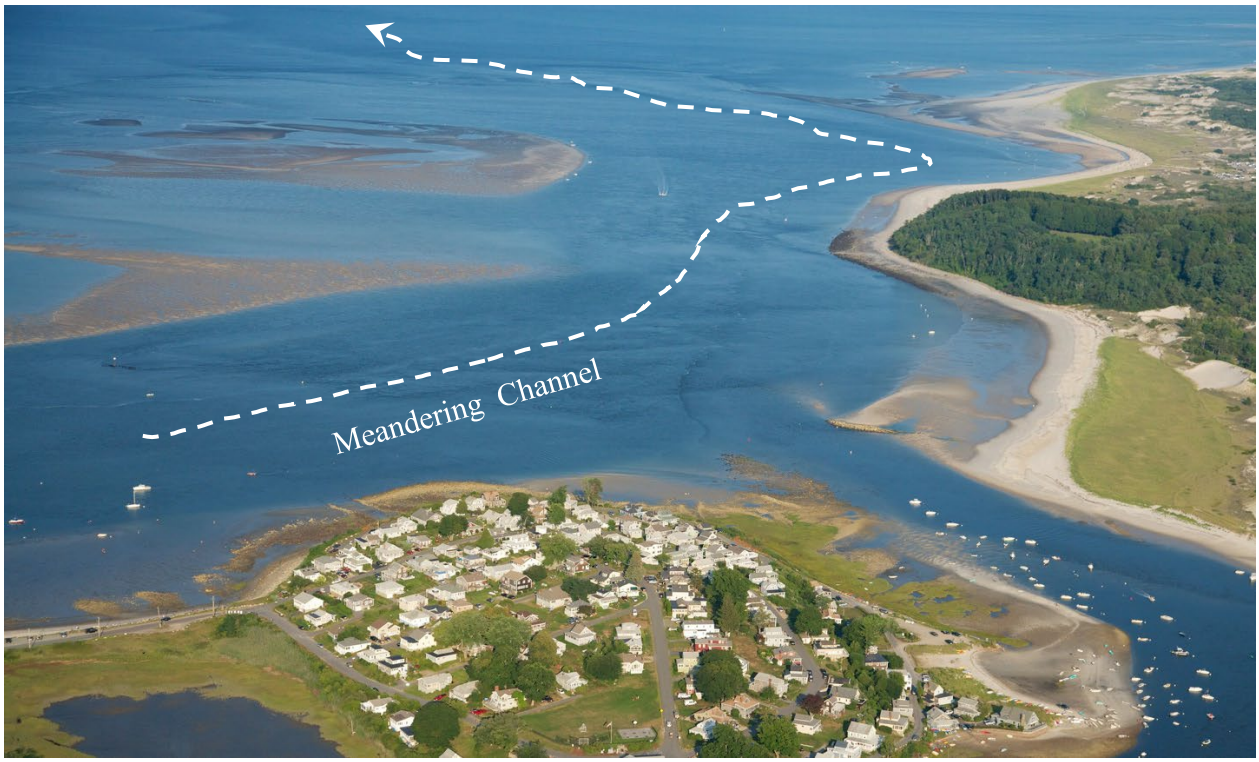


**Figure 53.** Meandering of main channelcan result in ebb flow impinging against North Crane Beach.

**Figure 54** Channel in a position distant from the beach allowing the beach to accrete.

from the shore the beach progrades. One period of prolonged channel impingement against North Crane Beach occurred during the 1970's when the beach retreated approximately 400 m in less than 10 years (Figure 51). Erosion of this section of the beach exposed the large foredunes that backed this beach to the full impact of the Blizzard of 1978, the storm of record for this region. As seen in Figure 54 (panel A), the dune scarp produced by this storm was 2 to > 6 m in height. Following the storm, the beach covered and built seaward as shown in Figure 54 (panels B-D). While this section of the beach has experienced a long period of stability (> 30 years), historical shoreline data indicate that migrations of the main Plum Island Sound channel can cause rapid erosion.

***c. Beach Protuberance.-*** is a cuspate foreland east of North Crane Beach (Figure 49) that has formed and dominates the morphology of this part of the barrier (Figure 55). Sand that is transported southward along Plum Island enters Plum Island Sound Inlet due to wave energy and flood-tidal currents. Most of this sand eventually bypasses the inlet (process discussed later in the report) and comes ashore to Castle Neck in the form of large landward swash bars that weld to the shoreline and prograde the beach (Figure 55). In Figure 55, it can also be observed that sandwaves migrate an easterly direction along the nearshore toward the protuberance. This

movement of sand is caused by ebb-tidal currents in the main channel during the falling tide. This process also adds sand to the protuberance.

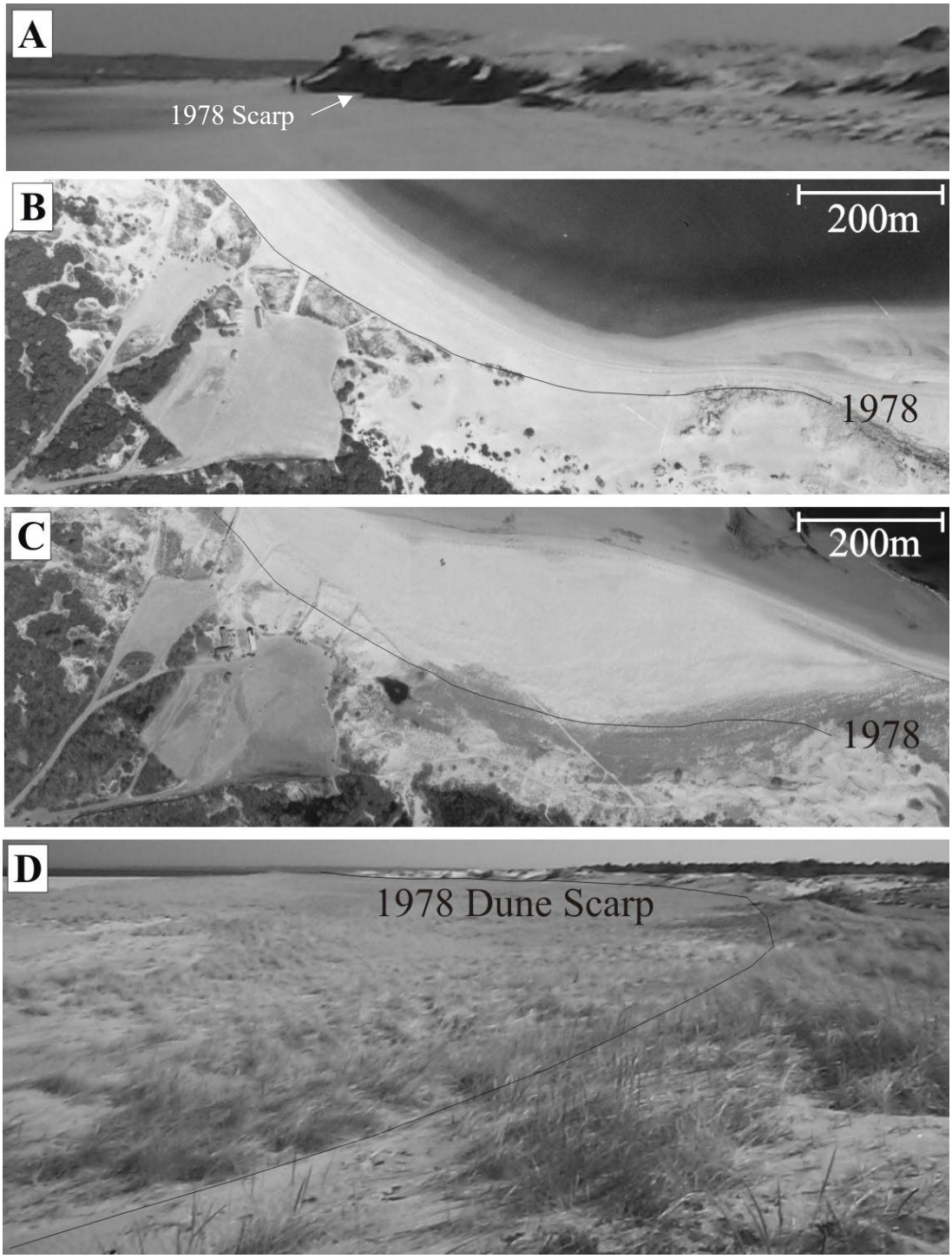


**Figure 55.** Views of the erosion caused by the Blizzard of 1978and subsequent reconstruction of the beach and vegetated dunes just south of the walkovers and parking lot (from Dougherty et al 2004).

Although this is an accretionary region due to the movement onshore of sand from the ebb-tidal delta, the historical shoreline changes depicted in Figure 56, indicates that beach here can undergo rapid erosional and depositional phases which is part of inlet sediment bypassing regime. The accretionary phase occurs when the bars are some distance offshore, resulting in shoaling and wave refraction that produce a sheltered area along the onshore beach. This process along with the addition of landward migrating swash bars cause beach progradation. However, once the protuberance is fully develop extending hundreds of meters offshore it becomes a promontory and the site of wave focusing and erosion. This is destructional phase, which is presently occurring (see Appendix 3).

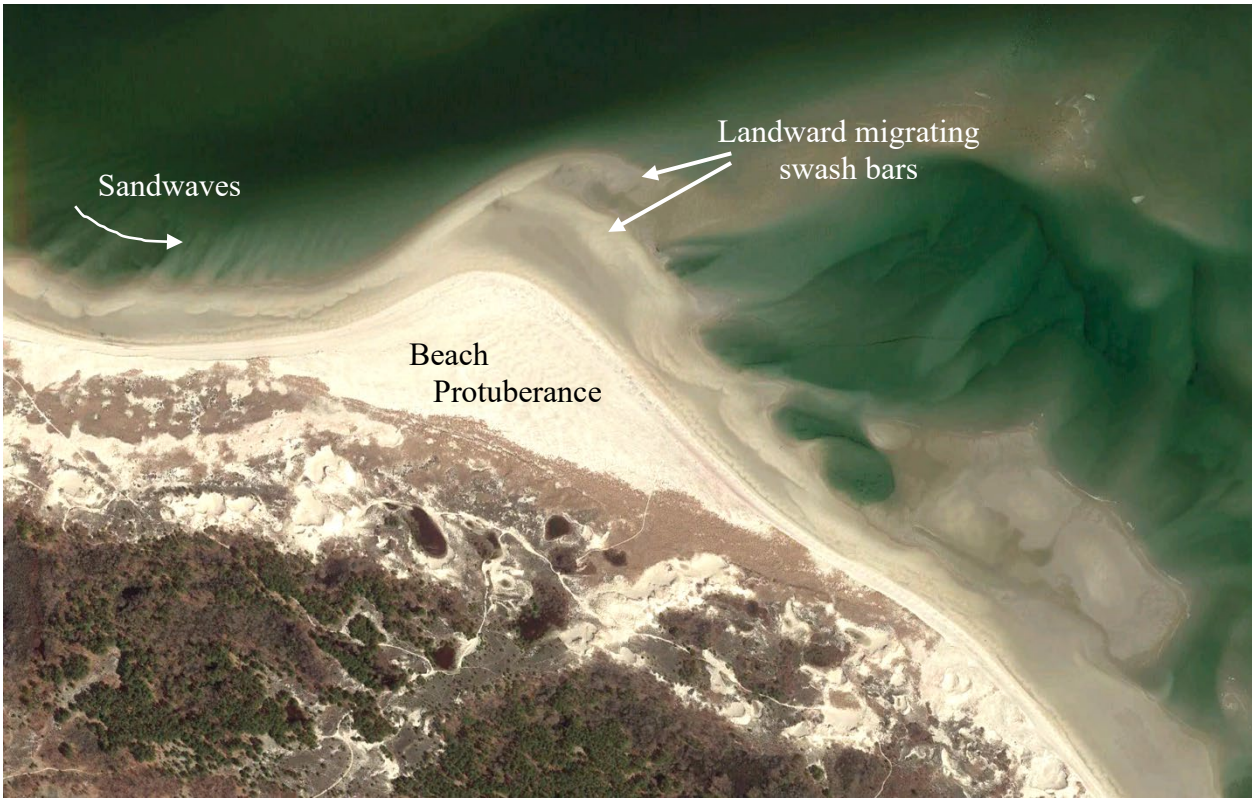


**Figure 56**. View of the Beach Protuberance along the mid-barrier.The bulge of the beach here is the result of the welding of landward migrating swash bars. Sandwaves migrate eastward due ebb flow.


**Figure 57** 2021 image of the Beach Protuberancewith historic highwater shorelines from CZM mapper. Note the 200 m of shoreline accretion between 2000 and 2021.

***d. Southern Spit-*** As described above, spit accretion was an important process in forming the southeast end during the evolution of Castle Neck (Figure 49). However, due to its proximity to Essex Inlet, the spit is constantly subjected to strong tidal currents and wave focusing during storms. Both of these processes can cause rapid erosion and shoreline retreat. Its stability is largely related to the volume of sediment moving south through the longshore transport system, which replenishes sand lost during storms and high wave-energy events.

Figure 57 shows that the spit prograded from 1897 to 1969 followed by a period of erosion and spit retreat from 1969 to at least 2009. A more detailed account of the 2003 to 2019 period is provided in Figure 58, which chronicles a dramatic loss of sand from the barrier and retreat of the Southern Spit. A graph of shoreline retreat indicates that seaward side of spit retreated 250 m from 1995 to 2018 and the end of spit eroded back some 600 m during the same period (Figure 59). The erosion of Southern Spit is intimately related to the stage of beach protuberance evolution. During the constructional phase most of the sand is sequestered on the enlarging beach protuberance and much of the trapped sand is not released until the bar migrations cease and the cuspate foreland begins to erode. When the beach protuberance is building, the spit is sand- starved and erodes.


**Figure 58**. 2021 image of the Southern Spit systemwith historic highwater shorelines from CZM mapper covering the past ~ 150 years.

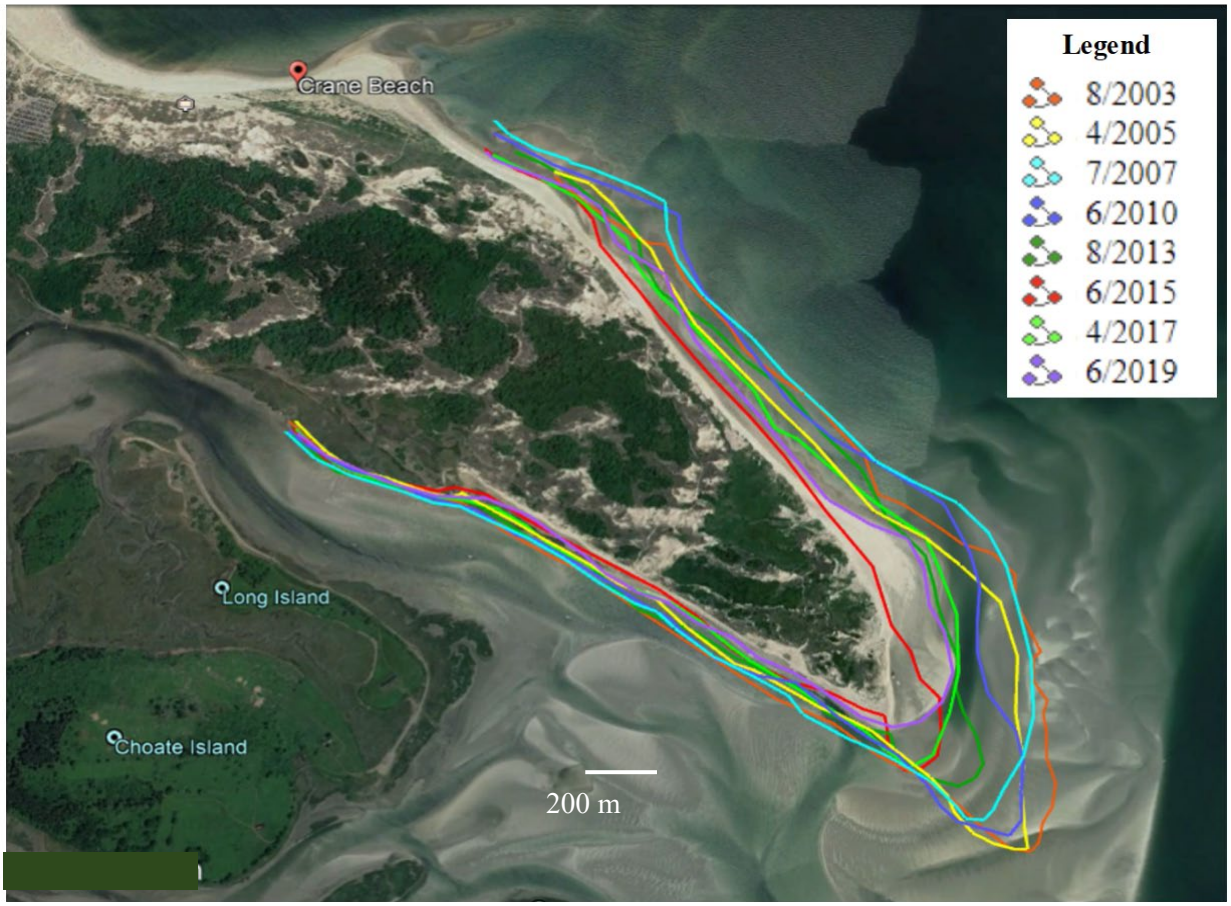


**Figure 59.** Historical shoreline changes determined from Google imagery of highwater shorelines. Note the dramatic erosion that took place from 2003 to 2019.

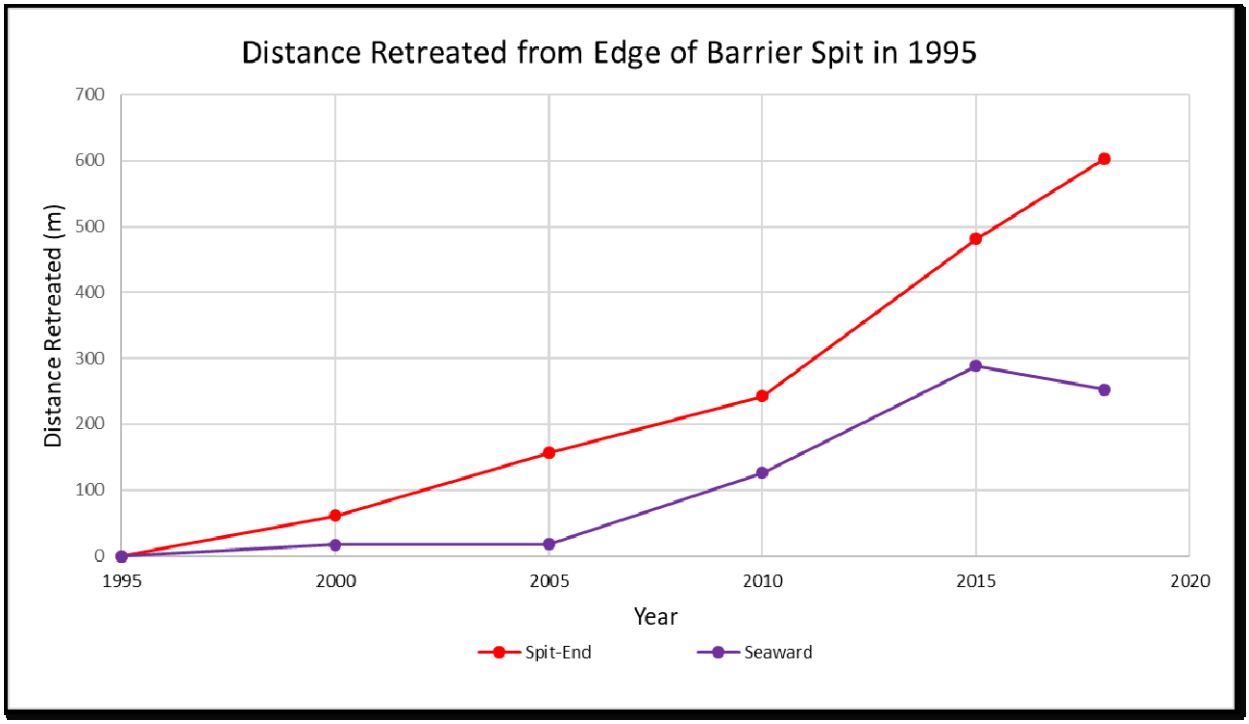


**Figure 60.** Shoreline history for the spit end from 1995 to 2018determined from Google imagery.

### C. Essex Bay Sedimentation Patterns

The sand eroded from the Southern Spit enters Essex Inlet and Essex Bay and is redistributed by tidal currents. Little if any of the sand is transported by waves to the backside of the spit, as this area is dominated by scarps and eroding beaches (Figure 58). Also, although sand is likely moved onshore and offshore in the main channel of Essex Inlet, little of this sand is deposited permanently on the ebb-tidal delta. There is no evidence of the ebb-tidal delta expanding during recent times, because it has reached and equilibrium size and volume as dictated by its tidal prism (Smith and FitzGerald, 1994). The disposition of the sand washed into Essex Bay is problematic because of the probable widespread dispersal of the sand. The volume of sand eroded from the spit was determined from image analyses and LIDAR data for three time periods (Table 7). These datasets only extend to 2011, but the spit actually began retreating in the mid-1990's. When the loss is extrapolated to 1995, a volume of 237,000 $m^3$ of sand is calculated as having been eroded from the Southern Spit. As Figure 60 demonstrates, the intertidal environments have undergone widespread changes, but most of these changes are related to intertidal shoals either becoming subtidal or vice versa. However, expansion of the spit platform into Essex Bay and growth of western flood delta might explain where some of the eroded sand was deposited (Figure 61). During the 10-year period from 2008 to 2018, the channel running behind Castle Neck (~ 2-3 m deep) filled with sand and slightly shifted northward eroding the barrier. This type of infilling, shoal formatting and shifting of channels was partly the result of the sand influx.

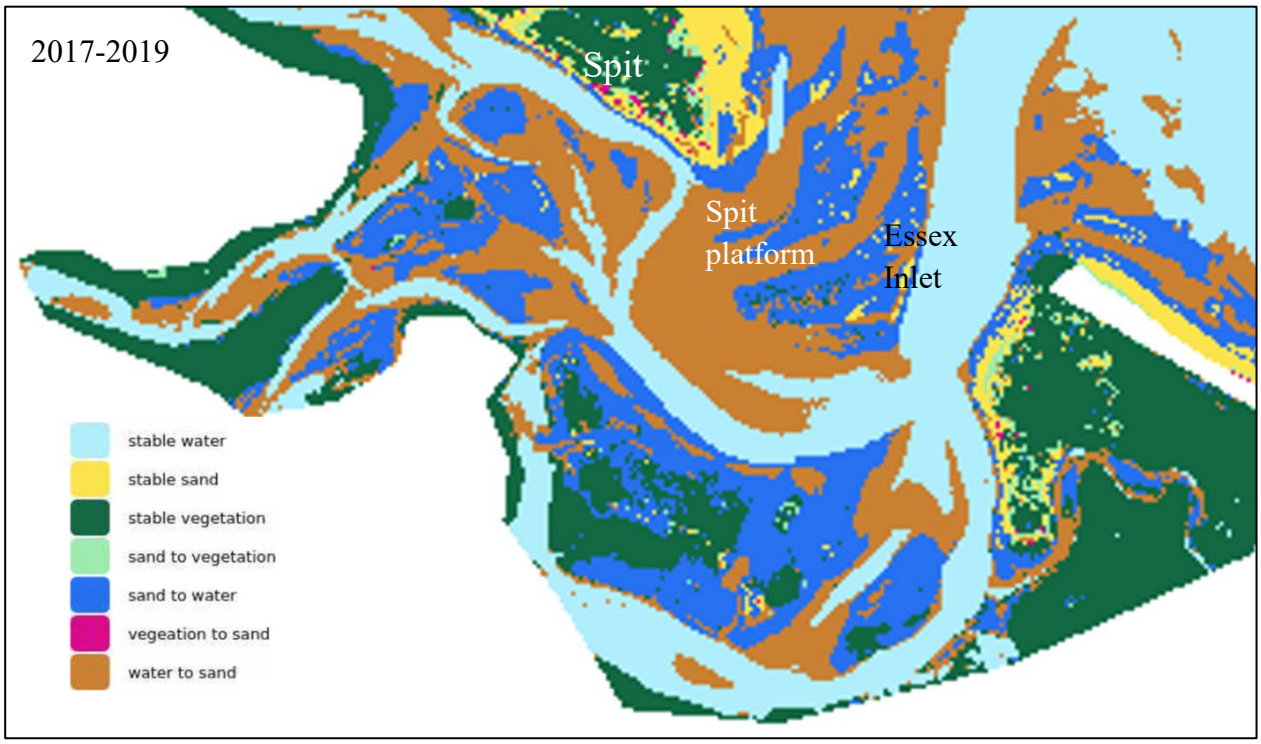


**Figure 61.** Map showing geomorphic changes of Essex Inlet and Bay system between 2017 to 2019. Note the water to sand province (brown pattern) on the spit platform and on the western flood-tidal delta.

**Table 7.** Area and Volumes of Spit 2011-2016

| ***Date*** | ***Spit Area*** **($m^2$)** | ***Spit Volume*** **($m^3$ above msl)** |
|---|---|---|
| 2011 | 306,000 | 394,000 |
| 2014 | 212,000 | 296,000 |
| 2016 | 211,284 | 216,148 |

Loss of sand from 2011 to 2016 ~**178,000 $m^3$**
Note 1. Sand loss is **237,000 $m^3$** when extrapolated back to 1995.


**Figure 62**. Backbarrier channel in 2008 (red outline) compared to sand channel footprint in 2018. Note slight migration of channel against spit and overall filling of channel during the 10-year period. This filling accounts for some of sand washed into the backbarrier.

## D. Inner Essex Bay Flood-tidal Delta

Outer and Inner Essex Bay/Estuary are separated by a narrow bedrock channel between Cross Island and Conomo Point, that reaches almost 12 m in depth. This constriction produces tidal currents in excess of 2 m/s during spring tides and any sand deposited in the channel during lower flow conditions is swept into the inner bay during by flood tidal currents. The flow expands immediately landward of Cross island and sand moving through the channel is deposited in a large flood-tidal delta (Figure 5b). During the period of spit retreat, when sand washed into Essex Bay, some of this sediment was transported into the inner bay enlarging the flood-tidal delta (Table 8; Figure 62). Image analysis was used to compute areas and volumes of the flood delta, indicating that the delta gained approximately 185,000 $m^3$ between 2010 and 2016 (Table 8). A comparison of the two images shows that between 2007 and 2016 the flood delta expanded its size by building northward and westward, and creating more intertidal area (Figure 62). The fact the flood delta enlarged during the same period that the spit retreated and sand washed into Essex Bay, is likely not coincidental. This sedimentation process suggests that the surfice sand is highly mobile in Essex Bay and can be transported far inland from its original source.

**Table 8.** Inner Flood-Tidal Delta Geometry

| **Year** | **Intertidal Area** ($m^2$) | **Volume** ($m^3$) |
|---|---|---|
| 2016 | 294,000, | 838,000 |
| 2014 (post-Sandy) | 260,000 | 765,000 |
| 2010 | 226,000 | 663,000[1], 644,000 |

Total sand volume gain between 2010[2] and 2016: **185,000 $m^3$**

Note 1: values estimated using area-volume relationships
2: average of 2010 estimates used to compute volume


**Figure 63.** Comparisons of the inner flood-tidal delta from 2007 to 2016. Both images were taken at similar low-tide elevations.

# VIII. DISCUSSION

## A. Long-term Assessment of Castle Neck Footprint

The most reliable dataset for assessing the future of Castle Neck covers the period between 1938 and 2018 (Figure 63; Appendix 4). It is easily recognized that the backside of the island has changed little since 1938 and that most of the net shoreline advancement and retreat has occurred along the exposed seaward side of the barrier. Figure 63 and Table 9 demonstrate that the barrier footprint has diminished in size by more 438,778 $m^2$ from 1938 and 2018, and that most of this loss occurred along the southern half of the island. This area is equivalent to 82 football fields, and if these football fields were placed sideline to sideline, it would cover a distance extending approximately from the Steep Hill drumlin to almost the end of the Southern Spit. It is noteworthy that barrier accreted between 1972 and 1992, when it grew by 674,671 $m^2$. These gains were followed by period of net erosion and net accretion between 2003 and 2018. Likewise, the beach west of Steep Hill (Steep Hill Beach) has undergone considerable fluctuations in erosional and depositional trends (Figure 64). It is interesting that the 1844-1897 shoreline is not substantially different from the 2007-2009 shoreline. However, during the interim the beach has done a kind of seesaw movement whereby outbuilding along one half is coincident with retreat of the adjacent beach and vice versa.


**Figure 64**. High-tide shorelines for 1938 and 2018.During this period the footprint of barrier decreased by 438,788 $m^2$.

**Table 9.** Castle Neck Area Data

| Year | Area ($m^2$) | Difference with previous year ($m^2$) | Difference from 1938 ($m^2$) | Shoreline Trend |
|---|---|---|---|---|
| 1938 | 4,319,417 | 0 | 0 | Gain |
| 1960 | 4,412,721 | 93,304 | 93,304 | Loss |
| 1972 (May) | 4,008,429 | -404,291 | -310,987 | |
| 1972 (August) | 3,540,333 | -468,096 | -779,083 | |
| 1978 | 3,803,475 | 263,142 | -515,941 | |
| 1991 | 3,996,628 | 193,153 | -322,788 | |
| 1992 | 4,215,004 | 218,376 | -104,412 | |
| 1995 | 4,066,043 | -148,961 | -253,373 | |
| 2003 | 3,731,062 | -334,980 | -588,353 | |
| 2018 | 3,880,628 | 149,565 | -438,788 | |
| 2020 | 3,707,459 | -173,169 | -611,958 | |

**Figure 65.** Historical shoreline changes of Steep Hill Beachfrom CZM Shoreline Mapper.

The causes of the long-term areal loss and beach retreat of Castle Neck must be considered in terms of where most this loss occurred, which is in the southern half of the island involving specifically, the spit. It should also be noted that this shoreline retreat took place not only at the spit end but also along the seaward beach. If the areal size of the island is a qualitative proxy for barrier sand volume, then as Table 9 demonstrates Castle Neck goes through cycles of erosion and deposition having variable durations. The erosional period cannot be correlated with a major storm; the beach gained acreage after the 1938 Hurricane and Blizzard of 1978 and lost beach during a relatively quiescent period from 1960 to 1972. Sea level trends also do not seem to explain the barrier areal signal. As observed in Figure 65, the rate of sea level rise diminished between 1960's and mid 1990's. However, during the same time there was a 12-year period of erosion followed by a 20-year period of accretion. The waxing and waning nature of the barrier footprint, which takes place in a long-term trend of erosion, is likely a result of many interrelated factors working over different time scale. For example, storms not only erode beaches resulting in significant shoreline retreat, storms can also produce river flooding, depending on their duration, pathway, and rainfall, that results in increased delivery of sand to the coast (FitzGerald et al 2002). Another factor that often goes overlooked is how the delivery of sand to barrier can be cyclic in nature.

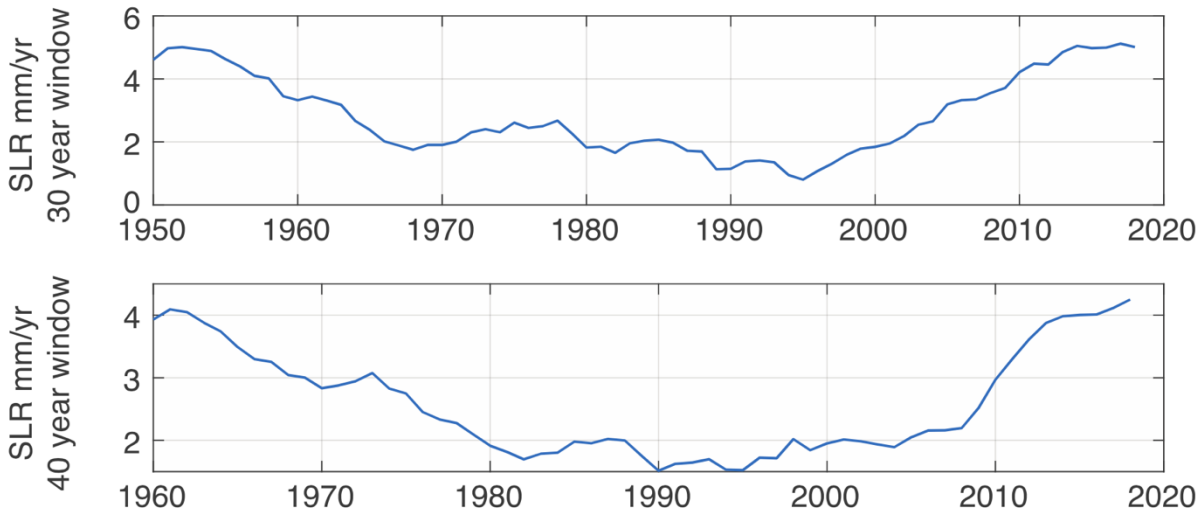


**Figure 66.** Running Boxcar averages of NOAA Boston Harbor tide gage. data (from FitzGerald et al 2021). Note the decrease in sea level rise rate between 1960 and 1995.

## B. Inlet Sediment Bypassing and Sand Delivery to Castle Neck

The initial source of sand for Castle Neck barrier formation was from sediment reworked onshore during the late Holocene transgression (FitzGerald et al 2002). A secondary source, later

becoming the primary source, was sand discharged from the Merrimack River and transported south along Plum Island by wave energy (FitzGerald et al 2002; Hein et al 2012). Climate Change is projected to produce greater precipitation in the Northeast that will translate to increased river discharge and sediment delivery to the mouth of the Merrimack River Inlet. At the same time, predicted increased storminess will result in greater longshore transport rates. A wave study by Woods Hole Group (2017) calculated a southerly transport rate for southern Plum Island of 55,000 $m^3$ per year. However, they also showed that a 50-year recurrence event transports 73,000 $m^3$ of sand during a single northeaster.

Sand moving alongshore in the Plum Island littoral transport system is ultimately delivered to Plum Island Sound Inlet via waves and flood-tidal currents. Some of this sand also accumulates at the end of Plum Island forming Sandy Point (Figure 66). This is a spit complex that undergoes cycles of growth and decay taking about 15 to 20 years (Figure 67). As the sequential images illustrate in Figure 67, the spit complex extended 350 m across the spit platform from 2001 to 2008 and then retreated over the same distance during the next nine years. The length of the cycle is likely controlled in part by the frequency and magnitude of storms. Like Sandy Point, the spit platform (Figure 66) expands and contracts over a similar time scale and is related to the migration of the main ebb channel. As the spit platform accretes southward, the main ebb channel is forced southward as well, and extends along the barrier. Eventually this long pathway slows the tidal exchange, which leads to a new straighter course being cut through the ebb-tidal delta that is hydraulically more efficient. Once the new more northern channel is established, the former southern channel is abandoned and the sand shoal that was once updrift is now downdrift

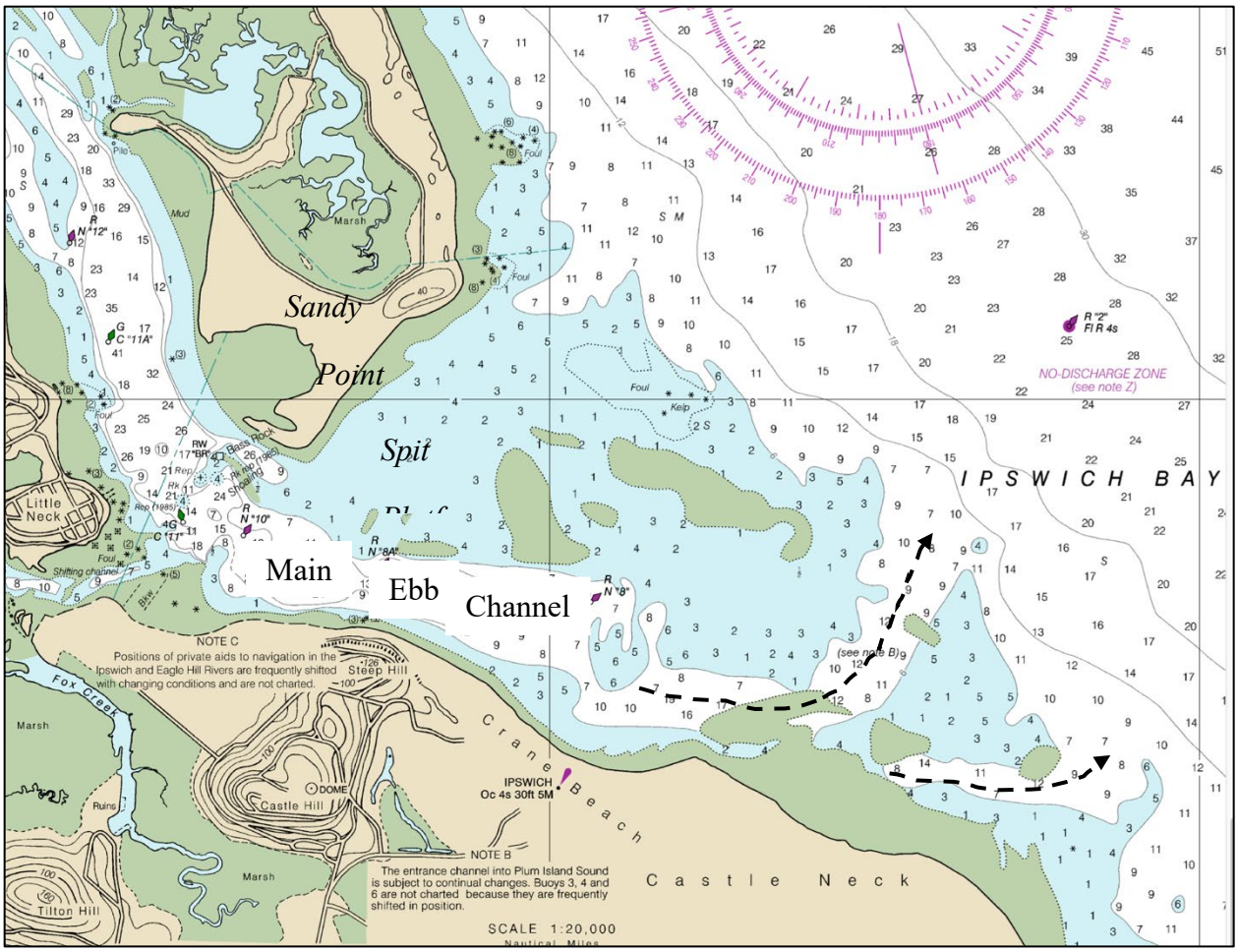


**Figure 67**. NOAA survey chart for Plum Island Sound Inlet. The arrows indicate positions of existing and former main ebb channels.

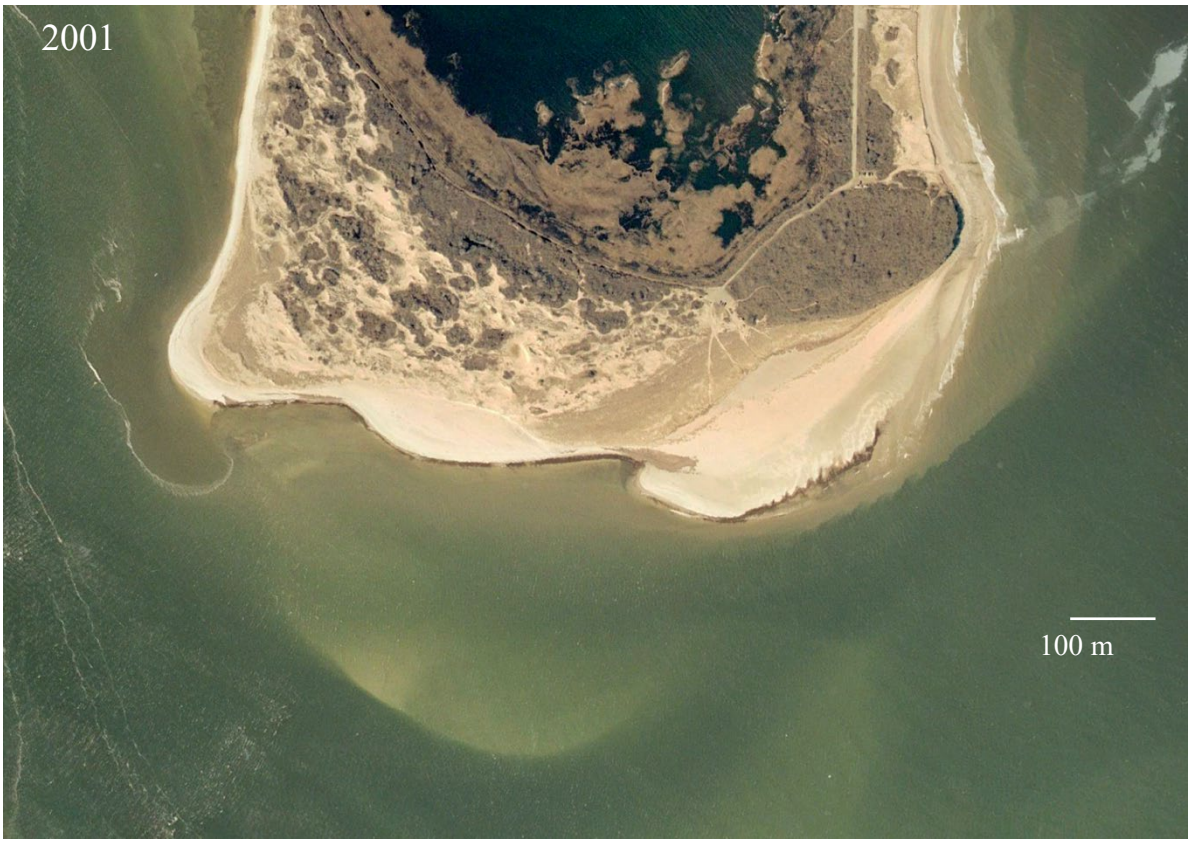
2001
100 m


2008
100 m


**Figure 68.** Sequential images depicting the growth and decay of Sandy Point spit complex. The growth represents a temporary sequestration of sand that is released to the inlet when the spit erodes and the shoreline retreats.

of the old channel. Because this sand shoal is no longer being pushed offshore by ebb-tidal currents, a combination of wave-generated and flood-tidal currents transport the shoal onshore where attaches to the beach. This is the process responsible for the construction of the beach protuberance and the overall morphology of Castle Neck.

Formation and evolution of the beach protuberance is illustrated in sequential images in Appendix 3. As shown in Figure 69, the sand bypassing Plum Island Sound Inlet not only builds the beach protuberance, landward-shoal migration extends for more than a kilometer to the south. The location where sand shoals weld to the beach is controlled by the alignment and position of the main ebb-channel. When the spit platform enlarges and progrades southward into the inlet, the main-ebb channel migrates downdrift and extends southeastward along the barrier. In this alignment, bar migrations occur far down the barrier. In contrast, when the spit platform is diminutive in size, the main ebb channel has a straighter more direct pathway through the ebb delta. In this configuration sediment bypassing occurs further northwest along the barrier. It should also be mentioned that the stage of onshore bar migration controls the supply of sand to the Southern Spit system. During the initial stages of


**Figure 69.** The red lines define the seaward extent of the main ebb channel. Note that the main ebb channels migrated to the southeast between 2006 and 2020. The double channels in 2020 defined a stage when a new northern channel is forming that will capture most of the ebb tidal prism.


**Figure 70**. 2014 image that shows landward bar migrations extending far southeastward from the beach protuberance.

Inlet sediment bypassing when the sand bars are some distance offshore, wave refraction around these bars causes a longshore transport reversal whereby sand is transported northward. This condition results in little sand moving south to the spit-end and thus, it becomes sediment-starved. Sand begins to be released from the northern beach protuberance sequestration site, after the bars have fully moved onshore and wave refraction is reduced. Thus, there is a close relationship between sand being trapped in the mid-barrier region and erosion and shoreline retreat of the Southern Spit.

## C. Sand Dynamics in Essex Bay and Estuarine System

As shown in Figures 58 and 59 and Table 7, approximately 178,000 $m^3$ of sand was lost from the Southern Spit and transported into Essex Inlet. Based on tidal current measurements, grain size trends, and bedform orientations, this sand was washed into Essex Bay and recirculated among the inlet channel, spit platform, and ebb-tidal delta (Figure 70). The fact that the ebb-tidal delta has not changed substantively in morphology or size argues that it has reached a dynamic equilibrium with its tidal prism (Smith and FitzGerald 1994). Thus, it is reasoned that

most of this sand ultimately is moved into Essex Bay and filling channels (i.e., Castle Neck River; Figure 61) and enlarging shoals (i.e., the west flood-tidal delta, Figure 70). It is also noteworthy that the inner bay flood-tidal delta also grew in size and volume during retreat of the Southern Spit (Figure 62). This deposition of sand landward of Conomo Point demonstrates the mobility of sand entering Essex Bay and that sand can be transferred several kilometers up the Essex Estuary. The landward movement of sediment is an important process for maintaining shellfish and eelgrass beds in a regime of accelerating SLR, and also providing platforms upon which marshes can form or enlarge. This is also an important in light of the fact that mineral sediment within the marsh peat consists of primarily of silt and fine sand (FitzGerald et al 2020).


**Figure 71.** Sand is recirculated among the different sand reservoirs, however there has been a net loss of sand from the Southern Spit system and most of this sediment now resides within Essex Bay and Estuarine system.

**D.** Wave energy distribution inside bay-

**E.** Flooding within the Town-

**F.** Sediment transport determined from modeling

## IX. CONCLUSIONS

### A. Observations

1. The Castle Neck barrier and Essex Tidal Inlet and Bay complex are part of a highly dynamic and interconnected sand transport regime that is dominated by a southerly longshore littoral transport system driven by northeast storms. Sand moving southward along Plum Island enters the Plum Island Sound where some of the sand builds the Sandy Point spit system and some is transported to the spit platform. These two sand reservoirs expand and contract controlling the deflection and southerly migration of the main ebb channel. In turn, the alignment of the main ebb channel dictates where the sand bars migrate onshore and weld to the beach as the end-product of the inlet sediment bypassing process.

2. Sand is sequestered for periods of 15 to 20 years at the mid-island region covering the beach protuberance and a kilometer length of shoreline to the southeast. Waves refracting around offshore bar complexes produce a transport reversal that traps sand until the bars attach to the beach. During the sand sequestration stage, the Southern Spit becomes sediment starved and between the 2011-2016 period it lost 178,000 $m^3$ of sand.

3. Sand eroded from the Southern Spit system moves in a net pathway into Essex Bay where it fills channels, such as Castle Neck River, and builds and enlarges sand shoals, including the inner flood-tidal delta west of Conomo Point. This movement of sand into Essex Bay helps to sustain shellfish grounds and eelgrass beds as sea level rises. The landward of sediment up the Essex Estuary also aids the delivery of silt and fine sand to the marsh platform improving their resiliency.

4. Castle Neck can be divided into four distinct regions based on sand transport trends, morphology, and patterns of shoreline change. Cedar Point and Steep Hill Beach are the westernmost beaches located west of the drumlin complex. This region is moderately stable but can experience periods of storm erosion followed by beach reconstruction amounting 30 to 40 of shoreline change. North Crane Beach sector is a region that has undergone dramatic changes related to shifts in the position of the main inlet channel. This can involve 50 to 400 m of shoreline advancement and recession. Presently, this section of shoreline is stable. The Beach Protuberance is an area that progrades and recedes depending on cycles of inlet sediment bypassing. The Southern Spit has been in a stage of erosion since 1995.

5. From 1938 to 2018 the Castle Neck barrier decreased in area by 438,788 $m^2$ (Table 9, Figure 63) and by 2020 the loss in area increased to 611,958 $m^2$ (Figure 71). This loss of sand was likely multicausal and related to sea-level rise, decreased sand supply coming from Plum Island, and sand losses to the offshore and to the backbarrier. The reduced sand coming from Plum Island may be related to human activities, including jetty repair, dredging activity, and construction of revetments and seawalls along the northern portion of the island.


Figure 72. High tide shoreline for 1938 compared to 2020.. Most of the loss in area was along the southern portion of the barrier amounting to 611,958 $m^2$.

## B. Management and outreach

The deliverables of this project include regularly meetings with local and town representations. Meetings have occurred between BU scientists and the Essex Select Board and members of other Neighboring Towns on a regular basis. In addition on October 27th 2019 an initial outreach event was held in Essex in conjunction with Essex Cruises to discuss the project with local people and stakeholder. We have also contructed a website with a project synopsis, description of the general findings and (after finalization of all results) maps of change and risk. Presently this can be found at https://zoeh63.wixsite.com/website/essex-mvp but will soon be moved to a permanent site on https://sites.bu.edu/coastallab/essex_mvp.

## X. ACKNOWLEDGEMENTS

We gratefully acknowledge the contributions of Peter Phippen of Mass Bays and Alyssa Novak of BU. In-kind match was provided by the Trustees and we are extremely grateful for all their field assistance and cooperation. We also thank all the BU interns and undergraduate students who assisted with field, lab, and modeling efforts.

## XI. REFERENCES

Booij N., Ris, R.R.C., Holthuijsen, L.H.L., 1999. A third-generation wave model for coastal regions 1. Model description and validation. Journal of Geophysical Research 104, 7649–7666.

Caldwell, R. L., and D. A. Edmonds (2014) The effects of sediment properties on deltaic processes and morphologies: A numerical modeling study, J. Geophys. Res. Earth Surf., v. 119, p. 961-982.

Dougherty, A.J., FitzGerald, D.M., and *Buynevich, I.V., 2004, Evidence for storm-dominated early progradation of Castle Neck barrier, Massachusetts, USA. *in*: Stone, G. and Orford, J. (eds.) Storms and their Significance in Coastal Morpho-Sedimentary Dynamics, Special Issue, *Marine Geology*, v. 210, p. 123-134.

Egbert, Gary D., and Svetlana Y. Erofeeva. "Efficient inverse modeling of barotropic ocean tides." Journal of Atmospheric and Oceanic Technology 19.2 (2002): 183-204.

FitzGerald, D.M., Hein, C.J., Connell, J.E., Hughes, Z.J., Georgiou, I.Y 2021, Largest marsh in New England near a precipice. *Geomorphology* v. 379, 1-17.

FitzGerald, D.M., *Buynevich, I.V., Davis, R.A., Jr. and *Fenster, M.S., 2002, New England Tidal Inlets with Special Reference to Riverine Associated Inlet Systems. *Geomorphology*, v. 48 p. 179-208.

Hanegan K., and Georgiou, I.Y., 2015, Tidal modulated flow and sediment flux through wax lake delta distributary channels: Implications for delta development. Proceedings of the International Association of Hydrological Sciences.

Jensen, J. R. (1986). Normalized difference vegetation index. *Introductory Digital Image Processing, Prentice-Hall*, 17(7):379.

Kopp, R.E., DeConto, R.M., Bader, D.A., Hay, C.C., Horton, R.M., Kulp, S., Oppenheimer, M., Pollard, D., and Strauss, B.H., 2017: Evolving understanding of Antarctic ice-sheet physics and ambiguity in probabilistic sea-level projections. Earth's Future, v 5, p. 1217-1233, doi:10.1002/2017EF000663.

Legates, D.R. and McCabe Jr, G.J., 1999. Evaluating the use of "goodness-of-fit" measures in hydrologic and hydroclimatic model validation. *Water resources research*, *35*(1), pp.233-241.

Lesser, G., Roelvink, J., van Kester, J., and Stelling, G., 2004. Development and validation of a threedimensional morphological model. Coastal Engineering, v. 51, p. 883 - 915.

Liu K, Chen Q, Hu K, Xu K, Twilley RR (2018) Modeling hurricane-induced wetland-bay and bay-shelf sediment fluxes. Coastal Engineering, v. 135, p. 77-90.

McFeeters, S. K. (1996). The use of the normalized difference water index (ndwi) in the delineation of open water features. *International journal of remote sensing*, 17(7):1425–1432.

Meselhe, E. A., Rodrigue, M. D. (2013). "Models Performance Assessment Metrics and Uncertainty Analysis." Louisiana Coastal Area Program Mississippi River Hydrodynamics and Delta Management Study.

Olofsson, Pontus, H. C. B. E. (2009). Beeoda protocol for accuracy assessment. *Boston Educatio in Earth Observation Data analysis*.

Olofsson, P., Foody, G. M., Stehman, S. V., and Woodcock, C. E. (2013). Making better use of accuracy data in land change studies: Estimating accuracy and area and quantifying uncertainty using stratified estimation. *Remote Sensing of Environment*, 129:122–131.

Sakib, M., Nihal, F., Haque, A., Rahman, M., Akter, R., Maruf, M., Akter, M., Noor, S. and Rimi, R.A., 2016. Afforestation as a buffer against storm surge flooding along the Bangladesh coast. In *12th International Conference on Hydroscience Engineering Hydro-Science* (pp. 6-10).

Sakib, M., 2015. Sundarban as a buffer against storm surge flooding. *World Journal of Engineering and Technology*, *3*(03), p.59.

Smith, J.B., and FitzGerald, D.M., 1994, Sediment transport patterns at the Essex River Inlet ebb tidal delta, Massachusetts, U.S.A., *Journal of Coastal Research*, v. 10, p. 752-774.

Sullivan JC, Torres R, Garrett A, Blanton J, Alexander C, Robinson M, Moore T, Amft J, Hayes D (2015) Complexity in salt marsh circulation for a semienclosed basin. Journal of Geophysical Research-Earth Surfaces v. 120, p. 1973–1989.

Woods Hole Group, 2017. *Great marsh Resiliency Project Wave Analysis and Numerical Modeling*. Falmouth: Woods Hole Group. 78 p.

## APPENDIX 1. BEACH PROFILE RESULTS

**Beach profile changes as an indication of seasonal and storm impacts:**

Three RTK beach profile surveys were conducted for the purpose of documenting morphological changes to the beach, as they relate to seasonal changes in wave energy and storm events. The first survey was recorded after a period of fair weather (June 2020), the second after a summer storm (September 2020)m and the final survey recorded he effects of Hurricane Teddy. Y axis is elevation and X axis is distance from the reference point (here set as the back stake situated on the dune crests).

**Description of the six transects:**

***Transect 0:***

The major change occurred after Hurricane Teddy. The summer berm was removed, and a new berm formed from the large volume of sand moving onshore. The general steepness of the beach increased between summer and fall months.

***Transect 1:***

Major changes occurred from June survey to the survey after Hurricane Teddy. The accretionary berm was mostly removed by the summer storm, leaving a steep and uniform slope between the dune and the low-tide terrace. The elevation of the beach at this transect has generally increased. The September transect is shorter than the other surveys, because of a higher tidal elevation at the time of survey.

***Transect 2:***

This section of beach has been the most constant as recorded by the three surveys amongst the six profiles. Some beach elevation was lost from June to September along the beach face area. Nonetheless, the beach experienced elevation gained along the entire transect after Hurricane Teddy.

***Transect 3:***

Major changes took place from June profile to after hurricane Teddy. The summer berm was completely removed, and a new berm formed following Hurricane Teddy.

***Transect 4:***

The September profile is relatively shorter compared to the others. Some elevation loss (~30 cm) occurred from the dune-dune scarp-upper berm area. After Hurricane Teddy, the summer berm was completely removed, developing a more uniform, steep profile.

***Transect 5:***

The morphology of the beach here did not change significantly. Approximately, 0.5 m elevation of beach was lost between June and September in the upper berm-berm area. After Hurricane Teddy, a consistent volume of sand was reworked, the eroded area accreted (elevation here on 11$^{th}$ October is similar to 6$^{th}$ June). Still, the summer berm was removed, and a new one formed after Hurricane Teddy.

# APPENDIX 2. KURTOSIS AND SKEWNESS TRENDS

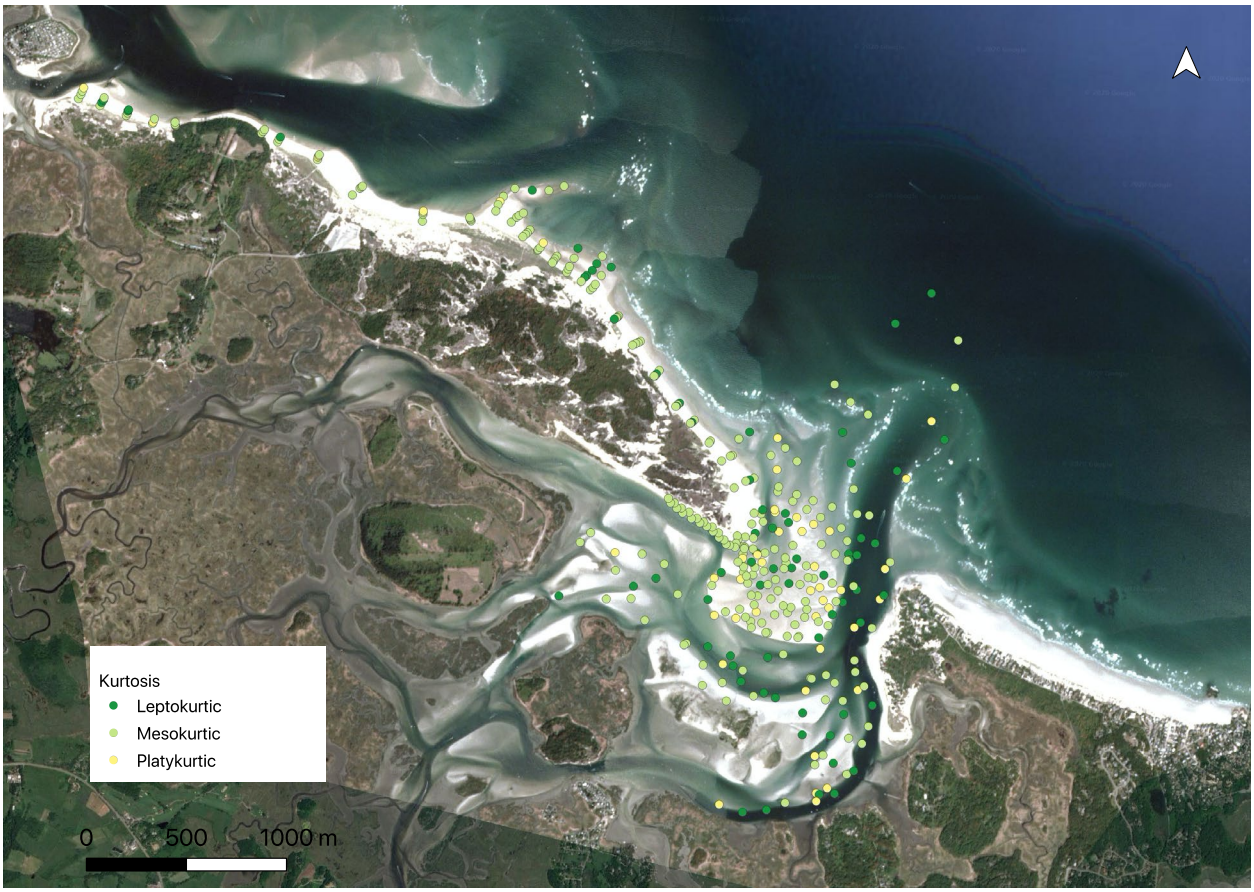


Skewness
coarse skewed
fine skewed
symmetrical
0
500
1000 m

**APPENDIX 3. SEQUENTIAL DEVELOPMENT OF THE BEACH PROTUBERANCE**

**(July 2006 – Oct 2020)**

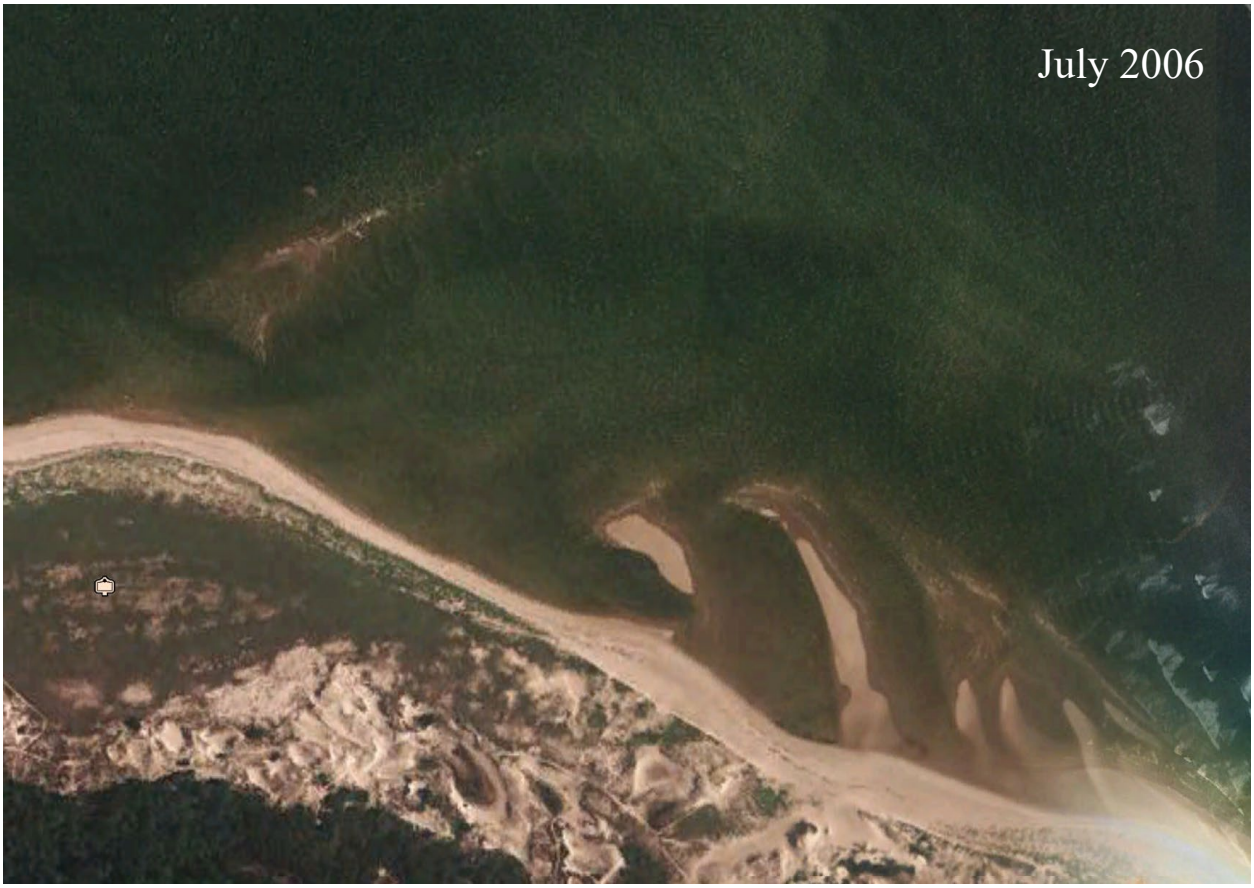


July 2007


April 2008


July 2008


June 2010


Dec 2010


August 2013


Sept 2014


June 2015


May 2016


April 2017

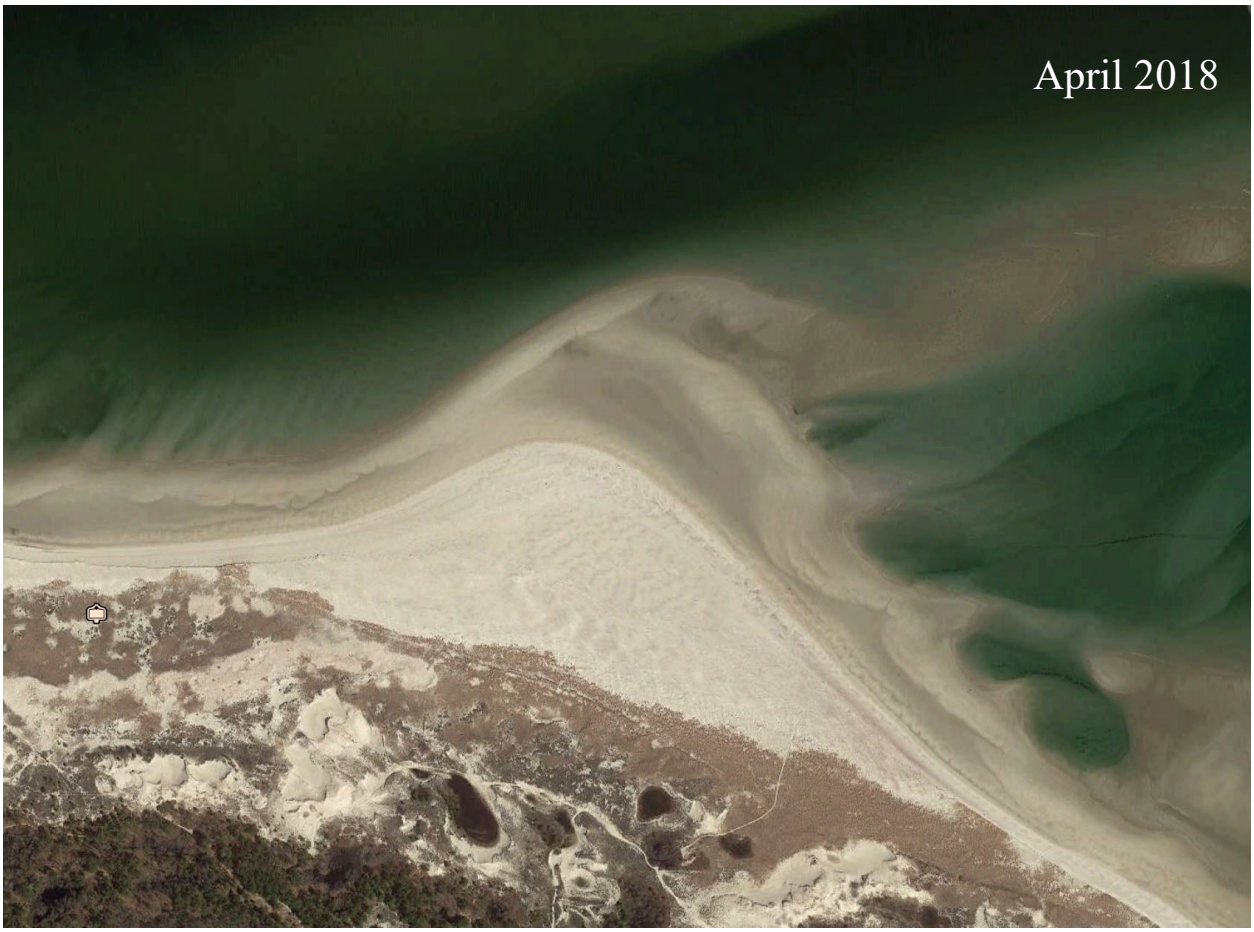
April 2018


June 2019


Oct 2020
Green Trail
Orange Trail
Red Trail

## APPENDIX 4. HISTORICAL SHORELINE CHANGES

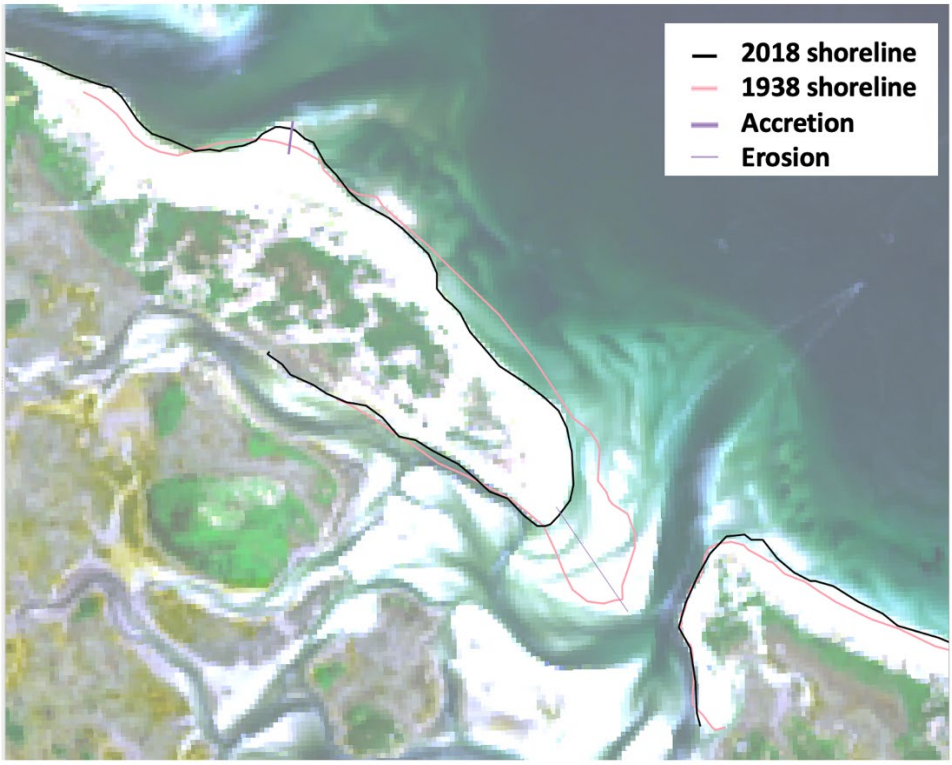


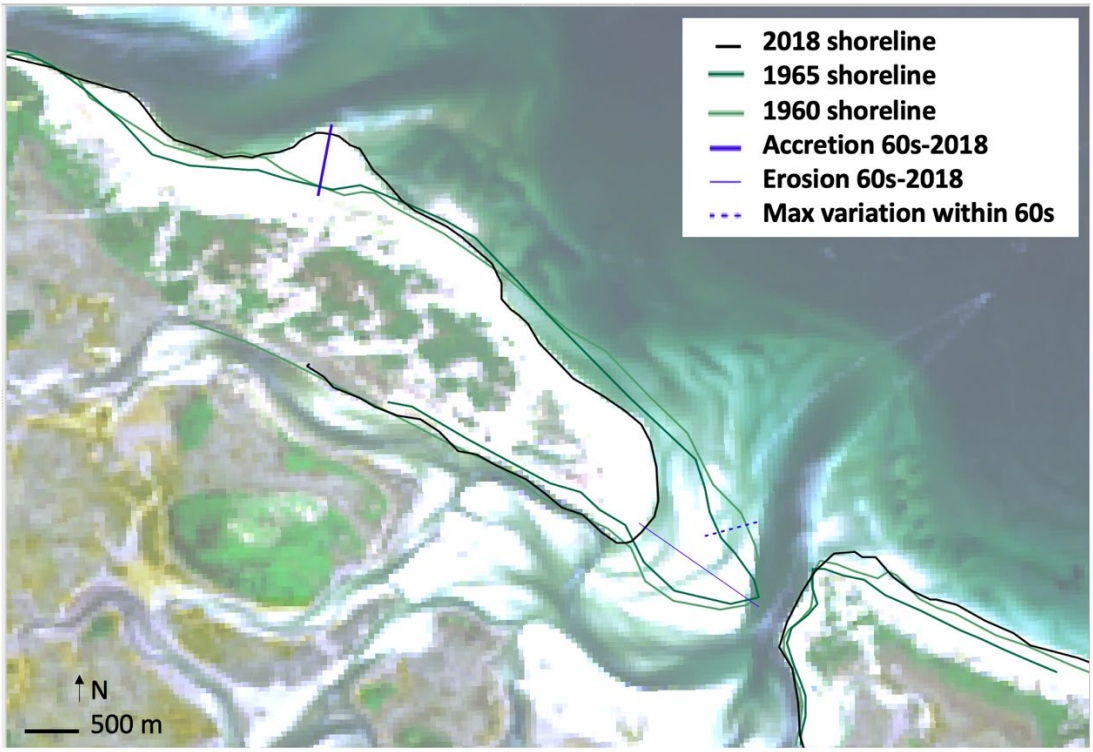

# APPENDIX 5: STORM ANALYSES

TS = Tropical Storm

XT = Extra Tropical Storm

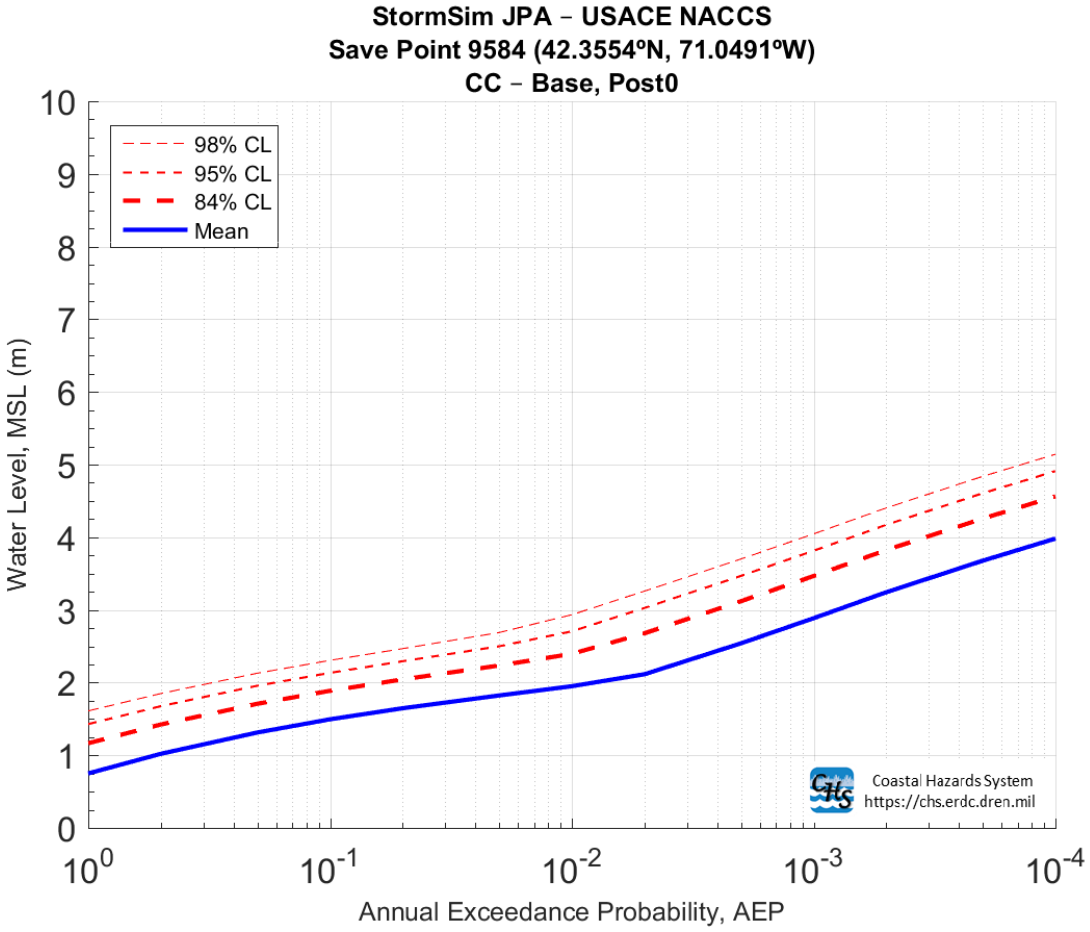

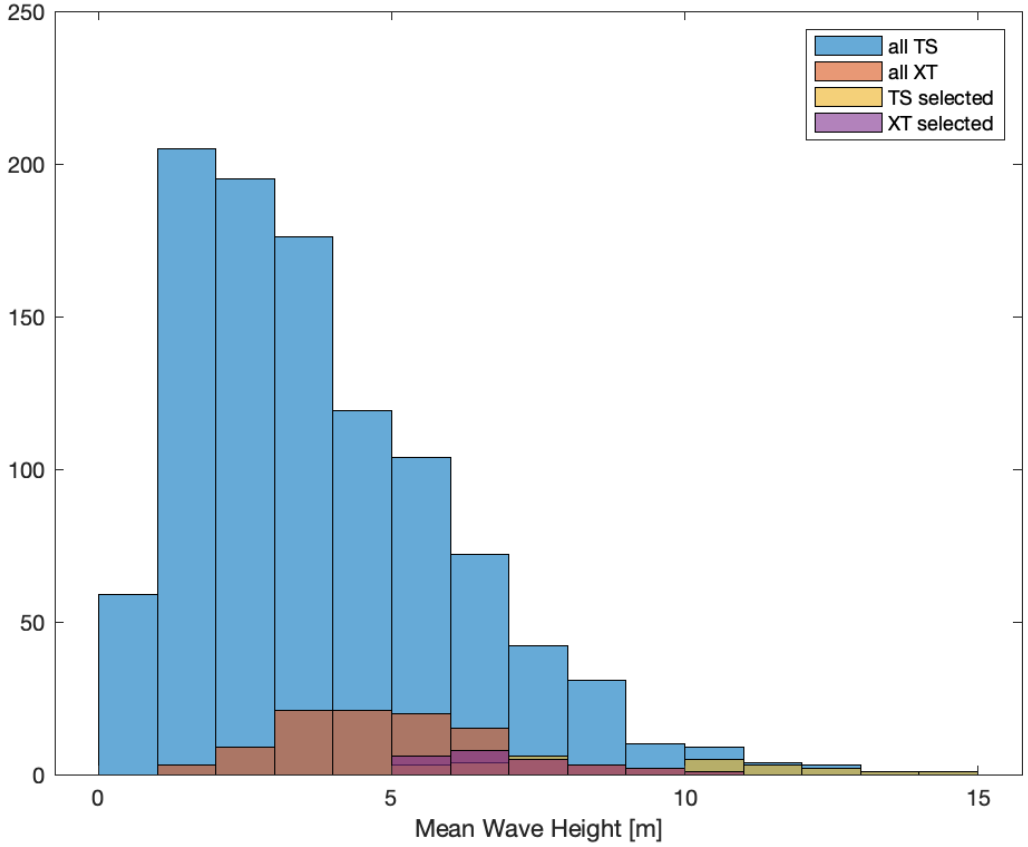
250
200
150
100
50
0
0
5
10
15
Mean Wave Height [m]
all TS
all XT
TS selected
XT selected

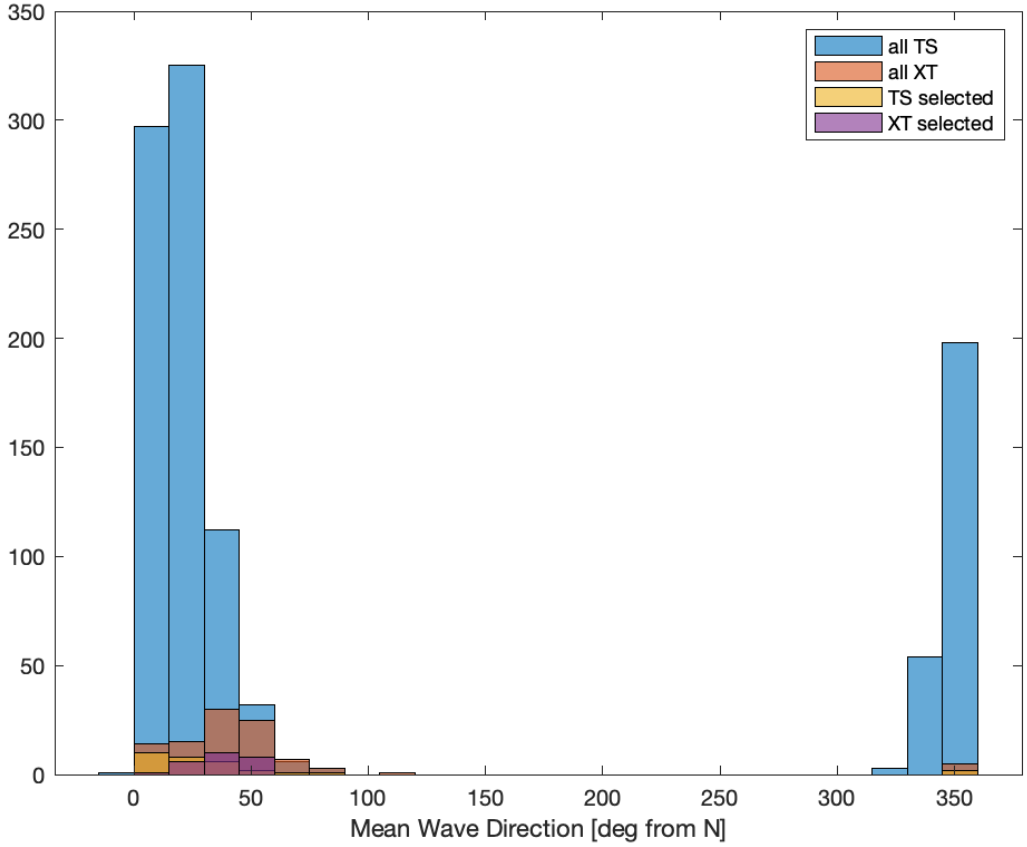
all TS
all XT
TS selected
XT selected
350
300
250
200
150
100
50
0
0
50
100
150
200
250
300
350
Mean Wave Direction [deg from N]

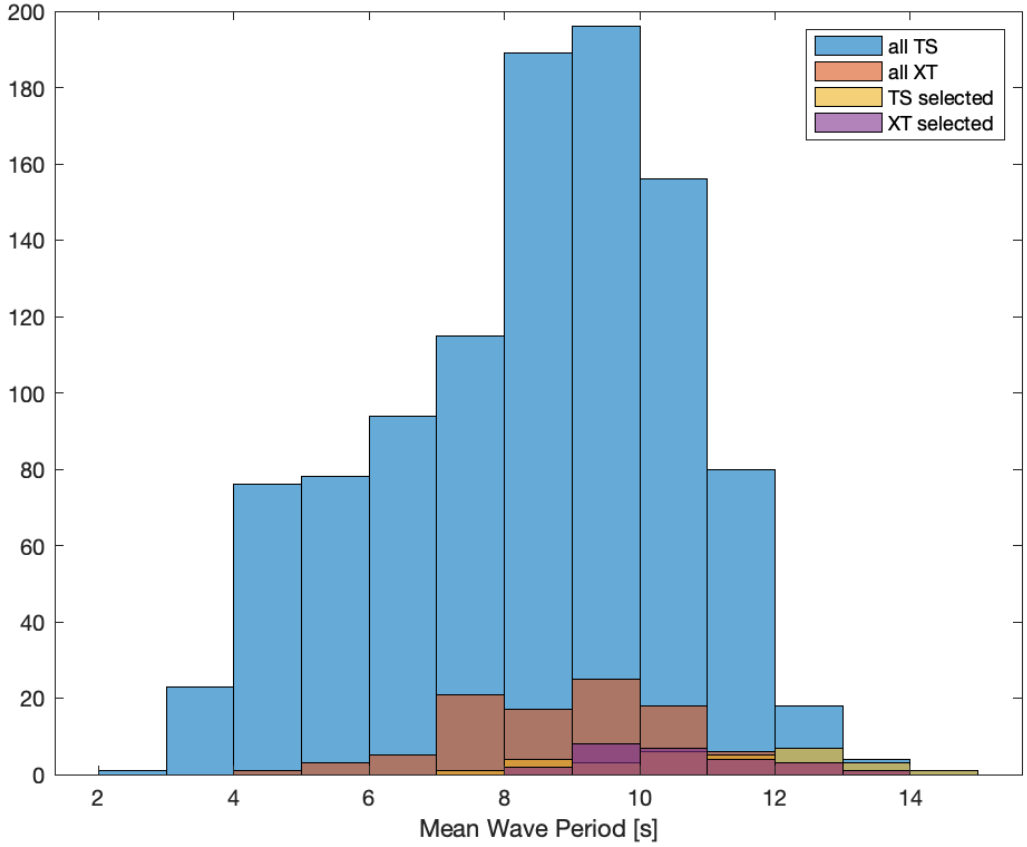
all TS
all XT
TS selected
XT selected
200
180
160
140
120
100
80
60
40
20
0
2
4
6
8
10
12
14
Mean Wave Period [s]

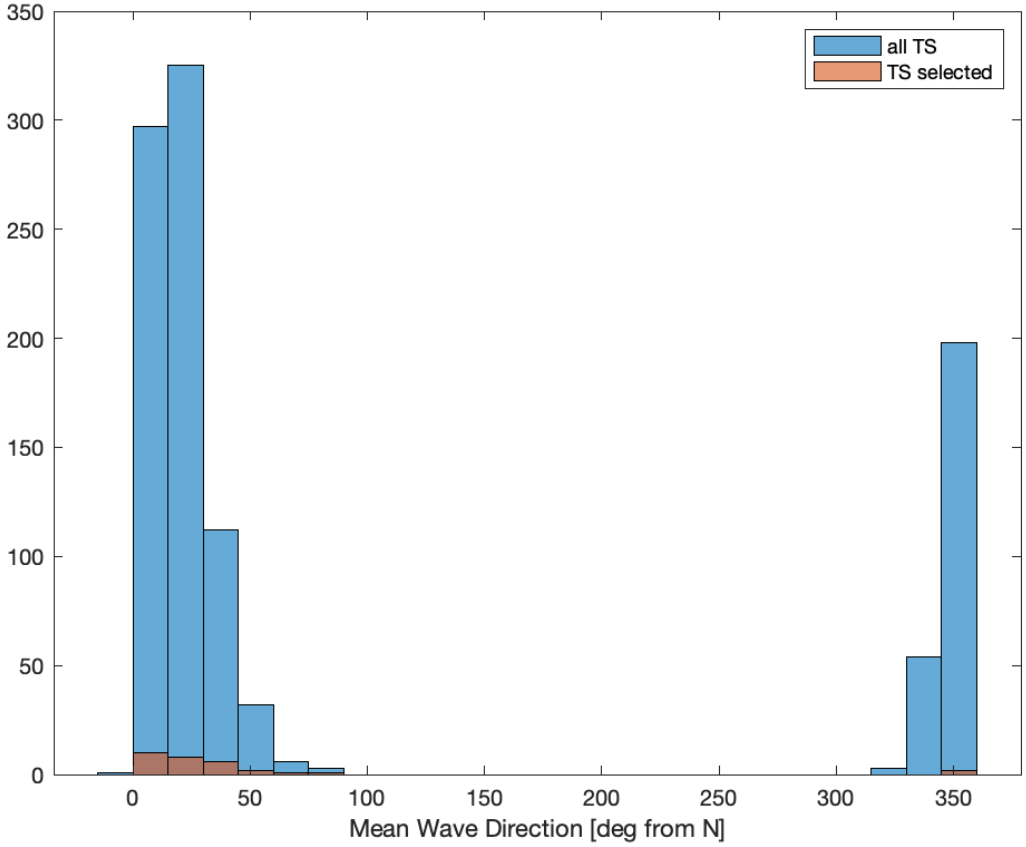
all TS
TS selected
350
300
250
200
150
100
50
0
0
50
100
150
200
250
300
350
Mean Wave Direction [deg from N]

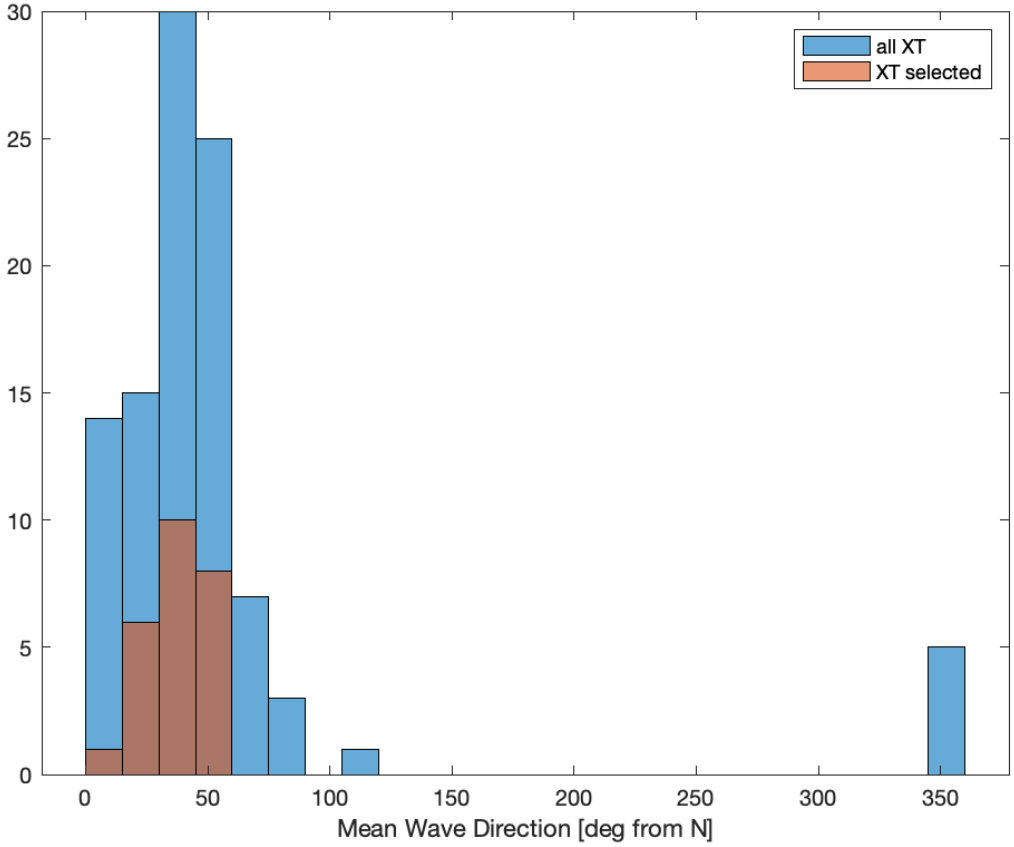
all XT
XT selected
30
25
20
15
10
5
0
0
50
100
150
200
250
300
350
Mean Wave Direction [deg from N]

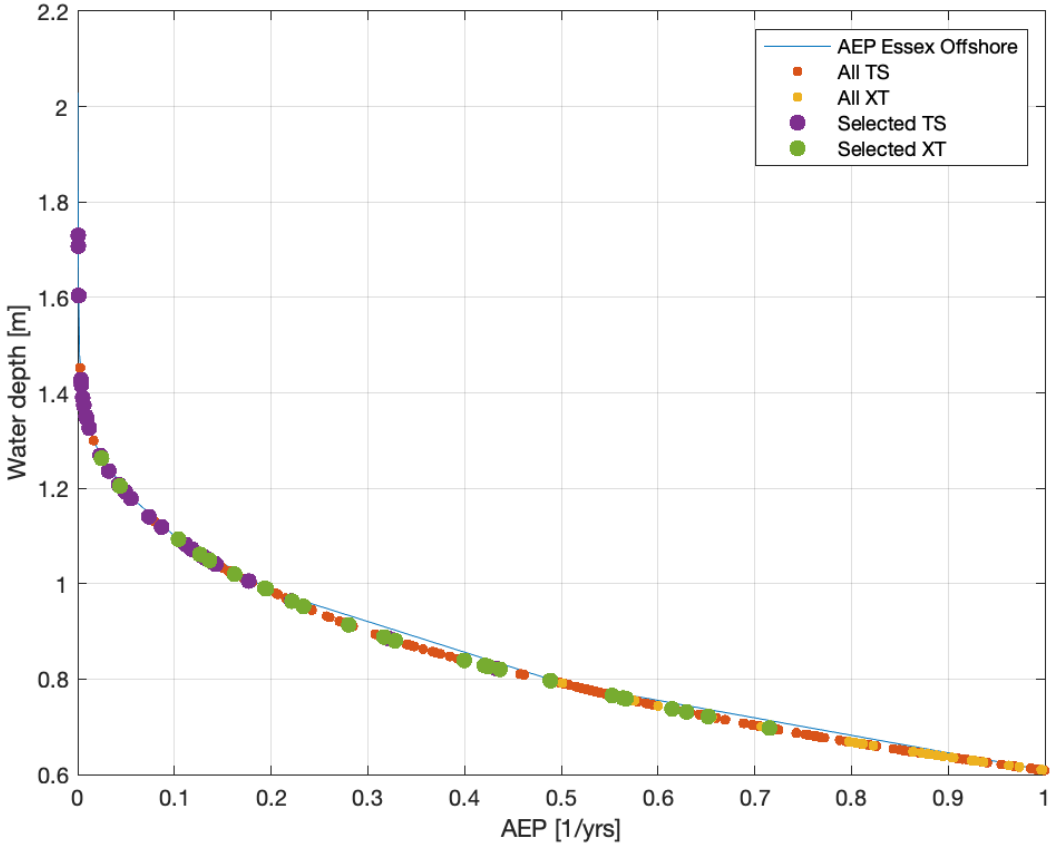
AEP Essex Offshore
All TS
All XT
Selected TS
Selected XT
Water depth [m]
AEP [1/yrs]
2.2
2
1.8
1.6
1.4
1.2
1
0.8
0.6
0
0.1
0.2
0.3
0.4
0.5
0.6
0.7
0.8
0.9
1

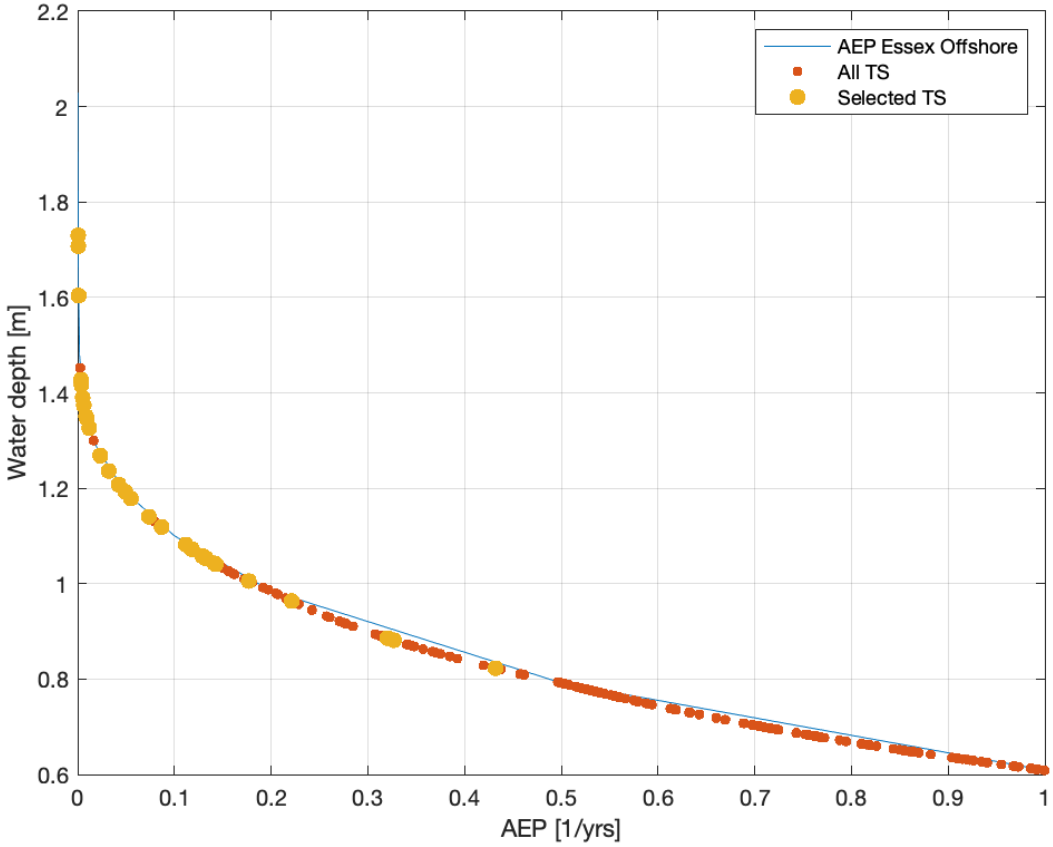
AEP Essex Offshore
All TS
Selected TS
Water depth [m]
AEP [1/yrs]
2.2
2
1.8
1.6
1.4
1.2
1
0.8
0.6
0
0.1
0.2
0.3
0.4
0.5
0.6
0.7
0.8
0.9
1

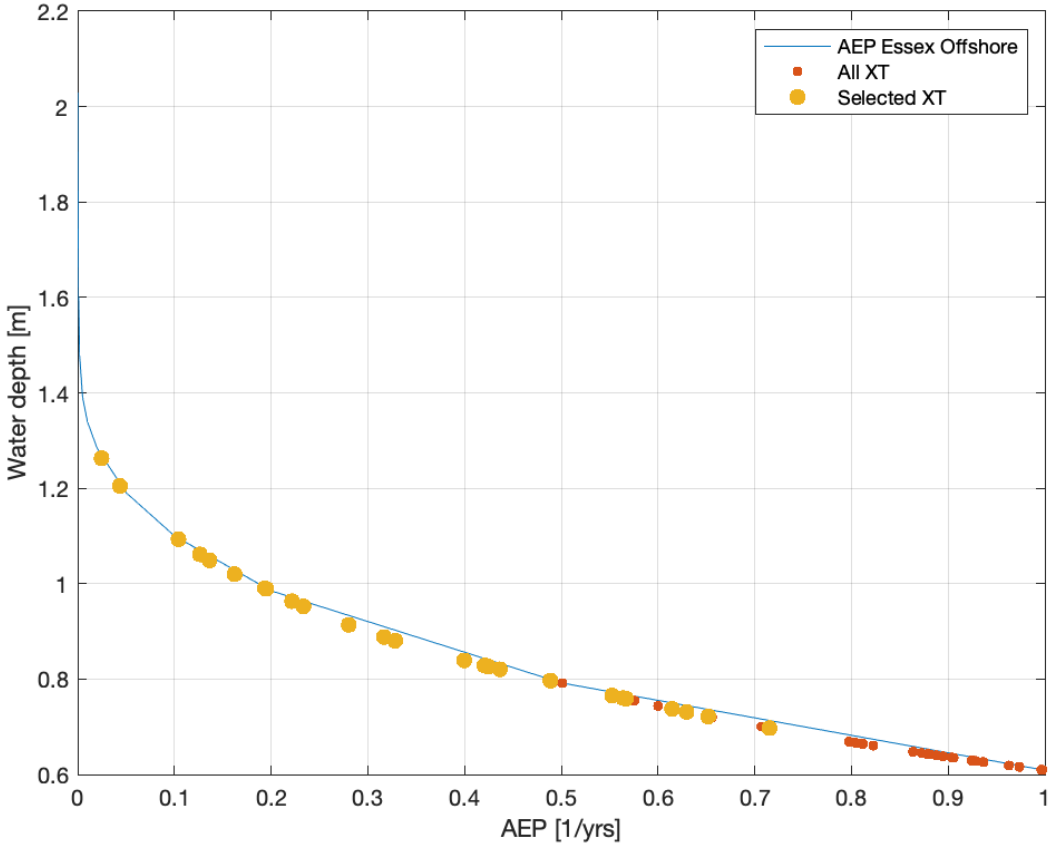
AEP Essex Offshore
All XT
Selected XT
Water depth [m]
AEP [1/yrs]
2.2
2
1.8
1.6
1.4
1.2
1
0.8
0.6
0
0.1
0.2
0.3
0.4
0.5
0.6
0.7
0.8
0.9
1

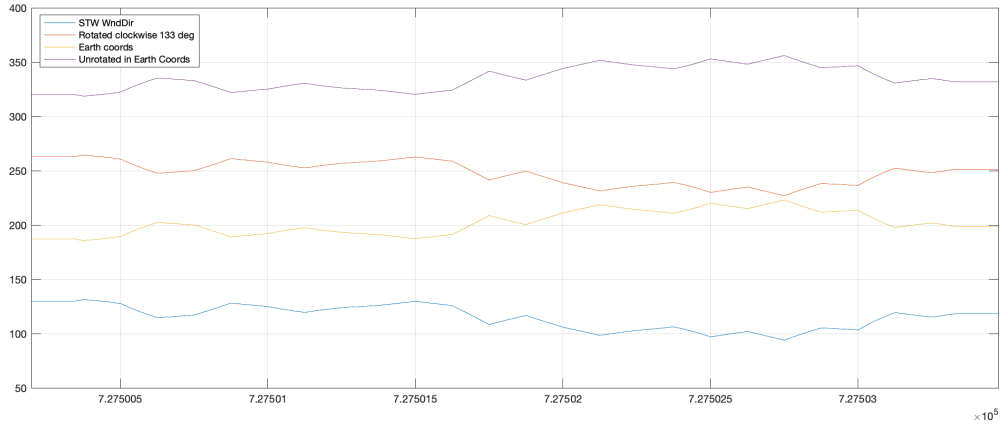
STW WndDir
Rotated clockwise 133 deg
Earth coords
Unrotated in Earth Coords
400
350
300
250
200
150
100
50
7.275005
7.27501
7.275015
7.27502
7.275025
7.27503
×10^5

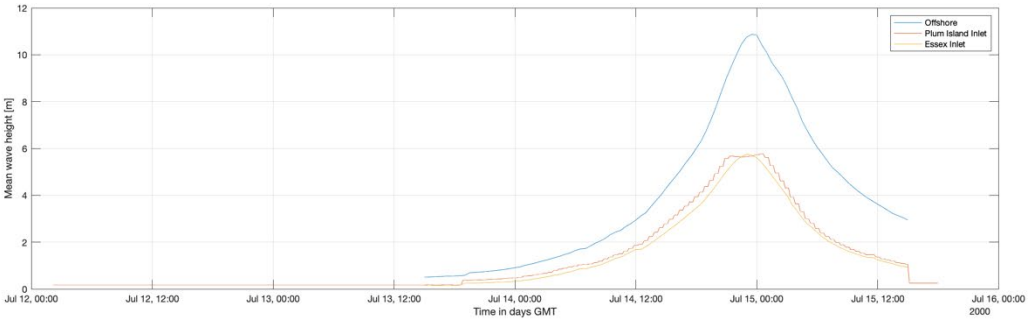
Offshore
Plum Island Inlet
Essex Inlet
Mean wave height [m]
12
10
8
6
4
2
0
Jul 12, 00:00
Jul 12, 12:00
Jul 13, 00:00
Jul 13, 12:00
Jul 14, 00:00
Jul 14, 12:00
Jul 15, 00:00
Jul 15, 12:00
Jul 16, 00:00
2000
Time in days GMT